CORA Cork Open Research Archive
Cartlann Taighde Oscailte Chorcaí

Title	Electrochemical sensors for integration on silicon
Authors	Barry, Fiona
Publication date	2022-03-31
Original Citation	Barry, F. 2022. Electrochemical sensors for integration on silicon. PhD Thesis, University College Cork.
Type of publication	Doctoral thesis
Rights	© 2022, Fiona Barry. - https://creativecommons.org/licenses/by-nc-nd/4.0/
Download date	2026-11-15 10:24:38
Item downloaded from	https://hdl.handle.net/10468/14097



UCC
University College Cork, Ireland
Coláiste na hOllscoile Corcaigh

Ollscoil na hÉireann, Corcaigh
National University of Ireland, Cork



Electrochemical Sensors for Integration on Silicon

Thesis presented by

Fiona Barry

for the degree of

Doctor of Philosophy

University College Cork

Tyndall National Institute



Head of School/Department: Dr. Fatima Gunning

Supervisor(s): Dr. James Rohan and Dr. Lorraine Nagle

2022

Declaration

This is to certify that the work I am submitting is my own and has not been submitted for another degree, either at University College Cork or elsewhere. All external references and sources are clearly acknowledged and identified within the contents. I have read and understand the regulations of University College Cork concerning plagiarism and intellectual property.

_____

Fiona Barry

March 31st 2022

Foreword

The research disclosed in this thesis was undertaken as part of a funded project with Analog Devices and the SFI centre CONNECT. CONNECT is a research centre focusing on future networks and communications, my research on the development of electrochemical sensors relates to this through the need for sensors in the Internet of Things (IoT) networks. This work has been funded from research grants from (i) Science Foundation Ireland and the Department of Agriculture, Food and Marine (Grant 16/RC/3835 (VistaMilk) and (ii) Analog Devices and Science Foundation Ireland (Grant 13/RC/2077_P2 (CONNECT)).

Abstract

Water quality monitoring is crucial to ensure the safe consumption of drinking water by humans. It is of such importance that the UN has included a specific goal for the improvement of water and sanitation in their Sustainable Development Goals (SDG). According to the UN, a staggering 3 in 10 people are without access to safely managed drinking water. At present the standard method for water quality monitoring is by laboratory testing. These typically require transportation of the sample from source to the laboratory, additional reagents, and specialised personnel and equipment to carry out the analysis. In this thesis, electrochemical methods at micro-electrodes are explored and developed for reagent-free, point-of-care analysis that does not require the need for specialised training. The main goal of the thesis is to develop low-power micro-sensors for point-of-care analysis. To achieve this, interdigitated micro-electrodes were investigated wherein each comb of electrodes could be biased separately allowing for unique analysis opportunities.

Discussed herein simulations of electrode geometries are used to establish the optimum design for the interdigitated electrode arrays. The fabricated interdigitated arrays are subsequently modified with nanoporous gold resulting in an increase in current for the detection of lead by 1.5-fold. These modified interdigitated electrodes successfully detected lead in 0.1 M acetate buffer pH 4.6 with a limit of detection of 0.43 ppb. However, issues arise when applying these electrodes to reagent-free tap water, where there is no discernible peak for lead seen below 50 ppb. To overcome this obstacle the interdigitated arrangement of the electrodes can be used to electrochemically control the pH of tap water without the need for additional reagents. This leads to the successful detection of lead in tap water to as low as 10 ppb.

Scope of Thesis

The scope of this thesis is to explore the design, fabrication, and application of these NPG-modified gold IDE arrays will be discussed in the following chapters. The objective is to successfully apply these devices to reagent-free detection of lead in tap water.

In chapter 1, an overview of fundamental electrochemistry concepts is given. As simulations are an integral part to the design of the electrodes in this thesis, a brief background on the set-up and theory of the simulations is given. Chapter 1 closes with a review of literature focusing on the detection of lead highlighting the issues currently faced and how the research in this thesis will overcome these challenges.

In Chapter 2, the designs of the IDEs of gold electrodes on silicon chips were decided on based on simulations of various IDE geometries. The designs that showed the best simulated current outputs were subsequently fabricated in Tyndall National Institute. The fabricated chips were electrochemically characterised, which was compared to the simulated data. This chapter introduces the interesting concept of adding an insulating capping layer to the electrodes to further enhance the array performance.

In Chapter 3, explores modifying the IDE surface with NPG. These modified electrodes were subsequently applied to the detection of lead. Initial detection was carried out in 0.1 M acetate buffer pH before moving onto to detection in tap water.

Chapter 4 expands in the work carried out in Chapter 3 by utilising the other comb of electrodes in the IDE to electrochemically alter the pH of the water sample for improved detection of lead in tap water.

Finally, Chapter 5 summarises the key results achieved in this work and highlights potential future work which could be undertaken.

Acknowledgements

I would first like to thank my supervisors Dr. James Rohan and Dr. Lorraine Nagle for supporting me throughout the PhD. Thank you, James, for providing me with the opportunity to pursue this PhD and possibly more importantly, keeping me employed while I waited for the right project for me to come along. The knowledge and experience you have shared with me and the encouragement you have shown me have not just made me a better researcher but more confident in myself. Thank you, Lorraine, for your daily support in the lab. I have acquired a wealth of knowledge from working so closely with you but most importantly your support and our chats really helped me keep going at times where I felt like giving up. So, for this I will be forever grateful.

I would also like to thank all the other researchers and post-docs who have helped me throughout this journey. Dr. Amelie Wahl who supervised me during my first internship, your expertise and work ethic was inspiring and my time working with you really stood to me. I thoroughly enjoyed our time together, both in the lab and outside of it, usually in Cavanaghs. Thank you to Dr. Declan Casey for your supervision on my second internship and teaching me all about copper plating and nickel-iron plating. Also thank you for your support in the lab and promptly fixing anything that breaks. Thank you to Dr. Pierre Lovera for letting me use the NTG, my time in the NTG lab was so integral to me getting a lot of the results for this thesis so I am very grateful for that. And thank you for all your amazing facts about Carlow. Thank you to my lab-mates Ehren and Aaron who have always been so kind to help me and loan chips and holders whenever I needed them.

My thanks also go to member of the extended Tyndall team who have helped support this research. In particular Dan O'Connell and the team in the fab for making our devices, Richard Murray for designing the masks, Donal O'Sullivan for fabricating the chip holders, Don Lynch, and Brian Walsh for the IT support, and to Feargal Nolan and Alan

Lester for sourcing our tap water samples from the 4th floor. Particularly Alan who was subjected to weekly requests for more water, thank you so much for being so nice about it.

A massive thank you to my amazing friends in and outside of Tyndall, none of whom I will refer to as doctors to keep the doctors humble. Thanks to Ian for putting up with me for all these years and I guess as an extension I should thank Sinéad for introducing us, which is a bit mad. It's been a pleasure being your friend throughout our college experience and seeing what a stylish gentleman you have become. Thank you for always being so willing to share your knowledge and support with me. It will be weird not studying or working in the same place as you anymore, so we need to get cracking up setting up our businesses. Thanks to Julia for always being a ray sunshine, I always feel so much better after being around you. You have been the best gym and running buddy a girl could ask for and I can't imagine what the pandemic would have been like without you and our daily walks. Thank you to Louise for being my first desk buddy in Tyndall and showing me the ropes, I was so sad when they moved me. Thanks to Caoimhe for all her amazing organising and always having tv and movie recommendations. Niamh, thank you for introducing me to rugby and getting to go to Kinsale 7's and encouraging me to do the SPRINT programme. Thanks to Colm, who may not know it, but his words of wisdom on a random night in Impala gave me the inspiration I needed to get the results I needed to finish this thesis. Another person to whom I will be forever grateful. Thanks to Benjy for putting up with all my Comsol questions. Thank you to Muireann who is an absolute breath of fresh air to be around and always up for the craic, and for not being annoyed at my long silences. And thanks to the many more for all the tea breaks, hiking trips and many an evening in Impala.

Thank you to the O'Mahony family for their support throughout my PhD, to Seamus and Carmel for being so understanding when I disappeared for a few months to write up, to Áine for supplying lots of delicious baked goods and to Eoin and Ruth for the goody bag you brought me when I had Covid. Thank you all for your support, it means the world to me.

A big thank you to my own family. To my parents who have supported me throughout my very long stint as a student and for encouraging me to not settle for something I don't really love. Without that advice I probably would not be writing this thesis. Thank you to my brother David, I love our car ride therapy sessions and how you asked just the right amout of questions about my PhD, which was very few.

And finally thank you Cian, who has had to bear the brunt of many of the downs that have come with trying to complete this PhD. I can't put into words how much your support has meant to me. Thank you for all the lifts, dinners, treats, and cups of tea, for making sure I drank enough water, for putting up with a load of boring weekends while I wrote, for doing all the grocery shopping, for all the IT support, for being a shoulder to cry on when I needed and making me laugh when I needed cheering up (although I really just made myself laugh because I'm so funny), for humouring me with my spur of the moment trips to West Cork, for learning quickly not to tell me to plan my day better when I had a bad day (like seriously!?), the list of things you have done to support me is endless and I am so grateful to have had you by my side through this. In the words of Elder Price, every dinner needs a side dish and you're the best damn side dish a girl could ask for.

Abbreviations and Acronyms

1D	One Dimensional
2D	Two Dimensional
3D	Three Dimensional
AAS	Atomic Absorption Spectroscopy
ADW	Artificial Drinking Water
Ag	Silver
AgCl	Silver Chloride
ASV	Anodic Stripping Voltammetry
AdSV	Adsorptive Stripping Voltammetry
Au	Gold
AuNP	Gold Nanoparticles
BBB	Blood Brain Barrier
Bi	Bismuth
CA	Chronoamperometry
CE	Counter Electrode
CNT	Carbon Nanotubes
CV	Cyclic Voltammetry
CSV	Cathodic Stripping Voltammetry
D	Diffusion
d	Inter-electrode Distance
DALYs	Disability-adjusted Life Years
DME	Dropping Mercury Electrode
DPASV	Differential Pulse Anodic Stripping Voltammetry
E	Applied Potential
E^0	Standard Potential
E_{eq}	Equilibrium Potential
E_{fin}	Final/Apex Potential
E_{ini}	Initial Potential
E_{pa}	Anodic Peak Potential
E_{pc}	Cathodic Peak Potential
ΔE_p	Peak Potential Difference
ΔE_{ohmic}	The Ohmic Drop

e^-	Electron
EPA	Environmental Protection Agency
F	Faraday's Constant
FCA	Ferrocene Carboxylic Acid
Fe	Iron
FEA	Finite Element Analysis
ΔG	Gibbs Free Energy
ΔG^o	Standard Gibbs Free Energy
GC	Generator-Collector
H^+	Hydrogen Ion
H_2O	Water
H_2SO_4	Sulphuric Acid
HCl	Hydrochloric Acid
HER	Hydrogen Evolution Region
HfO_2	Hafnium Oxide
HMDE	Hanging Mercury Drop Electrode
HOMO	Highest Occupied Molecular Orbital
i_0	Exchange Current
i_b	Backward Current
i_f	Forward Current
i_{net}	Net Current
i_{pa}	Anodic Peak Current
i_{pc}	Cathodic Peak Current
i_{col}	Collector Current
i_{gen}	Generator Current
ICP-MS	Inductively Coupled Plasma – Mass Spectroscopy
IDE	Interdigitated Electrode
IHP	Inner Helmholtz Plane
IPA	Iso-propyl Alcohol
IPE	Ideal Polarizable Electrode
IUPAC	The International Union of Pure and Applied Chemistry
IQ	Intelligence Quotient
J	Dimensionless Flux
k_0	Heterogeneous Rate Constant

k_b	Backward Heterogeneous Rate Constant
k_f	Forward Heterogeneous Rate Constant
$KAg(CN_2)$	Potassium Silver Cyanide
$KAu(CN_2)$	Potassium Gold Cyanide
KCl	Potassium Chloride
LOD	Limit of Detection
LSV	Linear Sweep Voltammetry
LUMO	Lowest Unoccupied Molecular Orbital
m_o	Mass Transfer Coefficient
MDA	Microdisc Array
N	Collection Efficiency
n	Number of Electrons in a Reaction
NaOH	Sodium Hydroxide
NHE	Normal Hydrogen Electrode
NPG	Nanoporous Gold
O	Oxidation
O_2	Oxygen
O_{bulk}	Oxidised in the Bulk Solution
O_{surf}	Oxidised at the Electrode Surface
O’	Oxidised Species that has been Chemically Changed
O'_{ads}	Oxidised Species that is Adsorbed onto the Surface of the Electrode
OH^-	Hydroxyl Anion
OHP	Outer Helmholtz Plane
Pb	Lead
PBS	Phosphate Buffered Saline
ppb	Parts Per Billion
ppm	Parts Per Million
Pt	Platinum
PSV	Potentiometric Stripping Voltammetry
PTFE	Polytetrafluoroethylene
Q	Charge
R	Reduction
R_{bulk}	Reduction in the Bulk Solution

R_{surf}	Reduction at the Electrode Surface
R’	Reduction Species that has been Chemically Changed
R'_{ads}	Reduction Species that is Adsorbed onto the Surface of the Electrode
R	Gas Constant
R_c	Redox Cycles
R_u	Uncompensated Resistance
RE	Reference Electrode
RHE	Reversible Hydrogen Electrode
S	Sensitivity of the Electrode
SD	Standard Deviation
SAM	Self-Assembled Monolayers
SCE	Saturated Calomel Electrode
SEM	Scanning Electron Microscope
SF	Shielding Factor
SHE	Standard Hydrogen Electrode
SiN_x	Silicon Nitride
SiO2	Silicon Dioxide
SPE	Screen-printed Electrodes
SWV	Square Wave Voltammetry
SWASV	Square Wave Anodic Stripping Voltammetry
T	Temperature
Ti	Titanium
UPD	Underpotential Deposition
WE	Working Electrode
WHO	World Health Organisation
α	Transfer Coefficient
δ	Diffusion Layer Thickness
η	Overpotential
Φ	Collection Coefficient

To my family

Table of Contents

Chapter 1 **Introduction 20**

1.1 Overview of Fundamental Electrochemistry Concepts 21

1.1.1 Experiment Set-up 21

1.1.2 Electron Transfer 28

1.1.3 Faradaic and Non-faradaic Processes 32

1.1.4 Factors Affecting the Faradaic Response 35

1.1.5 Electrochemical Techniques 42

1.1.6 Electrochemistry at Microelectrodes 47

1.2 Finite Element Simulations 53

1.2.1 COMSOL Multiphysics® 53

1.2.2 Mass Transport at Microelectrodes 56

1.2.3 Diffusion Domain Approach 58

1.2.4 Finite Element Method 59

1.3 Detection of Lead in Water 61

1.3.1 A review of Sensors Used for the Detection of Lead in Tap Water 62

1.4 Thesis Objectives 77

1.5 References 79

Chapter 2 **Electrode Design, Simulation, Fabrication & Characterisation 89**

2.1 Introduction 90

2.2 Experimental 92

2.2.1 Finite Element Simulations 92

2.2.2 Electrode Design and Fabrication 92

2.2.3 Electrochemical Cell Set-up 95

2.2.4 Microscopic Characterisation 96

2.2.5 Electrochemical Characterisation 96

2.3 Results 98
2.3.1 Finite Element Simulations 98
2.3.2 Microscopic Characterisation 118
2.3.3 Electrochemical Characterisation 120
2.4 Conclusion 129
2.5 References 131
Chapter 3 **Electrode Surface Optimisation for the Detection of Lead 132**
3.1 Introduction 133
3.2 Experimental 134
3.2.1 Electrochemical Cell Set-up, Microscopic and Electrochemical Analysis 134
3.2.2 Electrode Modification with Nanoporous Gold 134
3.2.3 Electrochemical Detection of Lead at Micro-Disc and IDE Arrays 139
3.3 Results and Discussion 141
3.3.1 Analysis at Gold Micro-Disc Arrays 141
3.3.2 Analysis at Nanoporous Gold Modified Interdigitated Electrode Arrays 156
3.4 Conclusions 164
3.5 References 166
Chapter 4 **Electrochemical *In Situ* pH Control for the Detection of Lead in Water 168**
4.1 Introduction 169
4.2 Experimental 171
4.2.1 Electrode Design and Fabrication 171
4.2.2 Electrochemical Cell Set-up, Microscopic and Electrochemical Analysis 171
4.2.3 Electrode Modification with Nanoporous Gold 171
4.2.4 Electrochemical Detection of Lead 171

4.2.5 pH Adjustment of Water Samples 171
4.2.6 Electrochemical *In Situ* pH Control 172
4.3 Results and Discussion 173
4.3.1 Monitoring pH Based on the Potential of the Gold Oxide Reduction Peak 173
4.3.2 Establishing Protonator Potential for *In Situ* pH Control 175
4.3.3 Detection of Lead in Tap Water with Chemical pH Control 179
4.3.4 Detection of Lead in Tap Water with Electrochemical *In Situ* pH Control 182
4.4 Conclusions 188
4.5 References 189
Chapter 5 **Summary and Future Work 190**
5.1 Summary 191
5.2 Future Work 193
Appendices 195
A.1 Publications 196
A.2 Invention Disclosure Forms 196
A.3 Presentations 196

Chapter 1 Introduction

1.1 Overview of Fundamental Electrochemistry Concepts

Broadly speaking, electrochemistry is the study of the relationship between electrical energy and chemical reactions. Specifically, it constitutes the study of electrical parameters, such as current, potential, or charge and their relationship to chemical changes. The measurement of these parameters has a vast range of analytical applications, including environmental monitoring, industrial quality control, or biomedical analysis.[1] When referring to electrochemical sensors, it is the electron transfer occurring at an electrode-solution interface by application of a potential that is typically of interest.[2] This phenomenon is known as electrolysis, the output of which produces positive or negative currents. Common electrochemical reactions include: a simple electron transfer from an electrode to an electroactive species in solution (or vice-versa)[3], a change of the electrode surface, e.g., formation of an oxide layer or deposition of a metal[4], or a change of physical state, e.g., from liquid to gas.[5, 6] A more detailed explanation is given step-by-step in this chapter.

1.1.1 Experiment Set-up

The three most common types of electrode set-ups that can be used in electrochemical experiments utilise: two, three, and four-electrodes. The two-electrode set-up is the simplest. However, this set-up suffers some drawbacks in that it can be difficult to maintain and control potential at the electrodes.[7] The three-electrode set-up solves the issues encountered with the two-electrode configuration and is generally the most popular experimental set-up employed for electrochemical studies. It consists of a working electrode (WE), counter electrode (CE), and reference electrode (RE) immersed in an electroactive solution. All three electrodes are electrically connected to a device known as a potentiostat. The potentiostat allows for the application of a potential or a current to

the electrochemical cell, while also measuring the current or potential response arising from electrochemical reactions occurring at the interface between the working electrode and solution. All potentials are controlled and reported with respect to the reference electrode. The measured current passes between the working and counter electrode through the solution. The potentiostat is connected to a computer or alternative portable interfaces such as a tablet or smart phone to acquire data. The electrochemical cell may be placed in a Faraday cage to minimise background electrical noise. A Faraday cage is typically made of conductive material, which allows any electrical interference to dissipate around the exterior of the cage preventing significant electromagnetic noise from reaching the electrolytic cell. This is particularly important when working with micro- and ultramicro-electrodes, which will be discussed in 1.1.6. An example of a three-electrode electrochemical experimental set-up is illustrated in Figure 1.1.

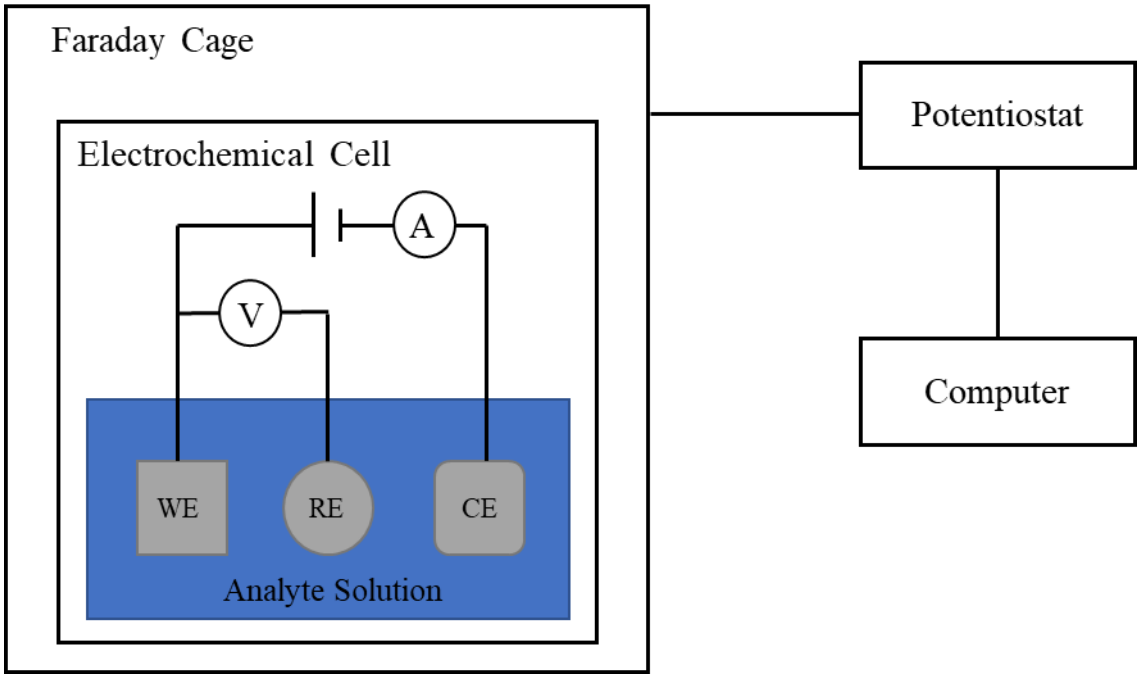


Figure 1.1 Schematic diagram of a standard three-electrode electrochemical cell within a Faraday cage, connected to a potentiostat and a computer. WE, RE and CE are the working, reference, and counter electrodes, respectively.

1.1.1.1 *The Working Electrode (WE)*

The WE, sometimes referred to as an indicator electrode, is where the reaction of interest occurs. It is the electrode where the potential is controlled and measured. The WE needs to be conductive and, when reaction of the electrode is not desired, inert in the potential region of interest. The WE also must have a clean reproducible surface, so in some cases, electrode pre-treatment is required before carrying out analysis. The material, size, and shape of the WE depend on its application. Mercury was the first material used as a WE, as the dropping mercury electrode (DME). The DME was ideal as each drop had a smooth and uncontaminated surface free from any adsorbed analyte or impurity. The self-renewing electrode did not need to be cleaned or polished. However, there were several disadvantages associated with this electrode. It has a constantly changing surface area. Its time scale is controlled by the lifetime of the drop, which cannot be varied conveniently outside of the range 0.5 to 10 s. Since the creation of the DME, is has since been replaced by the hanging mercury drop electrode (HMDE) and more recently by thin film mercury electrodes.[8] Mercury electrodes have an inability to operate at potentials much more positive than 0.0 V vs saturated calomel electrode (SCE). The anodic limit which arises from the oxidation of mercury, is always near that potential, although it depends somewhat on the medium.[9] Mercury is poisonous and requires careful handling. Additionally due to environmental concerns, mercury electrodes have become less favoured for WE material.[10] Other WE materials that have replaced DMEs include the noble metals (especially gold and platinum), carbon (including pyrolytic carbon, glassy carbon, carbon paste, nanotubes, and vapour-deposited diamond), liquid metals (mercury amalgams), and semiconductors (indium-tin oxide, Si). Working electrodes can be chemically modified to increase their sensitivities toward specific species (i.e., become chemical sensors) or to decreases the potential required to drive a particular reaction (i.e.,

catalysis).[2, 11, 12] Chemically modifying an electrode involves coating the electrode surface with a mono-molecular, multi-molecular, ionic or polymeric film which alters the electrochemical, optical or other properties of the electrode. Some commonly used chemical modifiers include conducting polymers, self-assembled monolayers (SAM) layers, carbon nanotubes (CNT), and gold nanoparticles (AuNP). Other advantages of chemically modifying electrodes include increases selectivity, increases chemical and electrochemical stability, larger usable potential window, and resistance to biofouling.[13] In this thesis, all the electrodes used are made of inert materials to prevent interfering reactions with species being analysed.

1.1.1.2 *The Counter Electrode (CE)*

The CE, sometimes known as an auxiliary electrode, provides an electron sink or source to avoid excess current going to the reference electrode – it is a conductor that completes the cell circuit. A set voltage is applied to the electrochemical cell through the CE. The CE is generally chosen to be inert under the reaction conditions, such as a platinum wire or graphite rod. [2, 14]

1.1.1.3 *The Reference Electrode (RE)*

The RE provides a stable and reproducible potential, against which the potential of the WE is measured. For the RE to perform as such, it must be an ideal nonpolarizable electrode; the type of electrode that does not change its potential upon passage of current. The opposite, an ideal polarizable electrode exhibits a large change in potential for an extremely small change in current, i.e., a WE.[2] The reaction governing the RE must be reversible, permitting a potential to be calculated from the Nernst equation, as well as the capability to recover its potential after a current stress.[10] The internationally accepted primary reference electrode is the standard hydrogen electrode (SHE) or normal hydrogen

electrode (NHE). [15-17] It provides an absolute scale for electrochemical reactions and is the determination of the standard potential of other reference electrode systems. The reaction for this electrode has a standard potential of 0 V at all temperatures by convention.

$$2H^+ + 2e^- \rightleftharpoons H_2, \qquad E^o_{Pt/H_2,H^+} = 0.000\ V \tag{1.1}$$

This electrode consists of a platinum wire, submerged in an acid over which hydrogen gas is constantly bubbled. The constant need for hydrogen bubbling makes the handling and maintenance of these electrodes cumbersome and can restrict their use.[17] The most commonly used alternative REs include saturated calomel electrodes (SCE) and silver/silver chloride electrode (Ag/AgCl). The SCE electrode is one of the most common REs and has a fixed, well-known, and very reproducible potential. It consists of platinum wire submerged in a saturated potassium chloride solution. The wire is also partially submerged in liquid mercury and coated with a mercury, calomel, and potassium chloride (KCl) paste. The reaction that governs the SCE has a standard potential of 0.268 vs. NHE.[10]

$$Hg_2Cl_2 + 2e^- \rightleftharpoons 2Hg + 2Cl^-, E^o_{Hg/Hg_2,Cl_2} = 0.268\ vs.NHE \tag{1.2}$$

The Ag/AgCl electrode is the most regularly used RE due to its simplicity, inexpensive design and most importantly, non-toxic components. SCE electrodes contain mercury making the electrode unsafe if broken and difficult to dispose of. The Ag/AgCl electrode is a much safer and environmentally friendly option. This electrode consists of a silver wire, coated with silver chloride submerged in a saturated KCl solution. The saturated KCl is used to minimise and stabilise the junction potentials between the reference

electrode and the sample solution. A glass frit allows ionic transport into the electrode from the solution. The reaction that governs this RE has a standard potential of 0.222 V vs NHE.[10]

$$AgCl + e^- \rightleftharpoons Ag + Cl^-, E^o_{Ag/AgCl} = 0.222\,V\ vs.NHE \quad (1.3)$$

The simplicity of the Ag/AgCl electrode lends itself well to microfabrication for incorporation into sensors. However, the requirement for a millilitres scale sample volume, limits its use with micro/nano scale devices. In these cases, a noble electrode (e.g., platinum, silver, or gold) may be substituted for the reference electrode and is referred to as a quasi- or pseudo-reference electrode.[18, 19] The term pseudo indicates that the noble metal is stable only over a short period of time and calibration is required prior to every measurement.[20] Alternatively, when regular calibration is not possible, an internal reference solution can be used. An internal reference solution can be one that contains a well-characterised redox couple, so any potential shifts can be accounted for and corrected.

1.1.1.4 *The Potentiostat*

The potentiostat consists of an electronic circuit that controls the voltage difference between the WE and RE, which has a constant potential. This control is achieved by applying a current between the WE and the CE. The current value changes based on the desired potential at the WE. A simplified schematic of a potentiostat for a three-electrode set-up highlighting the five main components of a potentiostat, one of them being the electrochemical cell itself can be seen in Figure 1.2. It is worth mentioning the bipotentiostat here, a bipotentiostat is a potentiostat that can control two working electrodes.

The signal generator is a computer interface used to control the voltage source. A digital signal from the computer is converted to an analog signal (voltage) which is applied to the electrochemical cell. These signals can have varied complexities depending on the electrochemical application.

The current amplifier controls the voltage of the cell by comparing the measured voltage with the desired voltage input by the signal generator. The potential measured at the RE is fed back to the negative input of the control amplifier. This is known as the "negative feedback loop", which results in the control amplifier being able to change its output and maintain a potential difference corresponding to the voltage input by the signal generator.[21]

The electrometer uses an amplifier to determine the potential difference between the RE and WE. This measurement provides a measured potential that feeds into the current amplifier. It also provides the user with the cell potential measurement at any given time.

The I/E converter also uses an amplifier, however, in this case it is used to measure the current flow in the electrochemical cell. This is achieved by measuring the potential at the WE before and after it passes through the resistor (R_m). The potential drop observed after the resistor can be used to determine the current in the electrochemical cell.

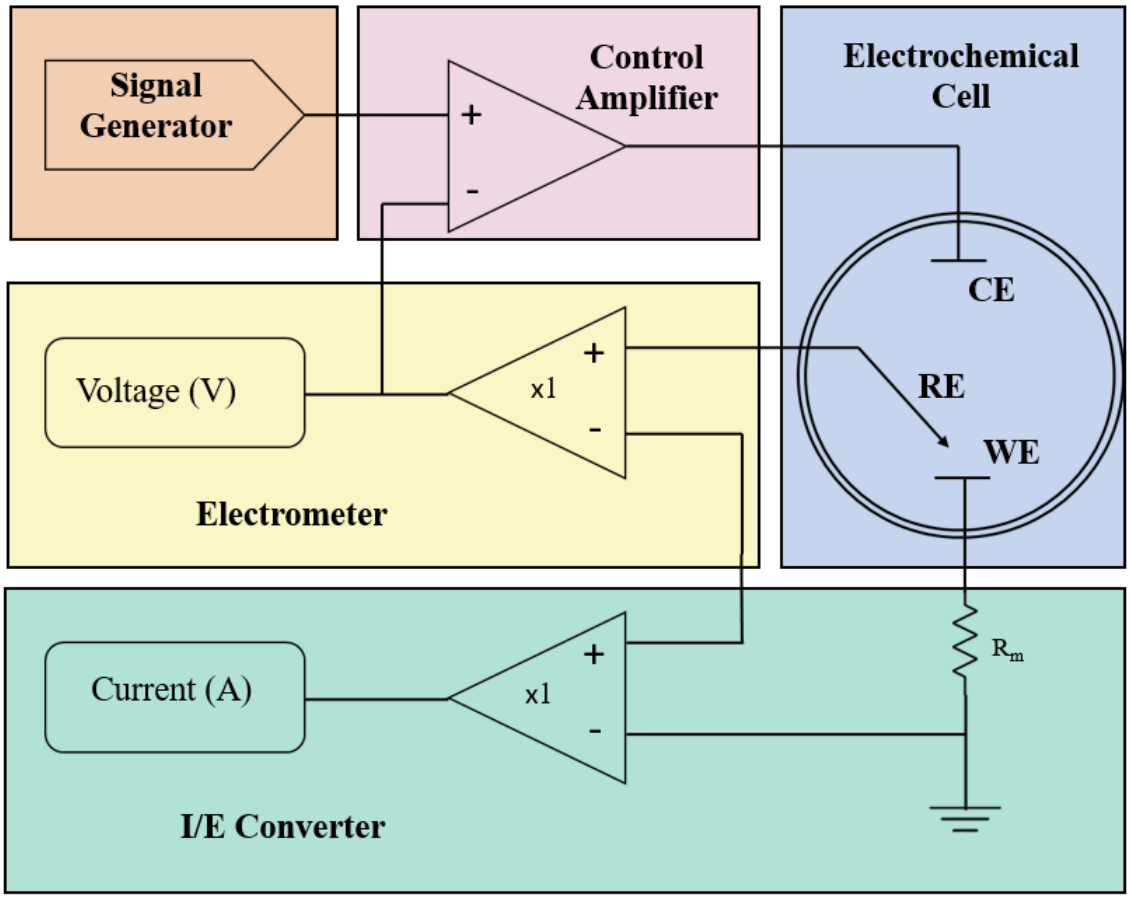


Figure 1.2 A simplified schematic diagram of a potentiostat for a three-electrode set-up, reproduced from[14].

1.1.2 Electron Transfer

As previously mentioned, electrochemistry is the study of the relationship between electrical energy and chemical reactions. Most commonly, the electron transfer occurs at an electrode-solution interface by application of a specific potential. In all cases, electrochemical reactions are invariably reduction (a gain of electron) or oxidation (a loss of electron) reactions, which are typically represented by the following equation:

$$O + ne^- \rightleftharpoons R \qquad 1.4$$

where O is the oxidised species, R is the reduced species, and *n* is the number of electrons exchanged between O and R. Such a reaction will occur in a potential region that makes the electron transfer thermodynamically or kinetically favourable.[1] Potential is the force required to move the electrons between the electron/solution interfaces. Where the potential applied causes a reduction the electrode is known as a cathode and where the potential causes an oxidation it is known as an anode.

Electron movement can occur between the metal electrode and a solution species when the cell potential is sufficient to force the electron to move. For an electron from the electrode to move, the energy level in the electrode must match the energy level of the vacant orbital of the solution species. Conversely, the electrode energy levels must be low enough so that it becomes more favourable for an electron in an orbital of the solution species to move to the electrode. The solution species will have a distinct energy associated with its highest molecular orbital (HOMO), and its lowest unoccupied molecular orbital (LUMO). These are the orbitals that an electron can be taken from or donated to, respectively. The energy required to promote an electron from a HOMO to a LUMO is known as the HOMO-LUMO gap. The electrode has a continuum of energy levels rather than discreet energy levels. These energy levels mark the boundary between occupied and unoccupied states. The critical potential at which electrons can transfer between the electrode and solution species is related to the standard potential, E^o, for the specific chemical substance in the system. When there is no applied potential, E, the electrode does not have enough energy to promote an electron to the LUMO of the solution species. At the same time the electrode energy level is typically not low enough to allow electron transfer from the solution species due to the energy barrier. As a result, the reactions are thermodynamically unfavourable and will not happen. Where E is applied, the energy level of the electrode moves. Application of E lower than E^o, causes

an increase in the energy level of the electrode so that it is greater than the LUMO of the solution species. The electron transfer from the electrode to the LUMO of the solution is now thermodynamically favourable and proceeds as a reduction reaction. Where E is greater than E^{o}, the energy level of the electrode is reduced. In this case it is now thermodynamically favourable for an electron from the HOMO of the solution species to move into the electrode resulting in an oxidation reaction. This process is also illustrated in Figure 1.3.[15, 22]

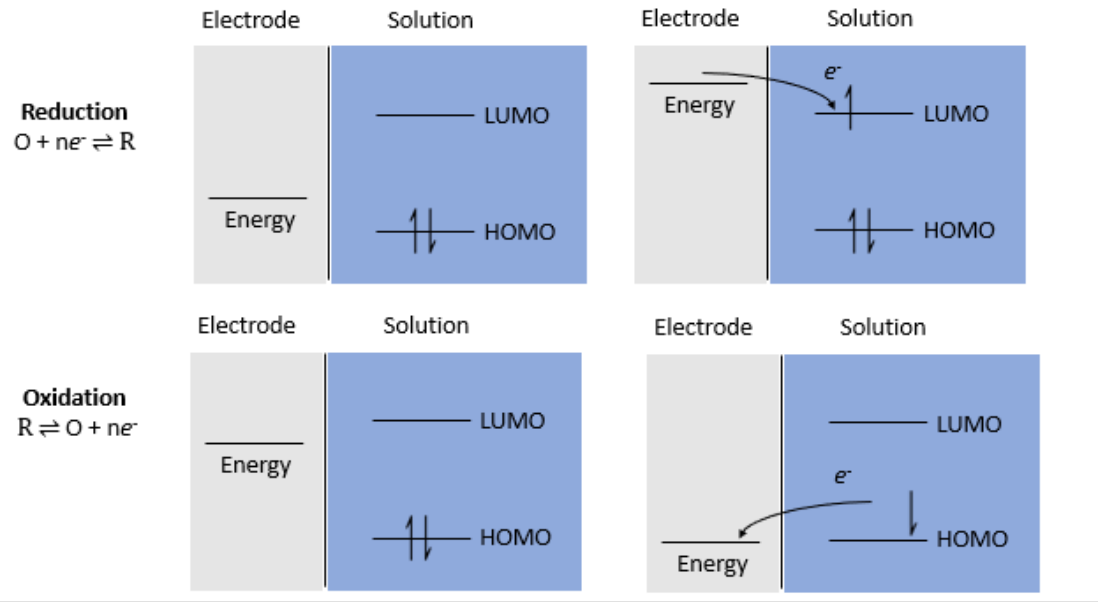


Figure 1.3 Diagram of electron transfer and energy levels at an electrode/solution interface for reduction and oxidation processes. LUMO is the lowest unoccupied molecular orbital and HOMO is the highest occupies molecular orbital. An applied voltage is required to surmount the energy barrier and allow electron transfer.

As previously mentioned, such a reaction will occur in a potential region that makes the electron transfer thermodynamically or kinetically favourable. The application of a potential to an electrode makes the reaction thermodynamically favourable which can be determined by the change in Gibbs free energy (ΔG):

$$\Delta G = \Delta G^{o} + RT\ln\frac{[R]}{[O]} \quad 1.5$$

where ΔG^{0} is the standard Gibbs free energy (J mol^{-1}), *R* is the gas constant (8.3145 J mol-1 K-1) and *T* in the temperature (K). The ratio of reduced to oxidised species can be related to the Gibbs free energy change (ΔG), from which the potential, *E* (V) can be derived:

$$\Delta G = -nFE \quad 1.6$$

where *n* is the number of electrons involved in the reaction, *F* is Faraday's constant which is related to the total charge of the reaction of product formed (96,487 C mol^{-1} for n=1). This equation can also be written with respect to the standard potential, E^{0}.

$$\Delta G^{o} = - nFE^{o} \quad 1.7$$

Where values for ΔG are negative, reactions occur spontaneously. Where ΔG values are positive, reactions are not spontaneous and therefore required application of voltage to proceed. From equations 1.6 and 1.7, the cell potential can be calculated as:

$$-nFE = -nFE^{0} + RT\ln\frac{[R]}{[O]} \quad 1.8$$

which simplifies to the Nernst equation:

$$E = E^o + \frac{RT}{nF}\ln\frac{[R]}{[O]}$$

1.9

1.1.3 Faradaic and Non-faradaic Processes

Two types of processes occur at electrodes. One type comprises of electron transfer reactions as described in 1.1.2 and obeys Faraday's law of electrolysis[2]:

$$Q = nNF$$

1.10

where Q is the charge (C), n is the number of electrons involved in the reaction, N is the number of moles (mol) of analyte and F is Faraday's constant (96487 C mol^{-1}).[1] These processes generate faradaic current which is of great interest in electrochemistry. Under some conditions, a given electrode-solution interface will show a range of potentials where no charge transfer reactions occur because such reactions are thermodynamically or kinetically unfavourable. However, the currents observed at a working electrode may not only arise from charge transfers but in fact may arise from adsorption and desorption processes that can take place at the electrode surface. The contributions from the latter are the second type of process that occur at electrodes. These processes do not obey Faraday's law of electrolysis and are therefore known as non-faradaic.[15, 23]

The faradaic current is a direct measure of the rate of electron transfer. The resulting current-potential plot, known as a voltammogram, is a display of current signal versus excitation potential. The exact shape and magnitude of the voltammetric response is governed by the processes involved in the electrode reaction. The total current is the summation of the faradaic currents for the sample and electrolyte solutions as well as the non-faradaic charging background currents, which will be discussed shortly.[1]

In an electrochemical cell where only, non-faradaic current is measured an electric field develops when a potential is applied. This causes charges to accumulate at the electrode-solution interface according to[15]:

$$\frac{Q}{E} = C \qquad 1.11$$

where Q is the charge stored at the electrode-solution interface (in Coulombs, C), E is the potential across the electrode-solution interface (in Volts, V) and C is the capacitance (in Farads, F). The electrode-solution interface can be viewed as a capacitor. In other words, the application of potential results in the formation of a specific interfacial region known as the double layer. Its capacitance and structure depend on several parameters such as: electrode material, solvent, supporting electrolyte concentration, extent of specific adsorption of ions and molecules, and temperature.[15]

Detailed descriptions of double-layer models can be found in the literature, e.g., the Helmholtz[24], the Gouy and Chapman[15, 23], and the Stern models[14, 16]. The first and simplest double layer model, created in 1879 is the Helmholtz model. In this model, the double layer is treated as a parallel plate where the charge at the electrode surface is neutralised by opposite sign counterions in solution at a set distance away from the surface of the electrode. The surface charge potential is linearly dissipated with distance. The distance will be that to the centre of the counterions, i.e., their radius. The line drawn through the centre of each counterion marks the boundary known as the Outer Helmholtz Plane (OHP) and the region within it is the electrical double layer, see Figure 1.4. However, the Helmholtz model is limited as it hypothesizes rigid layers of opposite charges which does not occur in nature. The Gouy-Chapman model proposed a diffuse charge model of the double layer, wherein there is a rigid charged surface at the electrode

with a cloud of oppositely charged ions in solution. The concentration of the oppositely charged ions decreases with distance from the surface. Inaccuracies in this model occur as experimentally the double layer thickness is found to be somewhat greater than calculated. The most commonly used of these model is the combination of the Helmholtz and Gouy-Chapman models, which was suggested by Stern.[15, 23]

In this simplified model, the electrical double layer is composed of the electrical charge at the surface of the electrode itself and the charge of the ions disbursed in the solution is at a small distance from the electrode surface. This double layer is formed when a potential is applied to the electrode and causes a charging (non-faradaic current) to pass through the cell. The double layer formed at the metal surface in solution considers two planes defining two layers, see Figure 1.4. The first layer consists of solvent molecules and specifically adsorbed (desolvated) ions. The locus of the electrical centres of this layer is termed the boundary of the inner Helmholtz plane (IHP). The layer between the electrode surface and the IHP is the inner layer, where the solvent molecules and ions are specifically adsorbed onto the electrode surface via chemical interaction. The second layer consists of solvated ions. The locus of the electrical charge from these ions is known as the outer Helmholtz plane (OHP). The non-specifically adsorbed solvated counter ions are attracted to the positively (or negatively) charged electrode surface via Coulomb force. Between the OHP and the bulk solution, non-specifically adsorbed species spread in an outer diffuse layer, of which the thickness depends on the total ionic concentration of the solution. The presence of the double layer is responsible for non-faradaic charging current, also known as capacitive current, i.e., not related to electron transfer reactions. Generally, these capacitive currents are negligible. However, there are some instances where they can cause an interference, such as at low concentrations or at fast scan rates.

Consequently, some methods may be used in electrochemistry to supress or minimise capacitance. [14, 16]

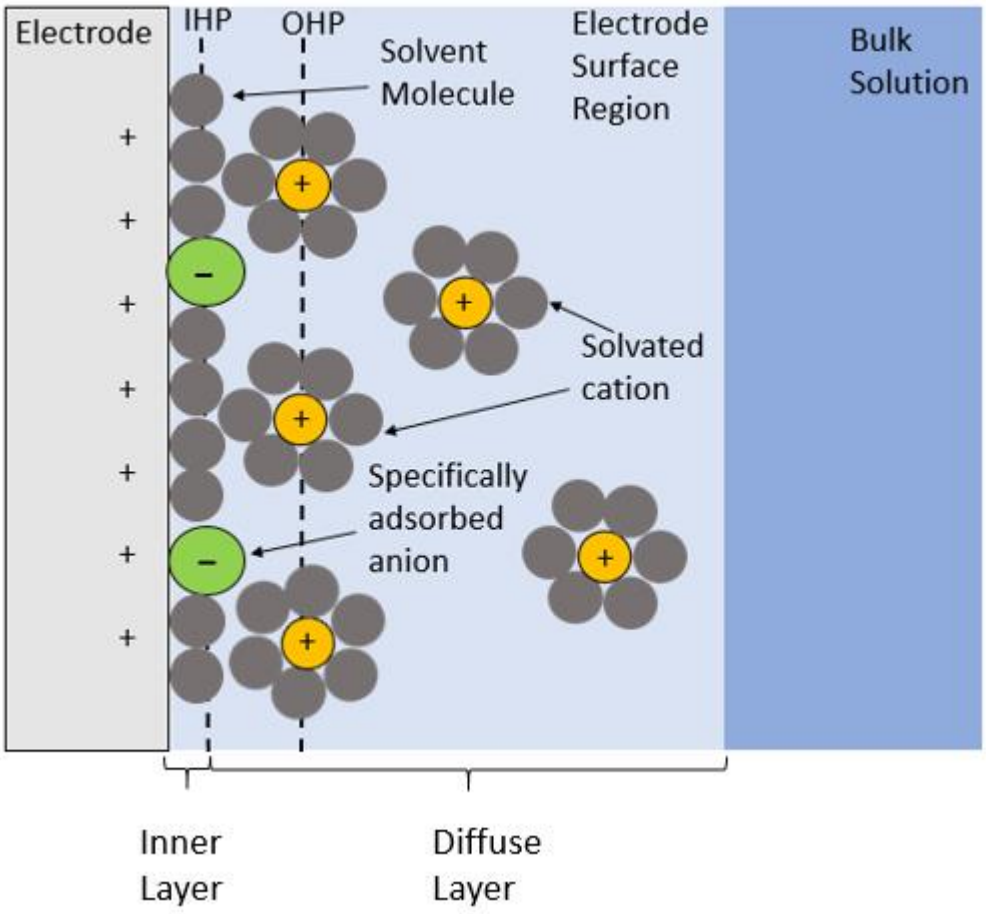


Figure 1.4 Simplified Model of the double layer region with specifically adsorbed anions and solvent molecules in the inner layer, and solvated cations in the diffuse layer. IHP and OHP are the inner and outer Helmholtz planes, respectively.

1.1.4 Factors Affecting the Faradaic Response

As described in 1.1.2, a typical electrochemical reaction involves electron transfer between an electrode and redox species in solution resulting in current flow. The steps involved in this process are highlighted in Figure 1.5. These include mass transfer from the bulk solution to the electrode surface; chemical reactions that occur in the electrode surface region; surface reactions, such as adsorption and desorption, and finally, electron transfer. The slowest of these processes is known as the rate determining step and

dominates the overall reaction rate. The most common processes that limit the reaction are the rate of electron transfer and the rate of mass transfer.

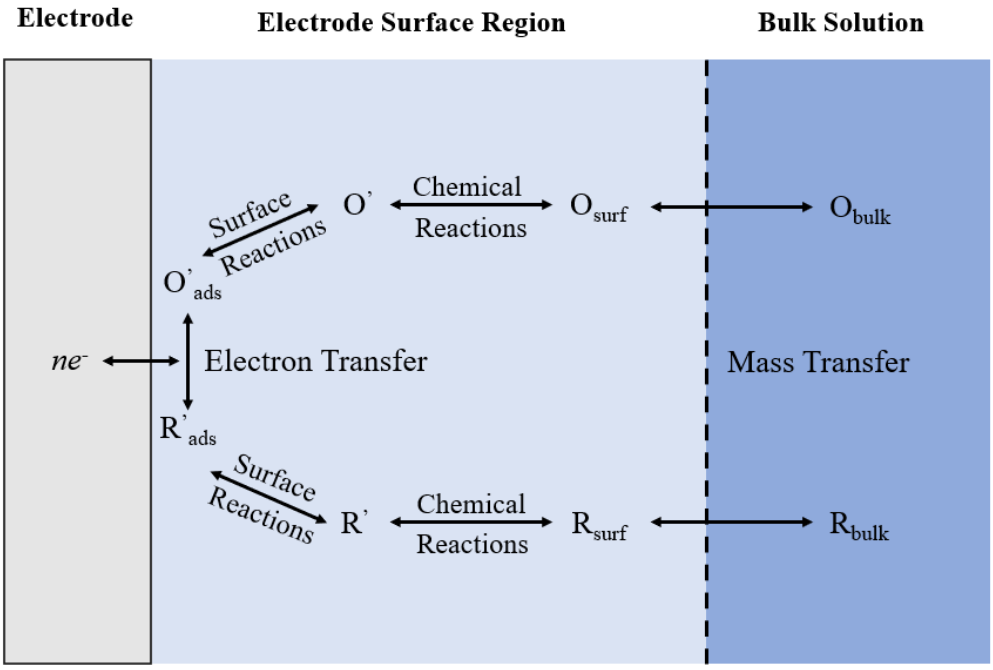


Figure 1.5 Schematic of the steps involved in a Faradaic reaction. O and R are a species in an oxidised and reduced state, respectively. O_{bulk} is oxidised in the bulk solution, O_{surf} is oxidised species at the electrode surface, O' is oxidised species that has been chemically changed and O'_{ads} is oxidised species that is absorbed on the surface. The same notation applies to R the reduced species.

1.1.4.1 *Electron Transfer*

For many electrochemical systems, experimental current of a one-step, one-electron mechanism can be described using the Butler Volmer kinetic model[1, 2, 15]. To explain this, we consider again the electron reaction from Eq. 1.4: $O + ne^- \rightleftharpoons R$, where the reduction reaction is the forward reaction (*f*) and the oxidation is the backward reaction (*b*). The rate of the forward reaction v_f [M s^{-1}] is first order with respect to O:

$$v_f = k_f C_O(0,t)$$

1.12

While that of the reversed reaction v_b is first order with respect to R:

$$v_b = k_b C_O(0,t)$$

1.13

Where k_f and k_b are the forward and backward heterogeneous rate constant [cm s^{-1}], respectively and Co(0,t) and Cr(0,t) are concentration of oxidised and reduced species, respectively at a distance 0 from the electrode at time t. The net conversion rate of O and R is given by:

$$v_{net} = v_f - v_b = k_f C_o(0,t) - k_b C_R(0,t)$$

1.14

For an electrode reaction, equilibrium is characterised by Nernst equation, which links the electrode potential to the bulk concentration of the participants. For the electron transfer reaction (Eq. 1.4), this equation is:

$$E = E^{0'} + \frac{RT}{nF} ln \frac{C_o^*}{C_R^*}$$

1.15

where C_o^* and C_R^* are the bulk concentration and $E^{0'}$ is the formal potential.

The rate constants k_f and k_b depend on the operating potential according to the following exponential relationships:

$$k_f = k^O e^{\left[\frac{(-\alpha n F(E-E^0)}{RT}\right]}$$

1.16

$$k_b = k^0 e^{\left[\frac{(1-\alpha) n F(E-E^0)}{RT}\right]}$$

1.17

where k^0 [cm s^{-1}] is the heterogeneous rate constant and α is the transfer coefficient. The value $E - E^0$ is known as the overpotential (η) and is the difference between the standard potential and the of the reaction and the potential required to drive the reaction. For a non-spontaneous cell reaction to occur, an overpotential must be applied. Overall, Eqs. 1.16 and 1.17 indicate that by changing the applied potential we influence k_f and k_b in an exponential fashion. Positive and negative potentials thus speed up oxidation and reduction reactions, respectively. As discussed in section 1.1.1, for an oxidation, the energy of the electrons in the donor orbital of R must be equal to or higher than the energy of electrons in the electrode. For reduction, the energy of the electrons in the electrode must be higher than their energy in the receptor orbital of R.

The forward and backward currents are proportional to v_f and v_b, respectively:

$$i_f = nFAv_f$$

1.18

$$i_b = nFAv_b$$

1.19

The overall current is given by the difference between the current due to the forward and backward reactions:

$$i_{net} = i_f - i_b = nFA[k_f C_O(0,t) - k_b C_R(0,t)]$$

1.20

By substituting the expressions of k_f and k_b, the Butler-Volmer equation is obtained:

$$i = nFAk_0 \left\{ c_O(0,t) e^{\left[\frac{-\alpha nF\left(E-E^0\right)}{RT}\right]} - C_R(0,t) e^{\left[\frac{(1-\alpha)nF(E-E^0)}{RT}\right]} \right\}$$

1.21

Since the Butler-Volmer equation describes the current-potential relationships for the reactions controlled by the rate of electron transfer, the net current depends on both the operating potential and the surface concentrations of each form of the redox couple. The total is then a combination of the two. The exchange current, i_0, can be described by:

$$i_0 = FAk^0 C_O^{*(1-\alpha)} C_R^{*\alpha}$$

1.22

Substituting this into the current-potential characteristic equation and assuming that mass transfer effects are non-limiting (such that concentration at the electrode and the bulk are equal) gives the Butler Volmer equation[1, 2, 15]:

$$i = i_o \left[e^{\frac{-\alpha\eta F}{RT}} - e^{\frac{(1-\alpha)\eta F}{RT}} \right]$$

1.23

1.1.4.2 *Mass Transfer*

As outlined in Figure 1.5, mass transfer also plays an important role in Faradaic current response. A species needs to move into the electrode surface region for an electron transfer to occur, but also needs to move away after electron transfer. Consequently, the

faradaic current also depends on the rate of mass transport between the bulk and electrode surface region. If the rate of mass transfer is slow, fresh analyte will not move into the electrode surface region and the reacted analyte will not move away affecting the overall faradaic response. Mass transfer can be accomplished in three different ways and/or a combination of these modes: (a) *diffusion* – movement of species against a concentration gradient; (b) *migration* – movements of charged particles in an electric field; (c) *convection* – movement of species induced by stirring or density gradients.[25]

The Nernst-Planck equation[15] below relates to unidirectional (x) flux of a species j to diffusion, migration, and convection:

$$J_j(x) = D_j \frac{\partial C_j(x)}{\partial x} - \frac{z_i F}{RT} D_j C_j \frac{\partial \emptyset(x)}{\partial x} + C_j v(x) \qquad 1.24$$

where $J_j(x)$ (mol cm^{-2} s^{-1}) is a one dimensional flux for species j at distance x (cm) from the electrode; D_j (cm^2 s^{-1}), z_j and C_j (mol cm^{-3}) are the diffusion coefficient, the charge and the concentration for the species j, respectively; $v(x)$ (cm s^{-1}) is the rate with which a volume element moves in solution; $\partial C_j(x)/\partial x$ is the concentration gradient; and $\partial \phi(x)/\partial x$ is the potential gradient along the x-axis. In equation 1.24, the first term is concerned with the diffusion and is, in fact, Fick's first law (equation 1.25), the second term accounts for the migration of the species in the solution, and the last term represents the convection of the solution.[15, 25] In some cases, it is desirable to reduce the contribution for two of the three terms to simplify the equation. Migration effects can be minimised by adding an excess of electrolyte to shield electric field effects, higher than the concentration of the electroactive species. Convection can be mitigated by performing analysis in quiescent solutions. In these cases, mass transport is dependent entirely on diffusion. To minimise diffusion effects, solutions can be stirred, or flowed over the electrode at high rates. In

such cases, convection effects become so large that diffusion effects are comparably miniscule.[15]

It is most common however to minimise convection and migration so that diffusion is the only flux so that the equation becomes:

$$-J_0(x) = D_0 \frac{\partial C_0(x)}{\partial x}$$

1.25

This is known as Fick's law of diffusion[25] and shows that the flux of species (in this example species O), J_O, is proportional to the concentration gradient $\partial C_O(x)/\partial x$ for one-dimensional diffusion. Fick's second law predicts the change of concentration of species over time, which for one-dimensional diffusion is given by:

$$\frac{\partial C_O(x,t)}{\partial t} = D_O \frac{\partial^2 C_O(x,t)}{\partial x^2}$$

1.26

Carrying out an experiment where diffusion effects are the only form of flux, means that the diffusion coefficient becomes an important parameter. The potential applied does not directly impact diffusion. However, the resulting concentration gradient established at the electrode causes flux of species to counter the gradient. A larger gradient will result in more flux; therefore, the potential has an indirect effect on the diffusion of species. If the kinetics of the reaction are extremely fast, then the limiting factor will be the mass transfer. In such a case the current can be calculated by:

$$i = \frac{nFADC^*}{\delta}$$

1.27

The value δ is known as the diffusion layer thickness (cm) and C^* is the concentration (mol cm^{-3}). The diffusion layer thickness can be approximated by the following equation:

$$\delta = \sqrt{\pi D t} \tag{1.28}$$

Substituting this into equation 1.27 gives the Cottrell equation[15, 25]:

$$i(t) = \frac{nFAD^{\frac{1}{2}}C^*}{\pi^{\frac{1}{2}}t^{\frac{1}{2}}} \tag{1.29}$$

This allows for the calculation of the current associated with a diffusionally controlled process, at a given time. Capacitive currents can be distinguished from faradaic currents in the total current due to the fact capacitive current decay more quickly (t^{-1}) than the faradaic currents ($t^{-1/2}$).

1.1.5 Electrochemical Techniques

1.1.5.1 *Cyclic Voltammetry (CV)*

CV is a very popular electrochemical technique for investigating electrochemical systems where a potential is applied to the system and a current is measured. The current response is generated by the application of a triangular potential waveform as highlighted in Figure 1.6(a). A forward and reverse scan are produced by this waveform. The applied potential is swept linearly from an initial potential, E_{in}, to an apex potential E_{fin}, and reversed back to generally the initial potential.

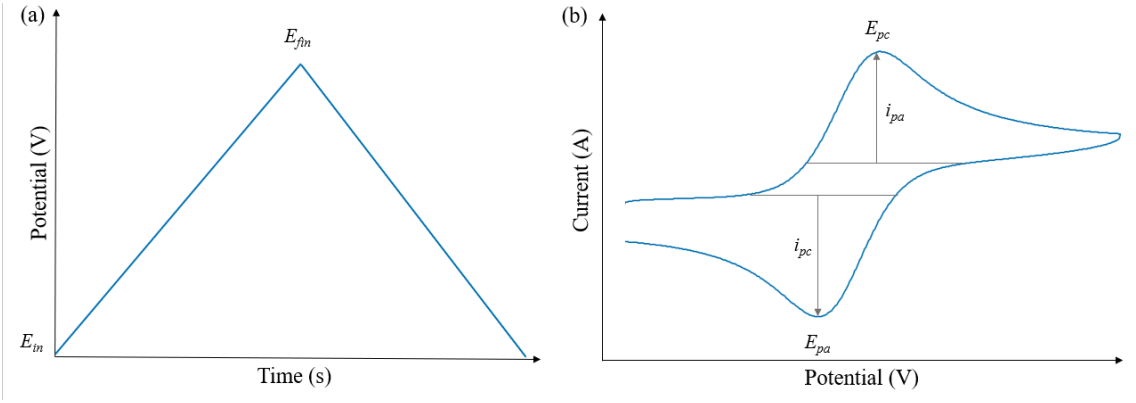


Figure 1.6 Schematic diagrams of (a) the potential wave form of cyclic voltammetry and (b) the resulting cyclic voltammogram.

The linear sweep rate is known as scan rate and can vary from microV/s to thousands of V/s. The scan rate sets the timescale of the experiment. The initial potential is set at a potential where no redox reaction occurs and is swept towards the potential region where the electrochemical reaction of interest takes place. For instance, in a redox reaction, the potential is swept positively or negatively past the standard potential for a redox couple, E_0'. An oxidation or a reduction reaction will occur on either the forward or reverse scan, depending on the redox species present. Useful parameters for examining the reversibility of these redox systems are the cathodic peak potential E_{pc}, the anodic peak potential E_{pa}, the cathodic peak current i_{pc}, and the anodic peak current i_{pa}, as highlighted in Figure 1.6(b). The reversibility can be determined from the peak currents by calculating the ratio between i_{pc} and i_{pa}; a result of 1 indicates a reversible reaction. For the peak potentials, the difference between peak potentials, ΔE_p, in a Nernstian reaction at 25 °C is expected to be 0.059/n, where n is the number of electrons involved in the half-reaction. Higher ΔE_p indicates irreversibility due to slow electron transfer kinetics. Reaction rates and mechanisms can also be determined using CV. The limiting step of the reaction can be easily determined from the shape of the resultant voltammogram, particularly when the species investigated does not undergo a chemical change or surface binding prior to

charge transfer. Reactions that give rise to a peak shaped voltammogram in these cases are generally limited by mass transfer to the electrode, thus they are termed diffusion-limited. Voltammograms where a current plateau is observed tend to result from steady-state mass transfer, hence these reactions are not limited at the electrode surface. Relationships between peak current and concentration can be established if the diffusion coefficient is known, and similarly the diffusion coefficient can be calculated when the concentrations are known by using the Randles-Sevcik equation[26]:

$$i_p = (2.69 \times 10^5) n^{\frac{3}{2}} A C D^{\frac{1}{2}} v^{\frac{1}{2}} \quad 1.30$$

This equation describes how the peak current i_p (A) increases linearly with the square root of the scan rate v (V/s), where n is the number of electrons transferred in the redox event, A (cm^2) is the electrode surface area (usually given as the geometric surface area), D (cm^2/s) is the diffusion coefficient of the oxidised analyte, and C (mol cm^{-3}) is the bulk concentration of the analyte.

1.1.5.2 *Square Wave Voltammetry (SWV)*

The square wave is characterised by a pulse height, ΔE_p, measured with respect to the corresponding tread of the staircase, and a pulse width t_p. Alternatively, the pulse width can be expressed in terms of the square wave frequency, $f = 1/2t_p$. The staircase shifts by ΔE_s at the beginning of each cycle; thus, the scan rate $v = \Delta E_s/2t_p = f\Delta E_s$. The scan begins at an initial potential, E_i, which can be applied for an arbitrary time to initialize the system as desired. Current samples are taken twice per cycle, at the end of each pulse. This is highlighted by the dots in the forward and reverse scans in Figure 1.7. The forward current sample, i_f, arises from the first pulse per cycle, which is in the direction of the

staircase scan. The reverse current sample, i_r, is taken at the end of the second pulse, which is in the opposite direction. A difference current Δi is calculated as i_f-i_r.[27] This technique gives excellent rejection of background currents.[28] Thus SWV yields peaks for faradaic processes, where the peak height is directly proportional to the concentration of the species in solution.[29]

SWV can be used to perform an experiment much faster than CV. SWV employs scan rates up to 1 V/s or faster, allowing much faster determinations. A typical experiment requiring three minutes by CV can be performed in a matter of seconds by SWV.[29]

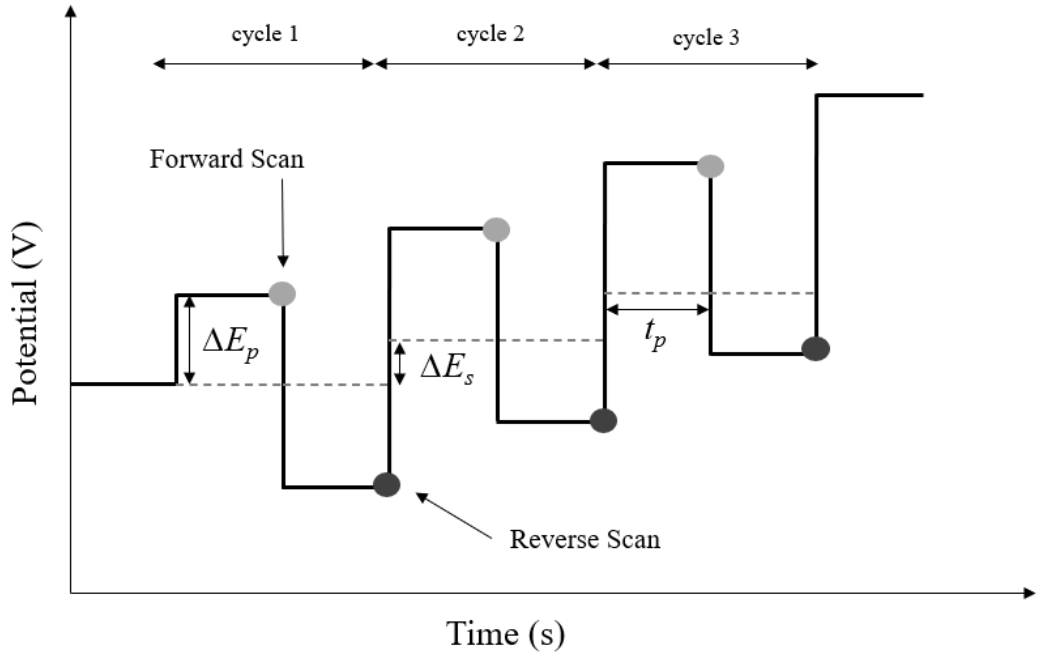


Figure 1.7 Schematic diagram of the potential in square wave voltammetry. Each cycle comprises a forward pulse and a reverse pulse, which are characterised by a pulse height (ΔE_p), a pulse increment (ΔE_s) and a pulse width (t_p).

1.1.5.3 *Chronoamperometry (CA)*

Chronoamperometry is a potential step technique. The resulting current from faradaic processes occurring at the electrode is monitored as a function of time. A stationary working electrode and unstirred solution are used. Mass transport under such condition is

solely by diffusion, therefore, the current-time curve reflects the change in the concentration gradient in the vicinity of the surface of the electrode. The slope of the concentration profile decreases as time progresses due to the depletion of the reactant associated with the gradual expansion of the diffusion layer. Subsequently, the current decays with time, as given by the Cottrell equation (eqn 1.29). In this work chronoamperometry is used for the constant potential deposition of metals on to the electrode surface.

1.1.5.4 *Stripping Voltammetry*

Stripping voltammetry is a trace analytical technique used in quantitative determination and speciation of metals and metal complexes. It is a two-step technique that involves a preconcentration step followed by a potential sweep that causes electrolytic dissolution or stripping of the species back into solution at characteristic potentials.[30, 31] The remarkable sensitivity of stripping voltammetry is attributable to the preconcentration that takes place during the deposition step.[31] The most common stripping voltammetry technique is anodic stripping voltammetry, this technique is used in the following work. ASV is primarily used for the analysis of metal ions and enables fast and accurate testing of water sample. Metal cations are reduced onto the electrode surface and subsequently oxidised by means of a potential sweep. Improved detection limits are possible in ASV by using potential step techniques instead of potential sweep. Potential step techniques take advantage of the fact that the capacitive component of the total current observed following a potential step decays more quickly (as t^{-1}) than does the faradaic component (as $t^{-1/2}$). Other stripping voltammetry techniques include potentiometric stripping analysis (PSV), cathodic stripping voltammetry (CSV), and adsorptive stripping voltammetry (AdSV).[30] ASV was chosen for CSV as this work focuses on the detection of lead which requires a negative deposition potential, CSV uses a positive deposition

potential and would be more appropriate for the detection of organic and inorganic compounds. AdSV forms a surface-active metal complex which is subsequently adsorbed and undergoes reduction at the electrode surface. AdSV is advantageous because it widens the scope of stripping voltammetry however it experiences limitations at higher concentrations due to adsorption sites at the electrode surface. PSV is an alternative to ASV where deposition occurs under potential-controlled conditions and the metal is subsequently stripped off by applying a controlled anodic current or by the addition of an oxidising agent. The resulting chronopotentiograms represent stripping plateaus. Qualitative analysis can be obtained from these plots using the Nernst equation and quantitative analysis can be obtained by differentiating the potential vs. time curve.

1.1.6 Electrochemistry at Microelectrodes

Microelectrodes are generally considered as those electrodes whose critical dimension (such as the radius of a disc or the width of a band) is comparable to, or smaller than the diffusion layer thickness, δ, and typically range from a few micrometres to 50 μm.[32] Under these conditions, a steady-state or a pseudo steady state is attained.[33] The International Union of Pure and Applied Chemistry (IUPAC) has defined that a microelectrode has dimensions of tens of micrometres or less, down to the submicrometre range, whereas other terms, for example ultramicroelectrodes and nanoelectrodes, are sometimes used in literature to describe electrode with dimensions of less than micrometre scale.[34] Ultramicroelectrodes are defined operationally as an electrode having a critical dimension smaller than 25 μm.[35] When the critical dimension of the electrode is below 10 nm, it is called a nanoelectrode.[35] The critical dimensions of the electrodes addressed in this work range between 1 μm to 20 μm, they are therefore considered ultramicroelectrodes. However, to maintain consistent terminology, it is preferable to

stick with the term "microelectrode" as it is now conventionally assumed that a microelectrode has dimensions of tens of micrometre or less, down to submicrometre range.

Decreasing the size of the electrode to the micron or submicron scale alters the voltammetric behaviour offering several advantageous properties over conventional macroelectrodes. Smaller electrodes lead to reduced ohmic resistance. Ohmic resistance relates to a drop in potential between the WE and RE as current is flowing through the electrochemical cell. The voltage drop can be influenced by the electrolyte conductivity, the distance between the WE and RE, and the magnitude of the current. Using Ohm's law, the ohmic (voltage) drop ΔE_{ohmic} can be calculated to be equal to the product of the current i and the ohmic or uncompensated resistance R_u:[36]

$$\Delta E_{ohmic} = iR_u \qquad 1.31$$

The behaviour of R_u is linked to the size of the electrode, as the electrode size decreases, so too does R_u, thus reducing the ohmic effects.[35] Other benefits of smaller electrode sizes include smaller capacitance, faster response times, better detection limits, lower sample volumes, and less power and materials to operate.[33, 34, 37-39] One of the most beneficial aspects of reducing electrode size is enhanced mass transport leading to steady-state behaviour. Larger electrodes are limited by mass transport unless slow scan rates are used. In contrast the enhanced mass transport at smaller electrodes means that steady state is observed at much faster scan rates, leading to overall faster analysis times. Since steady-state currents are not affected by scan rate but are dependent on the electrode geometry, as steady-state currents are achieved they can no longer be described by the Randles-

Sevcik equation. Different equations are used to describe behaviour and can be simply shown as:[35]

$$i_{ss} = nFAm_oC_o \quad 1.32$$

where m_o is a mass transfer coefficient. The functional form of m_o depends on the geometry, for example, band, cylinder, disk hemisphere and sphere.[35]

Although the advantages of microelectrodes are clearly apparent, one drawback of the use of single micro- and nanoelectrodes is the low current output; the measured currents are often in the nano to sub-nanoampere range. Consequently, the current measurement is sensitive to issues of electrical noise, often necessitating the use of a Faraday cage. This requirement for electrical shielding can negatively impact their application in real world sensing. A way to address this limitation is the use of arrays of microelectrodes, whereby multiple microelectrodes are operated in parallel. The microelectrode array leads to an increase of the electrochemical signal in proportion to the number of active electrodes in the array. Therefore, a considerable improvement in the current magnitude and enhanced signal-to-noise ratio are achieved.[32] Further improvements that can be made to overcome these issues of weak currents is through optimisation of micro- or nanoelectrodes band geometry. A larger current output can be produced by simply increasing the length of the band. These bands can also be used in an array to create devices with a higher total current output that are also less susceptible to interference.[34] However, further considerations of electrode design need to be taken into account when using microelectrode arrays. When designed correctly, an array of microelectrodes wired in parallel can offer the same enhanced sensitivity of a single microelectrode but with the advantage of a higher total current. A challenge with optimising microband design is to pack the bands closely

without losing their diffusional independence. Diffusional independence is the term used to describe the effect when the diffusion layers of the reacting electrodes do not overlap, see Figure 1.8(i). Any significant overlap of the diffusion fields between adjacent bands creates competition between those bands for the diffusing species, see Figure 1.8(ii).[40] This has a "shielding effect" which decreases the flux density at each individual band, reducing the total current measured to a fraction of what is expected, and negating the advantages of using microelectrodes. The shielding effect is described by:[41]

$$SF = 1 - \frac{i_{sh}}{\sum_{j=1}^{n} i_j} \qquad 1.33$$

The extent of diffusion overlap depends on the relationship of the relative sizes of the diffusion layer, the microband width and the band separation. The length of the microband has no effect on the nature of the diffusion, since it is orders of magnitude greater than the diffusion layer thickness.[42] Ensuring that there is adequate space between each electrode can prevent this diffusional overlap, but also increases the overall array footprint. Another attractive quality of band electrode geometries is the ease at which they can be fabricated as interdigitated electrodes (IDE). IDEs typically used as Generator-Collector electrodes can eliminate diffusion layer overlap when electrodes in the array are placed close to each other, thereby reducing the array footprint.

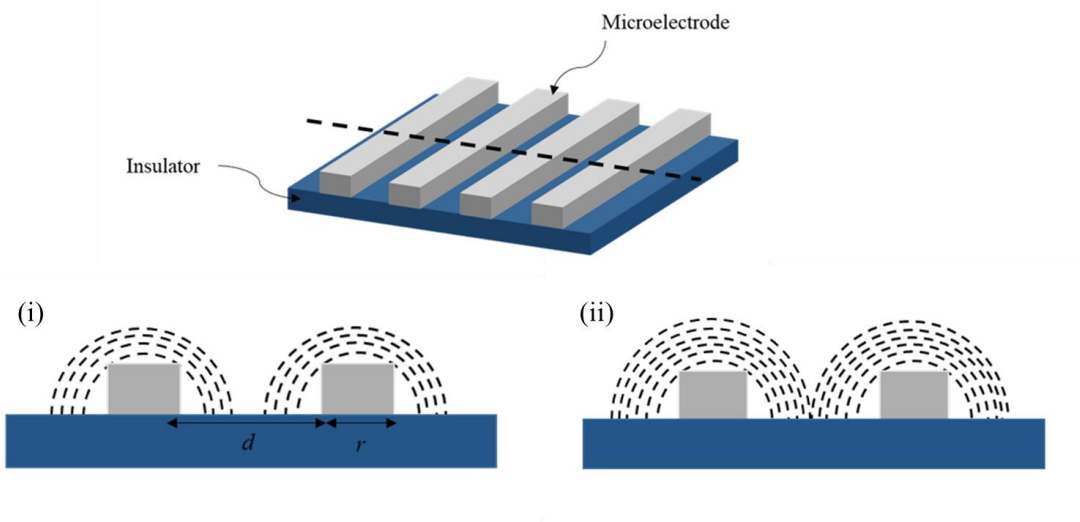


Figure 1.8 Schematic diagram of the diffusion layers where (i) the electrodes are diffusionally independent and (ii) the diffusion layers are diffusionally dependent.

Generator-collector devices consist of consecutive bands in an array which alternate between anodic and cathodic potentials. The target analyte is electrochemically titrated by measuring its diffusion from the "generator" band to the "collector" band, hence the name Generator-Collector (GC).[42] A simpler explanation is that the generator electrode is used to oxidise or reduce the analyte and the collector electrode is held at a potential which converts the analyte back to its starting form (redox cycling) or to another species.[43] In 1986 Bard *et al*. demonstrated reversible cycling of redox species between the two photolithographically patterned microelectrodes, the generator and collector electrodes, which lead to a greatly amplified current. Several applications of GC devices have been reported since.[44] An important parameter to consider when using GC electrodes is the collection efficiency, *N*, which is defined as the ratio of the current at the collector electrode I_{col}, to the current at the generator electrode, I_{gen}:

$$N = -\frac{I_{col}}{I_{gen}} \qquad 1.34$$

Ideally, the value of *N* should be as high as possible to ensure the best accuracy of results and greater sensitivity. Decreasing the width of the electrodes and inter-electrode gap increases *N*, thus decreasing overall sensor footprint. This is evident by work carried out by Niwa et al.[45], who proved that reducing the electrode with and inter-electrode gap lead to an increase in collection efficiency. In cases of redox cycling where the redox species is cycled between the generator and collector electrodes multiple times, an increase in current is measured. The more cycles that a molecule undergoes, the higher the measurable current which results in enhanced sensitivity. The number of redox cycles is determined by the collection efficiency and can be estimated by the equation:[45]

$$R_c = \frac{1}{1 - \Phi_1 \Phi_2} \qquad 1.35$$

The values Φ_1 and Φ_2 are the collection efficiencies of each comb of the array. However, if the combs are identical (equal width, height, and length) then this simplifies to Φ^2.

The effect of the number of bands in IDE arrays being used as GC electrode was investigated by Min et al, who looked at arrays of 200, 400, and 600 bands for the analysis of the redox species ferro/ferrihexacyanide. It was found that the signal-to-noise ratio was a function of the width and gap and not the number of bands. It was also observed that at lower concentrations, a smaller number of electrode fingers was superior with respect to the signal-to-noise ratio. At higher concentrations (50 to 100 µM) a medium number of bands, 400, was superior.[44]

1.2 Finite Element Simulations

Mass transport of redox analyte concentration profiles is an essential tool to study and predict mass transport behaviour at an electrode-solution interface under the application of an external potential. Diffusional mass transport from the bulk solution to an electrode surface consists of solving the partial differential equations relating the change in concentration with respect to time and position, as is mathematically described by Fick's second law of diffusion.[46, 47] At single electrodes, mass transport simulations are principally used to provide important insight on analyte concentration profiles in conjunction with experimental results. Simulations of electrode arrays can be useful in optimising electrode design prior to fabrication. The diffusion profiles at single electrodes and electrode arrays can be represented by the diffusion domain approach. The partial differential equations can be solved either by hand or by a relevant computer model using a numerical technique known as the finite element method. COMSOL Multiphysics® is a well-used versatile commercial software package for the solution of partial differential equations. An overview of COMSOL Multiphysics® is given here, in addition to mass transport at electrode, the diffusion domain approach and the finite element method.

1.2.1 COMSOL Multiphysics®

An overview of the steps to set-up and run a model are shown in Figure 1.9. The first step in building the model is to determine the space dimension. For this work a 2D space dimension is used. The 'Physics' is selected from a pre-set built-in list on the software. In this case, 'Transport of Diluted Species' is selected under the 'Chemical Species Transport' section. The specific study selected is 'Time Dependent'. Finally, the model is built and ready for defining and processing.

The parameters, variables and functions are defined under Global Definitions. These are applied to the entire file. Under 'Component' section, the parameters, variables and functions are specified to systems specific to the model. Other sections under Component include Geometry, Materials, Transport of Diluted Species and Mesh. These are used to draw domain, specify materials, apply the physics with built-differential equations and assign boundary conditions. The solver parameters can be adjusted under Study and the simulation is computed here. The resulting simulations can be processed in the results section.

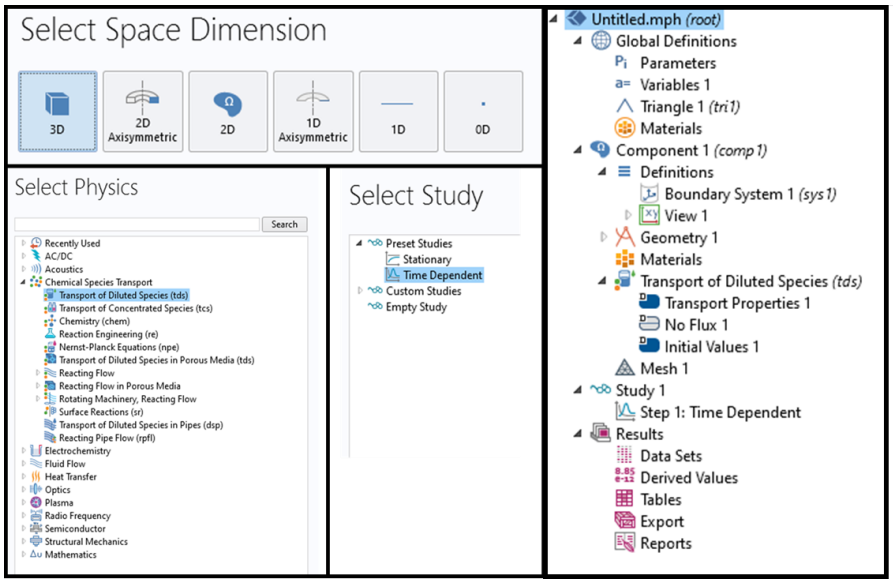


Figure 1.9 Screenshots of steps for building, solving and processing a model in COMSOL Multiphysics® 5.2.

The Transport of Diluted Species modelling platform allows the study of analyte concentration profiles for the oxidation of a redox molecule at a single electrode or electrode array. These simulations were based on the single electron oxidation process of a standard redox probe ferrocene monocarboxylic acid (FCA) in solution at the surface of the electrode of interest. This reaction can be represented by the oxidation/reduction electron transfer reaction, see equation 1.4. The simulations undertaken were used to assess the effect of electrode geometry on diffusional mass transport of FCA during a

potential sweep technique, in this case cyclic voltammetry, with respect to applied scan rate, electrode spacing and electrode width. As electrochemical experiments were undertaken in the presence of excess supporting electrolyte, in static un-agitated environments, at constant temperature and over short time periods, mass transport effects arising from migration and convection were assumed to be negligible. As a result, emphasis was placed on diffusional mass transport alone, and only Fick's second law of diffusion with respect to band electrodes in 2D was considered[46, 47]:

$$\frac{\partial C_i}{\partial_t} = D_i \frac{\partial^2 C_i}{\partial x^2} + \frac{\partial^2 C_i}{\partial z^2}$$

1.36

where *Ci* and *Di* represent the concentration and diffusion coefficient of the redox species in solution, respectively. Assuming a simple reversible charge transfer process, where both *O* and *R* are present in solution, the relative diffusion coefficients may have slight variances but for simulation purposes they were assumed to have equal values, i.e., ($D_O = D_R$). The concentration of *R* at an electrode of interest for a given time interval using a potential sweep method may be expressed by the following Nernstian boundary conditions[47, 48]:

$$\text{at t = 0: } C_R(t) = C_R^*$$

1.37

$$\text{at t > 0 = } C_R(t) = \frac{C_R^*}{1+\exp\left[\frac{nF}{RT}(E^0 - E(t))\right]}$$

1.38

where *t* is time (s), C_R^* and $C_R(t)$ concentration (mol m^{-3}) of the reductant species R in the bulk and at the electrode surface with respect to time, respectively, *n* is the number of electrons exchanged, *F* is Faraday's constant, *R* is the gas constant, *T* is temperature (K),

E^0 is the formal potential of the redox couple (V). E(t) is the applied forward potential in V defined as:

$$E(t) = E_{int} + vt \quad 1.39$$

where E_{int} is the initial voltage (V) of the potential sweep, v is the scan rate ($V.s^{-1}$), t is the time (s).

1.2.2 Mass Transport at Microelectrodes

In a cyclic voltammetric study of Ferrocene Carboxylic Acid, the redox reaction is driven by the applied potential. The change in potential causes the Fe^{2+} in FCA to be oxidised to Fe^{3+} at the electrode surface. During the reaction, as the electroactive Fe^{2+} is depleted a concentration gradient is formed. Convection and migration effects are considered negligible such that the thickness of the depletion zone is limited by the rate of diffusion only. The voltammetric result of the reaction is highly dependent on the size of the diffusion layer thickness, δ, versus the electrodes critical dimensions, r. In cases where the diffusion layer is small compared to the electrode critical dimension ($\delta < r$), resulting in a diffusion-limited and time-dependent response, i.e., planar diffusion. Alternatively, in cases where the diffusion layer is large compared to the electrode critical dimension ($\delta > r$), a steady-state and time-independent response is achieved, i.e., radial diffusion. As a result, planar diffusion is likely to occur at larger electrodes and radial diffusion is typical at smaller electrodes. In both cases, as well as cases where a transition from diffusion to planar are observed, there is a dependence on the analysis time scale. The shorter the time scale, the smaller the growth of the diffusion layer, especially for larger electrodes, and thus the more likely planar diffusion dominates. Longer time scales allow for sufficient growth of the diffusion layer for radial diffusion to be achieved. It is important to note

here that the steady state rate of diffusion at a microelectrode is much higher than that for a macroelectrode, therefore, steady state response can be obtained for microelectrodes at a shorter time scale.

For electrode arrays, mass transport becomes more complicated as the inter-electrode distance and interaction between electrodes need to be taken into consideration. Hence, the inter-electrode distance is a critical factor that needs to be incorporated into the electrode array design. Simulations are key here for optimising the electrode array design prior to fabrication. Compton et. al. have pointed out four main regimes affecting diffusional mass transport to microelectrode arrays, as highlighted in Figure 1.10.[40, 42, 49] These regimes are described by the relationship between the thickness of individual electrode diffusion layer, δ, the electrode critical dimension, r, and the inter-electrode distance, d. The four regimes are as follows: (i) planar diffusion to each electrode as $\delta \ll r$, radial diffusion to each electrode as $\delta = r < d$, (iii) a transitional zone where $r < \delta \leq d$, and (iv) planar diffusion to the electrodes when $\delta \gg d$. In regime (i), the electrodes are well separated but due to short analysis times the diffusion layers are small compared to the critical dimension, this results in planar diffusion and a tailing off of the current. Regime (ii) is optimum as is reflective of an array design where the electrodes are well spaced and sufficient analysis time has been given for the formation of the diffusion layers. In this regime, the current response of the whole array is equivalent to a single electrode, time the number of electrodes in the array. Regimes (iii) and (iv) are examples of designs where the inter-electrode distance is too small resulting in partial or complete overlap of the individual diffusion layers, respectively. The measured current from these regimes is becomes lower and tends to tail off, giving rise to peak-shaped responses. The reduction is signal is due to the electrode array behaving as a one large electrode equal to

the total area of the array (electrodes and insulating area between them) rather than individual microelectrodes.

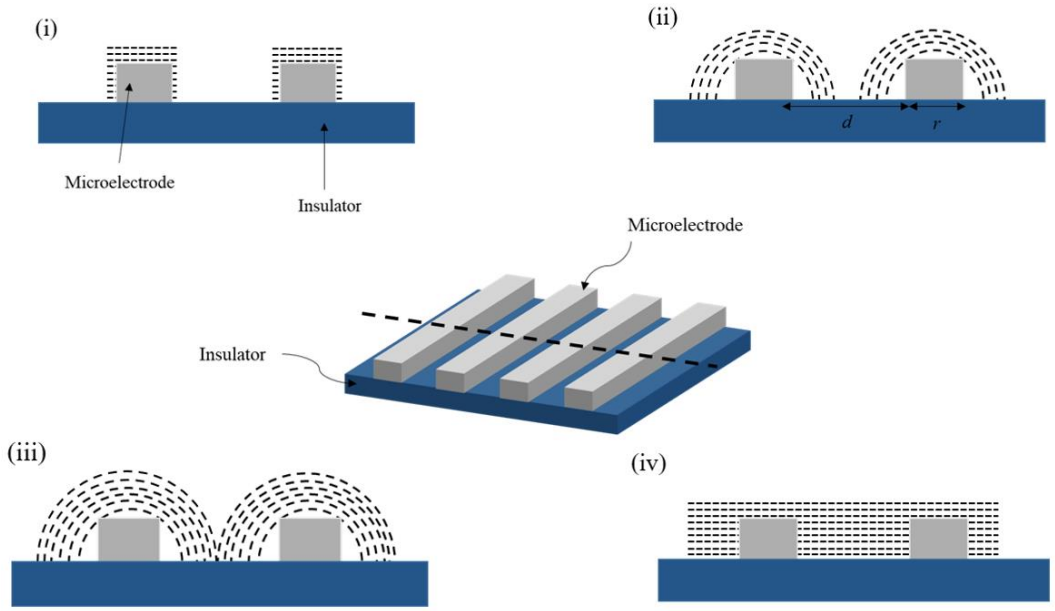


Figure 1.10 Schematic diagram of the four categories a diffusion profile may belong to for an array of microelectrodes. (i) $\delta \ll r$, planar diffusion to each electrode, (ii) $\delta = r < d$, radial diffusion to each electrode, (iii) $r < \delta \leq d$, transition zone and (iv) $\delta \gg d$, planar diffusion to the entire array.

1.2.3 Diffusion Domain Approach

The simulation of mass transport at electrodes is a 3D phenomenon, which is time consuming and complicated to solve. The diffusion domain approach simplifies simulation of a 3D problem into a 2D problem without losing accuracy by identifying the presence of a diffusionally independent unit cell. The unit cell of the diffusion domain approach is represented by an x,z plane of symmetry present at the centre of each microband and at the mid-point between two neighbouring microbands, across which the net diffusional flux must be equal to zero. Hence, each unit is diffusionally independent. Diffusion need only be simulated at a single diffusion domain between these planes of symmetry. This means that to simulate the CV response of a particular array, only the response of one square needs to be simulated and this can then be multiplied by the

number of electrodes in the array. [42, 46, 50] A visual representation of the 2D unit cell used for the diffusions domain approach can be seen in Figure 1.11.

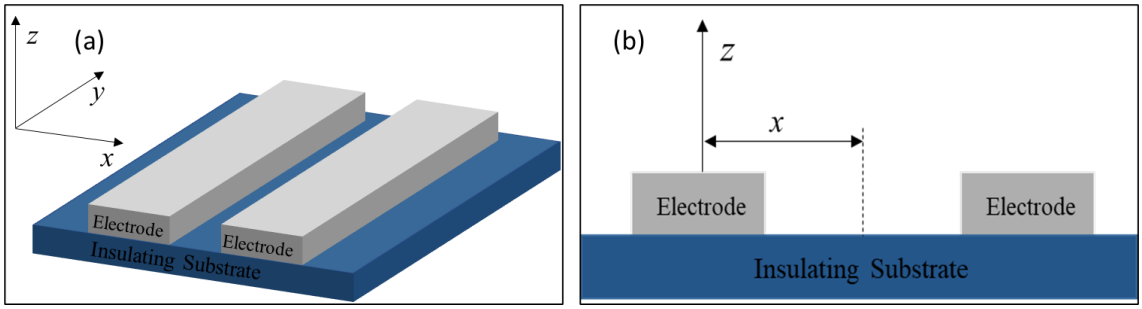


Figure 1.11 Schematic representation of (a) a 3D microelectrode domain and (b) a 2D cross section through the x,z plane, representing one unit cell for the diffusion domain approach

1.2.4 Finite Element Method

The finite element method is a numerical method for solving partial differential equations. The basic concept can be thought of as splitting the computational domain into individual smaller sub-domains, called finite elements. The centre of such elements is known as a node and put together they form a mesh. Partial differential equations solutions are computed at the node; solutions are interpolated, i.e., estimated using basis functions, whereby any point is described according to the number of parameters of the system that may vary independently (finite elements or degrees of freedom). The finite elements geometry depends on that of the domain. Generally, in 1D representations the finite elements are lines; in a 2D situation they are triangles and in 3D they are tetrahedrons.[51, 52] In Figure 1.12, a schematic representation of a typical triangular mesh used in a 2D problem representation is shown.

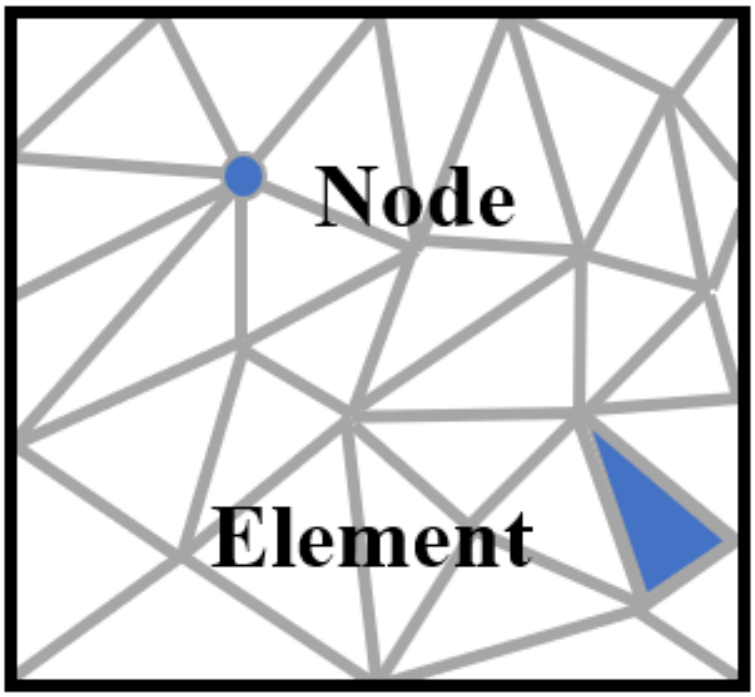


Figure 1.12 Schematic representation of a typical triangular mesh used in a 2D domain.

1.3 Detection of Lead in Water

Lead is a toxic metal whose widespread use has caused extensive environmental contamination and health problems in many parts of the world. Exposure to lead causes a significant burden of disease; the Institute for Health Metrics and Evaluation has estimated that in 2017, lead exposure accounted for 1.06 million deaths and 24.4 million disability-adjusted life years (DALYs) due to long-term effects of lead.[53] Lead is a cumulative toxicant that affects multiple body systems, including neurological, haematological, gastrointestinal, cardiovascular and renal systems. Even very low levels of lead exposure can cause these adverse health effects and developmental disorders, which introduce particularly serious problems in children including slowed motor responses, decreased IQs and hypertension.[54] Lead exposure is estimated to contribute to about 600,000 new cases of intellectual disabilities in children every year.[55] Additionally, penetration of lead through the Blood Brain Barrier (BBB) is proving to be a risk factor for Alzheimer's disease and Senile Dementia.[56]

Lead is not biodegradable, therefore, when discharged from lead related activities such as mining or from lead containing products (paint, pipes batteries or gasoline), it can accumulate in the environment, which results in contaminated food and water.[57] 300 million tonnes of lead mined to date is still circulating mostly in soil and groundwater.[58] It has been reported that the contamination of drinking and daily use water sources with lead has increased over the years due to issues such as the corrosion of metal solders and joints that connect the pipes in the water distribution system. The leaching rate of dissolution of metals in the channel depends on other factors such as pH, temperature, the presence of chloride ions, dissolved oxygen and water softness.[59]

The World Health Organisation (WHO) and Environmental Protection Agency (EPA) have strictly defined concentration limits for lead that is allowed in drinking water. As of

2013, the WHO reduced this limit from 50 ppb to 10 ppb to reduce exposure to lead to the lowest possible limit. However some drinking water may not meet this level.[60] In Ireland for example, a recent document released by Irish Water showed 23 supplies across Ireland were found to have been above the permitted level.[61] This figure is only taking into account water sources tested by Irish Water who are only responsible for the water supply outside a household's property. Water flowing through the pipes on private property is no longer the responsibility of Irish Water and no longer tested, therefore the water coming out of the tap could possibly have an even higher lead content depending on the pipes. This highlights the drastic need for the availability of easily accessible sensors for the detection of lead in drinking water.

1.3.1 A review of Sensors Used for the Detection of Lead in Tap Water

At present, the laboratory standards for the detection of lead in drinking water are atomic absorption spectroscopy (AAS) and inductively coupled plasma – mass spectroscopy (ICP-MS). While there are advantages to these techniques such as their sensitivity and low limit of detection (LOD) in the femtomolar range[62]; there are also many disadvantages. These include expensive equipment, requirement for qualified operators, and complex analytical procedures, which make these techniques unsuitable for on-site and on time measurements. The stability of water samples during long-term storage is questionable, as they are subject to various biological, chemical, and physical effects.[62-65]

An electrochemical approach to the detection of lead in water samples offers an attractive alternative to spectroscopic techniques due to the numerous advantages associated with it. Compared to spectroscopic techniques, electrochemical devices are much more user-friendly as they require simple operating procedures. These devices are also lower cost

than the equipment needed for spectroscopic techniques due to their smaller size and lower power requirements. They also give faster analysis times, out of the literature reviewed, 70% of the sensors had analysis times of 5 minutes or less. Opting for electrochemical techniques also gives rise to the opportunity to mass produce sensors which allows for multiple devices to be produced at the same cost. These advantages make electrochemical devices much more attractive on-site and on time measurements.[63] The sensing mechanism of electrochemical devices is based on output-transducer signals wherein the potential difference is measured using a potentiostat. Recent advancements in potentiostat design have made it possible for small, compact devices for handheld portable sensing devices.[66] Anodic stripping voltammetry (ASV) is one of the most commonly employed electrochemical methods for the detection of lead.[67] This involves electrodeposition (reduction) of target metals from solution onto/into the working electrode of an electrochemical device and subsequent stripping (oxidation) of the analyte from the working electrode surface at a specific potential, as depicted in Figure 1.13. This electrochemical process is fast; with the deposition step happening in a matter of minutes (typically 2- 5 mins) and the stripping step needing seconds to complete. This process leads to the production of a current that is proportional to the concentration of lead in the water sample. The stripping techniques used in this work is SWV. The peak current for this technique is given as follows:[9]

$$\Delta i_p = \frac{nFAD_o^{\frac{1}{2}}C_o^*}{\pi^{\frac{1}{2}}t_p^{\frac{1}{2}}}\Delta_\psi$$

1.40

where n is the number of electrons, F is Faraday's Constant (96,485 C mol-1), A is the electrode area (cm2), D_0 is the diffusion coefficient of the species, C_0 is the concentration of the species, t_p is the experimental timescale $\frac{1}{2T_{sw,p}} - T_{sw,w}$, and Δ_ψ is a dimensionless

peak current parameter. Metal deposition and dissolution or stripping processes at electrodes can be simply represented by the equation:

$$M^{n+} + ne^- \rightleftharpoons M \quad 1.41$$

ASV can be used with linear scans or modulations (differential pulse ASV (DPASV) and square wave ASV (SWASV)) and exhibits higher sensitivity with low LOD (~0.002 ppb to 200 ppb in comparison to linear sweep voltammetry (LSV).[63] The characteristic redox potential of lead allows their sensing by untreated metal electrodes and consequently eliminates the demand of a molecular recognition probe that is used in optical sensors. The specificity of this method arises as the oxidation of lead requires a specific potential.

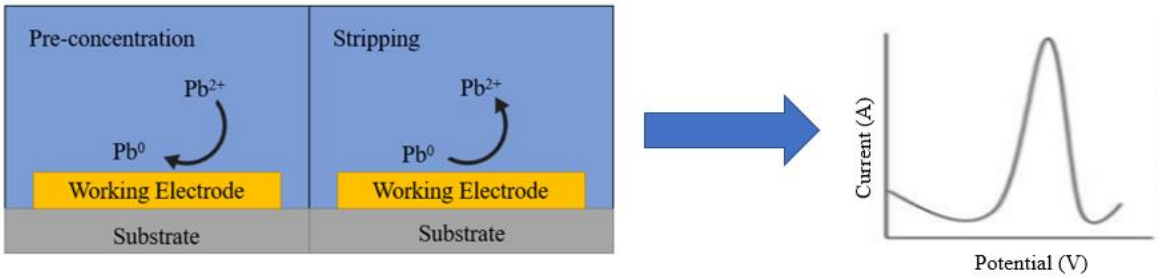


Figure 1.13 Anodic stripping voltammetry (ASV) principle.

At solid metal electrodes, the electrodeposition of metals proceeds via formation of a monolayer of the target metal (underpotential deposition, UPD) followed by the deposition of the bulk-phase metal. UPD can be defined as 'the electrochemical adsorption of a sub-monolayer or monolayer of cations on a foreign metal substrate at potentials more positive than the reversible potential of the deposited metal'.[68] The equilibrium at which the deposition and stripping of the bulk-metal phase occurs is given by the Nernst Equation:[69]

$$E_{eq} = E^0 + \frac{RT}{nF} ln \frac{a^{M^{n+}}}{a^M}$$

1.42

where E_{eq} is the equilibrium potential (V), E_0 is the standard potential (V), a is the activity, n is the number of electrons involved in the reaction, T is the temperature (K), R the gas constant (J mol^{-1} K^{-1}) and F is Faraday's constant (C mol^{-1}). Cyclic voltammetry studies carried out by Herzog and Arrigan,[69] showed that a peak occurs at a potential more positive than the Nernst potential. This relates to the formation of a monolayer or sub-monolayer of metal atoms on the electrode surface. Subsequently, the bulk-metal deposition occurs at a potential close to the Nernst potential. On the reverse scan, the bulk deposit is stripped first from the electrode and at a more positive potential, the last of the monolayer or sub-monolayer metal, the UPD, is stripped back into solution. UPD of metals occurs at solid electrodes due to stronger interactions of the deposited atoms with the substrate than with each other. Therefore, less energy is required to reduce the first monolayer of metal, through strong attraction between that metal and the substrate electrode material. As a result, potentials of UPD occur before the thermodynamically predicted potential for the metal deposition. This can be viewed as an adsorption process in which the Gibbs energy of the adsorbate-substrate interaction is greater than that for the adsorbate-adsorbate interaction. The advantage of using UPD-ASV over bulk-metal deposition is that the metallic deposit covers a very low portion of the working electrode surface. Therefore, the structure of the electrode remains mainly unchanged, resulting in good repeatability of the analytical response. Additionally, this helps avoid the need for mechanical and electrochemical treatment between measurements.

This review describes recent progress in the design and development of electrochemical sensors used for the detection of lead in water samples. An in-depth study was conducted into will the design, fabrication, and application of these sensors to real water samples

with an emphasis on their potential applicability as portable handheld devices or unobtrusive deployable devices for the detection of lead in drinking water.

1.3.1.1 *Materials*

A review by Arduini *et al*. conducted in 2010 found that bismuth made up 37% of the materials used for lead detection, not just in water quality monitoring but in all-natural samples (food, clinical and environmental). The other materials were as follows; mercury 20%, chemical modification 13%, different types of carbon 11%, boron-doped 7%, gold 6% and silver and antimony both 3%.[70] Looking specifically at sensors for water monitoring, there is a similar trend to that found by Arduini with the majority of research in this area has been carried out on bismuth sensors, as can be seen in Figure 1.14. Bismuth electrodes have been in use since 1930,[70] however, it was not until 2000 when the use of bismuth electrodes as an attractive alternative for mercury was first reported by Wang et al.[71] Bismuth was regarded as the ideal materials to replace mercury in lead sensors as it was considered to be environmentally friendly, have low toxicity and it can form multicomponent "fused alloy" with many metals. [70, 72, 73]

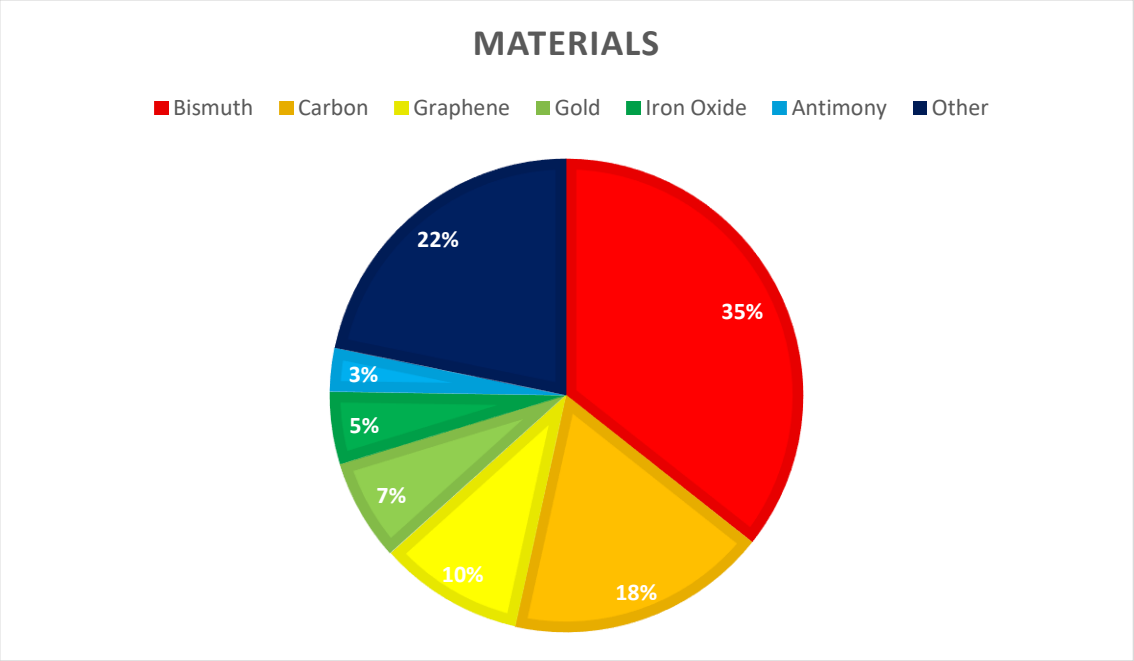


Figure 1.14 Distribution of sensing materials used in lead sensors for water quality monitoring.

There are two methods for using bismuth as a sensing material, the first is the simultaneous deposition of bismuth and analyte is known as *in situ* plating. The alternative technique is *ex situ* plating, which involves electrodepositing the bismuth-film ions before transferring the electrode to the sample solution for analysis.[73] While *in situ* is generally considered superior to *ex situ* plating due to simplification and shortening of the experimental procedure, it is disadvantageous for use in a commercial portable sensor. The use of in *situ* bismuth plating in a commercial sensor would require additional buffers and sample preparation, and the associated technical training. *Ex situ* plating is better suited to the mass production of commercial sensors. However, issues arise with *ex situ* deposited bismuth films due to oxidation, degradation, or detachment of the film surface with use. This affects the overall performance including sensitivity, reliability, reproducibility, and sensor lifetime.[74-77] The principles of *in situ* and *ex situ* bismuth plating are outlined in Figure 1.15.

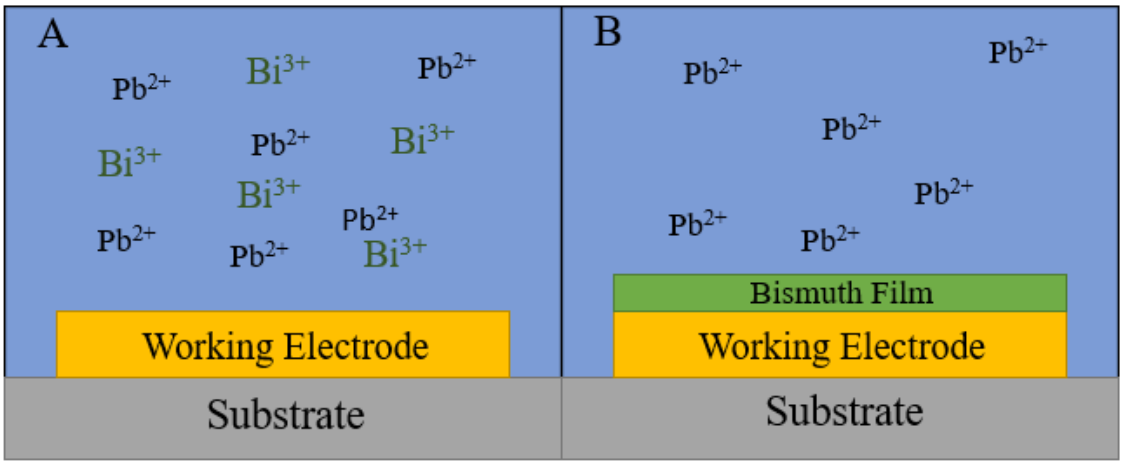


Figure 1.15 Principles of (A) In situ and (B) Ex situ bismuth electrodes for the detection of lead in water

Despite this, interest in bismuth as a sensing material for lead in water has been maintained throughout the years. In the last ten years carbon and other materials, such as polymers, metal-organic framework and various nanoparticles have been increasing in popularity and only in the last five years has research in graphene and iron oxides started

emerging. These electrodes are more frequently being used as a replacement for bismuth electrodes as they overcome the issues mentioned above.

1.3.1.2 *Fabrication*

For sensors to be commercially viable in portable or *in situ* detection units, the fabrication process needs to be low-cost, time-efficient, and capable of mass production. Fabrication techniques used in the sensors outlined in this review include photolithography techniques such as screen-printing and microfabricated, or modified electrodes. The latter will be covered in following section.

Screen-printing electrodes (SPEs) is the second most popular fabrication technique used by the sensors reviewed here, after modifying commercial glassy carbon electrodes. The popularity of SPEs is due to the fact this technique enables the rapid fabrication of inexpensive electrodes. [78] SPEs allow for the ability to cheaply manufacture the working, reference, and counter electrodes on the chip at the same time, as opposed to other fabrication strategies seen in this review. These chips can be connected to miniaturised potentiostats which makes this a very attractive technique for the development of hand-held or small deployable devices. [79] Due to the inexpensive nature of SPEs they are quite often used as disposable electrode.[78, 80] Lithographically fabricated electrodes, particularly microfabricated electrodes, proved to be a not so popular technique among the sensors analysed for this review. There are many advantages to the microfabrication technique such as reduced sensor size, volume and cost along with the ability to mass produce geometrically identical, uniform and well-defined surface structures, and similar to SPEs, integrated reference and counter electrodes.[81, 82] Not only do microfabricated electrodes require less space and power, they offer many other benefits such as reduced resistance (ohmic drop), reduced sample consumption, higher current densities due to enhanced mass transport and increased ability to facilitate measurements in low-ionic-

strength water samples; these characteristics result in greater sensitivity, improved response and increased signal-to-noise ratio.[32, 34, 37] The main draw-back of microelectrodes is the low current output; the measured current are often in the nano to subnanoampere range. Therefore microfabricated electrodes can be disadvantageous as low current output limits the typical detection of microfabricated electrodes to 1 – 2 ppb, making them insufficient for the detection of trace metals with less than 1 ppb concentration.[83]

There are two ways in which the limitations of microfabricated electrodes can be overcome. The first is longer deposition times of 300 – 500 seconds to get better signal-to-noise ratio and lower detection limits.[32] The advantages of microfabrication such as reduced sensor size, volume and cost along with the ability to mass produce geometrically identical, uniform and well-defined surface structures with integrated reference and counter electrodes should substantially outweigh the need to for an extra few minutes deposition time.[81, 82] The second method is through the use of microfabricated electrode arrays or microelectrode arrays. The microelectrode array leads to an increase of the electrochemical signal in proportion to the number of active electrodes in the array. Therefore, a considerable improvement in the current magnitude and signal-to-noise ratio can be achieved.[32] Improved behaviour as a result of microelectrode arrays has been illustrated by Kanyong et al., see Figure 1.16. Here, gold nanoparticles were electrodeposited on screen-printed carbon electrodes (SPCE). These electrodes achieved a limit of detection of 2.1 ppt, lower than most of the other screen-printed sensors. The difference between this work and other AuNP on carbon screen-printed electrodes is that the electrodes were printed in a microelectrode array configuration (working area: 5.03×10^{-5} μm^2).[80] However, the disposable nature of these sensors make them unsuitable for implementation in portable or in-line monitoring devices.

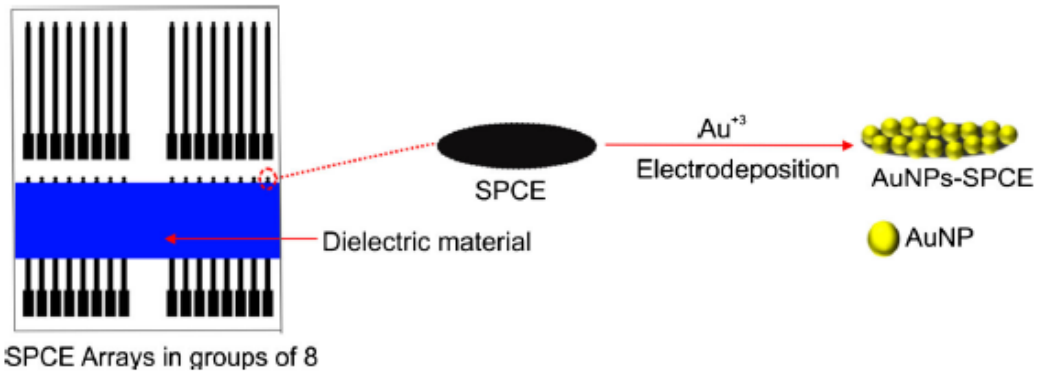


Figure 1.16 Screen-printing of carbon arrays and gold nanoparticle (AuNP) modification.[80]

1.3.1.3 *Modifications*

As highlighted in 1.3.1.2, for microfabricated electrodes to be efficient at detecting low concentrations of analyte, modification may be necessary. Many of the sensors looked at for this review relied on the modification of commercial glassy carbon electrodes for the detection of lead in water. [84-119] This is an inefficient fabrication process for the mass production of sensors on a commercial scale for two main reasons. Firstly, the glassy carbon electrodes used were large and bulky and incompatible with portable or small deployable devices. Secondly, many of the modification processes are not low-cost or time-efficient, an example being, the hollow sphere bismuth oxide doped mesoporous carbon nanocomposites.[120] The modification of the glassy carbon electrode with the nanocomposite was quite straightforward, requiring simply the nanocomposite solution to be drop-cast and left dry for 1 hour in ambient conditions. The fabrication of these nanocomposites, however, is quite complex and time-consuming. It is made up of five steps, each of which require heating ranging from 90 °C to 500 °C. Two of these steps require heating for extended periods of time 10 – 12 hours and the final step requires stirring for 5 days. Not only is this process time-consuming, the amount of heating required will have high energy costs, making it an undesirable commercial process.

1.3.1.4 *Sensor Lifetime*

Sensor lifetime or stability is an important factor to consider in the development of commercial sensors. For a sensor to be worth buying by the consumer, it must have the longest possible lifetime. In terms of analysing the sensors outlined in this review, they can be broken into three categories: repeatability which looks at how many times measurements can be taken before there is a decrease in response, long-term stability which compares their response over a period of time or not subjected to examination. For those in the unexamined category, 31% of papers analysed for this review did not mention the repeatability or lifetime of the sensor. Repeatability measurements were undertaken by 52% and long-term stability was examined by only 17%.

For the repeatability measurements most sensors were only tested for 5, 10 or 15 measurements which does not give a convincing indication of the sensor lifetime nor is it enough measurements to get from a sensor for it to be a commercially viable product. A more desirable number of measurements of 30 – 60 was carried out by only 5 sensors sulphur-doped graphitic carbon nanoflakes on glassy carbon[121], zinc oxide nanofibers functionalised with L-cysteine on glassy carbon[110], nanoporous bismuth on screen-printed carbon[76], 2D bismuthine and graphene on glassy carbon[95], and bismuth on gold electrodes.[83] The most notable examination of repeatability was 120 measurements carried out on thiol-functionalised mesoporous silica and Nafion composites on glassy carbon electrodes, however, these measurements were carried out in 0.1 M HCl as the electrolyte and not in real water samples.[122] In order to assess the true repeatability of these sensors, assessment in real samples is required.

For the groups that looked at long-term stability of the sensors; half assessed up to 15 days or less while the other half assessed the stability over a 30 day period. Only one sensor was assessed for a longer period of 60 days, a ruthenium(II) textured graphene

oxide nanocomposite on a gold electrode. After the 60 days the sensor had retained 91.1% of the initial response[123]. However, like the repeatability study the long-term stability needs to be carried out in real samples to determine the true long-term stability of the sensor. Real water samples can contain surfactants and organic molecules that can impact the stability of the sensor surface.[122]

1.3.1.5 *Application in Real Samples*

Application to real water samples is a key element of any handheld or deployable device for lead sensing in water samples. In the literature examined for this review, all of the sensors had been tested in real water samples however, most required some pre-treatment before this was possible. Pre-treatment includes pH adjustment, filtration, and in cases where in situ bismuth films were used, bismuth ions were also added to the sample. 56% of the sensors looked at for this review required one or a combination of the pre-treatments mentioned. Only 5% specifically stated that no pre-treatment was required in real samples for testing and 39% gave no details as to the treatment of the real water samples.

In all cases none of the sensors were able to match the detection limits achieved in buffered solutions. Due to the high pH, organic carbon, and other species present in real water samples, lead ions may react and form insoluble lead compounds. For example, insoluble lead sulphate and lead carbonate will form in the presence of sulphate and carbonate ions in solution. Unfortunately, these neutral lead compounds cannot be detected by anodic stripping voltammetry, and most likely will decrease sensitivity of analysis.[124] Organic matter and other species present in real water samples can also cause biofouling of the electrode which can further impeded the ability to detect lead to same sensitivity as in buffered solutions.

1.3.1.6 *Summary of Literature Review Findings*

Bismuth has maintained popularity over the years as a sensing material for lead sensors in water despite the issues with reliability, reproducibility, and sensor lifetime. Focus needs to shift to other more durable materials to ensure commercial sensors developed are reliable and have as long a lifetime as possible. Many sensors reported in the literature were developed on commercially acquired glassy carbon electrodes with time-consuming and energy intensive processes for modification with the sensing material. An alternative approach such as lithographic fabrication, particularly microfabrication offers a better alternative then modifying glassy carbon electrodes for implementation in a commercial process. Further work is required on optimising sensors for real sample analysis. Many of the sensors reviewed here demonstrated excellent limits of detection in buffer solution, however, this is not the case when applied to real samples. The lead concentration in drinking water is generally low and the complexation of lead with other compounds in water means that sensors developed for this application need to have a lower limit of detection than what has previously been demonstrated in buffer solutions.

Based on these observations we propose microfabricated nanoporous gold-modified interdigitated arrays for the detection of lead in tap water. Microfabricating gold bands on silicon is a low-cost, time-efficient, and easily mass-produced process, ideal for commercial sensors. Nanoporous gold (NPG) was chosen for electrode surface modification for the detection of lead. NPG is a form of gold with a "sponge-like" 3D structure of interconnecting tuneable pores in a skeleton of gold filaments, which combine the conflicting properties of high porosity and strength.[125-127] It is formed via a two-step process involving electrochemical deposition of the silver-gold alloy on to the electrode surface, followed by subsequent etching or dealloying of the less noble silver metal.[128] The technique of dealloying has an ancient history, Incan civilisations dealloyed copper

from the surface of copper-gold alloys to create an illusion of a pure gold artefact known as depletion gilding.[126] Forty[129] showed that depletion gilding of a less-noble metal from Au alloys results in an open, continuous nanoporous gold structure. When the silver component in a silver-gold alloy is dissolved in nitric acid, the remaining gold atoms form a rough, porous material. The size of the pores can be easily tuned and range from a few nanometres to hundreds of nanometres.[130] This porous structure has been shown to be as strong as bulk gold despite being a highly porous material.[126, 131] The alloy deposition and silver etching times used in this work were 3 s and 2 mins., respectively, as established in previous work.[132, 133] NPG has a high specific surface area originating from its large internal surface area.[128, 130, 134] This attractive attribute, coupled with its superior catalytic properties[125] and excellent conductivity[135] make it a promising electrochemical sensing platform. Other advantages of using NPG as an electrochemical sensor include high selectivity, low overpotential, fast kinetics, longer device lifetimes and resistance to common impurities.[136, 137] The main benefit of using NPG over other surface modifications used for the detection of lead such as gold nanoparticles is that NPG is easier to prepare and is more stable. A significant drawback of nanoparticles materials is the requirement for expensive modifiers and lengthy modifications steps. Additionally, nanoparticles are prone to undergo aggregation, causing subsequent loss of available surface area and catalytic activity.[131, 138] NPG on the other hand is a low-cost-free-standing mesoporous thin film which can be easily mass-produced to create stable sensors.[139]

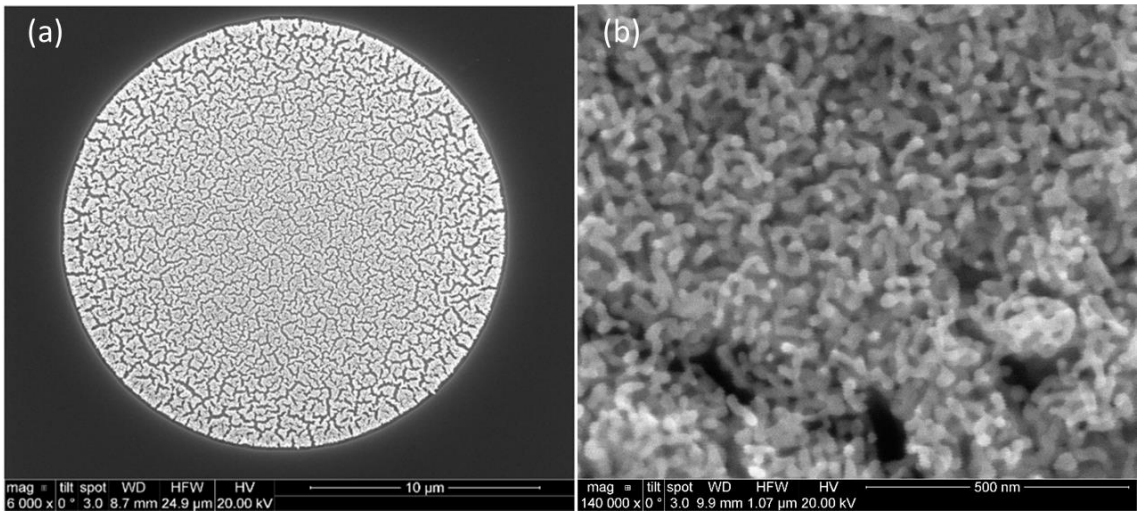


Figure 1.17 SEM Images of (a) NPG deposited at a 20 µm micro-disc electrode and (b) high mag of NPG deposited in 20 µm micro-disc electrodes

An issue for many of the sensors looked at for this review was detection of lead in real samples. While many established successful detections of lead in buffered solutions, they failed to detect lead in water samples collected at source without any pre-treatment. The primary issue with real samples is the increased pH compared to buffer solutions. The pH of water is typically in the range of 6 – 8 pH, where many of the buffered solutions used ranged between 3 - 5 pH. Our solution to overcome this is using IDE arrays. IDE arrays are typically used for solution based redox active species, which differs from the case where lead is preconcentrated at the sensor electrode. However, IDE arrays can also be used for electrochemical or *in situ* pH control.[140-142] Prior work by Macpherson et al.[143] showed successful detection of mercury using *in situ* pH control in water using a ring disc electrode arrangement. The protons created during hydrolysis of water at the anode ring diffused to the sensing electrode disc electrode lowering the local pH of the electrodes compared to the bulk, enabling direct detection of mercury. At IDE arrays, *in situ* pH control is achieved by imposing an appropriate potential at one comb of electrodes, termed as the protonator, which induces a local pH change which differs from that of the bulk solution but enables detection at the other comb of electrodes, the sensing electrodes.

Acidic conditions are achieved when the protonator electrodes are held at a sufficiently high oxidising potentials leading to the formation of H^+ ion, as shown in equation 1.43.[144]

$$2H_2O \rightarrow O_2 + 4H^+ + 4e^-$$

1.43

A visual representation of in situ pH control can be seen in Figure 1.18. Here, the central protonator electrode has been held at a sufficiently high potential to induce a local pH change to pH 3 at the sensing electrodes in a bulk solution of pH 7.

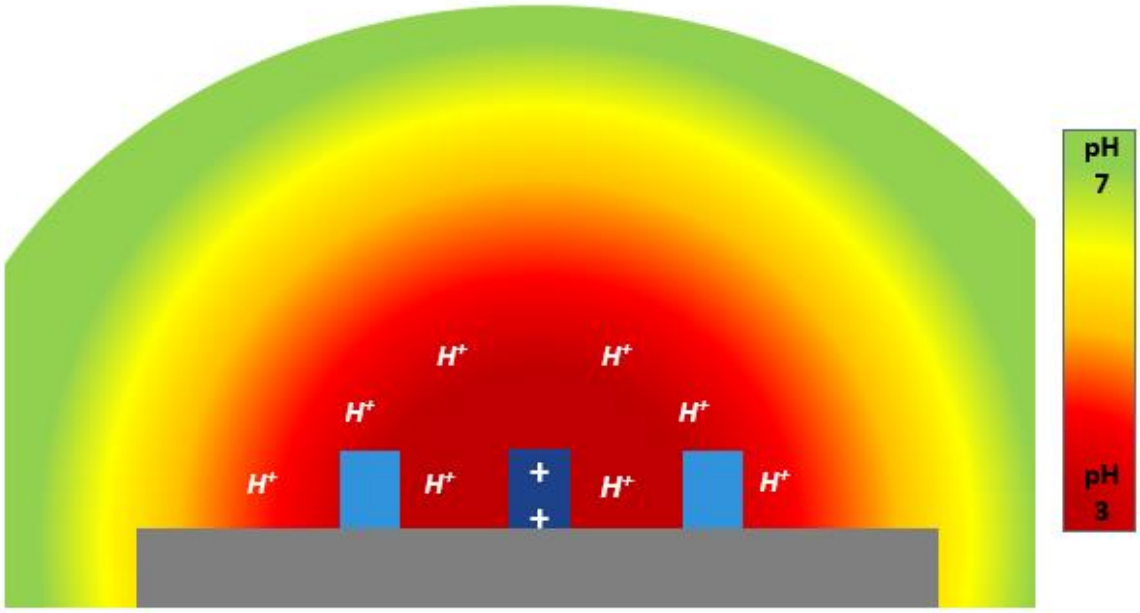


Figure 1.18 Schematic of in situ pH control at IDE array where the central protonator electrode has induced a local pH change at the array of pH 3. The protonator was held at 1.65 V while the sensing electrodes were swept from 1.2 V to 0 V at 50 mV s^{-1}. The electrode bands were 1 µm wide with a 2 µm inter-electrode gap.

1.4 Conclusions

This chapter highlighted the electrochemical fundamentals and techniques used for the work carried out in this thesis. A brief description introduction to COMSOL Multiphysics® was given along with an account of the benefits of microelectrodes, generator-collector electrodes and mass transport at such electrodes. The chapter concludes with a review of electrochemical sensors for the detection of lead in tap water. The use of stripping analysis at electrochemical sensors has been gathering momentum for many years, in a review in 1999, Wang *et al.* reported the expectation that stripping analysis would rapidly rise in popularity in the 21st century and have a major impact on decentralised metal testing. While there has been much work carried out in developing sensors for stripping analysis since then, none have yet succeeded in decentralising metal testing.[145] The literature review carried out above highlighted several areas that could be impeding the ability of these sensors to replace current methods of testing including modification layer instability, complicated fabrication processes, sensor lifetime, and an inability to detect in real samples with the need for additional buffers or reagents. In this thesis we propose a strategy to help overcome these issues by using NPG modified gold IDE arrays for *in situ* electrochemical pH control for the detection of lead in tap water.

1.5 Thesis Objectives

- One of the main aims of the thesis is to develop low-power sensors for point-of-care analysis. There simulations are an integral part of this research to examine optimum electrode geometry for reducing the size of the arrays while maintaining optimum performance.

- To further enhance the optimised IDE arrays, a simple NPG modification will be used. The modification with NPG will increase the surface area of the electrodes thus enhancing performance without the need to increase the overall size of the array.

- Another significant aim of this research is the ability to use these sensors for reagent-free detection. Therefore, the final aim of this thesis is to exploit the IDE arrays for electrochemical pH control in tap water negating the need to adjust the pH with the addition of a buffer.

1.6 References

1. Wang, J. Fundamental Concepts. In *Analytical Electrochemistry*, Wang, J., Ed.; 2006; Chapter 1, pp 1-28.

2. Ciobanu, M.; Wilburn, J. P.; Krim, M. L.; Cliffel, D. E. Fundamentals. In *Handbook of Electrochemistry*, Zoski, C. G., Ed.; 2008; Chapter 1, pp 3-30.

3. Marcus, R. A., Electron transfer reactions in chemistry. Theory and experiment. *Reviews of Modern Physics* **1993**, 65, 599-610.

4. Wang, X.; Tabakman, S. M.; Dai, H., Atomic Layer Deposition of Metal Oxides on Pristine and Functionalized Graphene. *Journal of the American Chemical Society* **2008**, 130, 8152-8153.

5. Franaszczuk, K.; Herrero, E.; Zelenay, P.; Wieckowski, A.; Wang, J.; Masel, R. I., A comparison of electrochemical and gas-phase decomposition of methanol on platinum surfaces. *The Journal of Physical Chemistry* **1992**, 96, 8509-8516.

6. Anna L. Barker, M. G., Julie V. Macpherson, Christopher J. Slevin, Patrick R. Unwin, Scanning electrochemical microscopy: beyond the solid/liquid interface. *Analytica Chimica Acta* **1999**, 223-240.

7. Potentiostat. https://www3.nd.edu/~kamatlab/documents/facilities/potentiostat.pdf (02/04/2021),

8. Vyskočil, V.; Barek, J., Mercury electrodes–possibilities and limitations in environmental electroanalysis. *Critical Reviews in Analytical Chemistry* **2009**, 39, 173-188.

9. Bard, A. J.; Faulkner, L. R. Polarography and Pulse Voltammetry. In *Electrochemical Methods: Fundamentals and Applications*; 2001; Chapter 7, pp 261-301.

10. Smith, T. J.; Stevenson, K. J. Reference Electrodes. In *Handbook of Electrochemistry*, Zoski, C. G., Ed.; 2007; Chapter 4, pp 73-108.

11. Two, Three, and Four Electrode Experiments. https://www.gamry.com/application-notes/instrumentation/two-three-and-four-electrode-experiments/ (04/02/2020),

12. Understanding the Specifications of your Potentiostat. https://www.gamry.com/application-notes/instrumentation/understanding-specs-of-potentiostat/ (04/02/2020),

13. Edwards, G. A.; Bergren, A. J.; Porter, M. D. 8 - Chemically Modified Electrodes. In *Handbook of Electrochemistry*, Zoski, C. G., Ed.; Elsevier: Amsterdam, 2007, pp 295-327.

14. Potentiostat Fundamentals: Introduction to Potentiostats. https://www.gamry.com/application-notes/instrumentation/potentiostat-fundamentals/ (27/03/2021),

15. Bard, A. J.; Faulkner, L. R. Introduction and Overview of Electrode Processes. In *Electrochemical Methods: Fundamentals and Applications*; 2001, pp 1-44.

16. Kahlert, H. Reference electrodes. In *Electroanalytical methods*; Springer: 2010, pp 291-308.

17. Spitzer, P.; Wunderli, S. Reference Electrode for Aqueous Solutions. In *Handbook of Reference Electrodes*, Inzelt, G.; Lewenstam, A.; Scholz, F., Eds.; 2013; Chapter 5, pp 77-143.

18. Zhou, J.; Ren, K.; Zheng, Y.; Su, J.; Zhao, Y.; Ryan, D.; Wu, H., Fabrication of a microfluidic Ag/AgCl reference electrode and its application for portable and disposable electrochemical microchips. *Electrophoresis* **2010**, 3083-3089.

19. Polk, B. J.; Stelzenmuller, A.; Mijares, G.; MacCrehan, W.; Gaitan, M., Ag/AgCl microelectrodes with improved stability for microfluidics. *Sensors and Actuators B: Chemical* **2006**, 239-247.

20. Inzelt, G. Pseudo-reference electrodes. In *Handbook of Reference Electrodes*; 2013, pp 331-332.

21. Biologic How potentiostats work and their use in Science & Inductry (Electrochemistry Basic Series). https://www.biologic.net/topics/what-is-a-potentiostat-how-potentiostats-work-and-their-use-in-science-and-industry/ (15/11/2021),

22. Kelly, R. S., Analytical electrochemistry: the basic concepts. *Analytical Sciences Digital Library* **2009**.

23. Wahl, A. J. C. Fabrication, Charactersiation and electroanalysis at 1-dimensional nanoctructures. University College Cork, 2013.

24. Gongadze, E.; Peterson, S.; Beck, U.; Van Rienen, U. Classical Models of the Interface between an Electrode and and Electrolyte. In COMSOL Conference, Milan, 2009; Milan, 2009.

25. Ciobanu, M.; Wilburn, J. P.; Krim, M. L.; Cliffel, D. E. Equations Governing Modes of Mass Transfer. In *Handbook of Electrochemistry*, Zoski, C. G., Ed.; 2007; Chapter 1. Fundamentals, pp 17-20.

26. Wang, J. Study of Electrode Reactions and Interfacial Properties. In *Analytical Electrochemistry*; 2006, pp 29-66.

27. Bard, A. J.; Faulkner, L. R. Sqaure Wave Voltammetry. In *Electrochemical Methods: Fundamentals and Applications*; John Wiley & Sons, Inc.: 2001; Chapter 7. Polarography and Pulse Voltammetry, pp 293-299.

28. Osteryoung, J. G.; Osteryoung, R. A., Square wave voltammetry. *Analytical Chemistry* **1985**, 57, 101-110.

29. Square Wave Voltammetry.

30. Denuault, G.; Sosna, M.; Williams, K.-J. Stripping Analysis. In *Handbook of Electrochemistry*, Zoski, C. G., Ed.; 2007; Chapter 11. Classical Experiments, pp 446-447.

31. Fundamentals of Stripping Voltammetry.

32. Kokkinos, C.; Economou, A.; Raptis, I., Microfabricated disposable lab-on-a-chip sensors with integrated bismuth microelectrode arrays for voltammetric determination of trace metals. *Analytica Chimica Acta* **2012**, 710, 1-8.

33. Štulík, K.; Amatore, C.; Holub, K.; Mareček, V.; Kutner, W., Microelectrodes. Definitions, characterization, and applications. *Pure Appl. Chem* **2000**, 72, 1483-1492.

34. Li, D.; Batchelor-McAuley, C.; Chen, L.; Compton, R. G., Band Electrodes in Sensing Applications: Response Characteristics and Band Fabrication Methods. *ACS Sensors* **2019**, 4, 2250-2266.

35. Bard, A. J.; Faulkner, L. R. Basic Potential Step Methods. In *Electrochemical Methods: Fundamentals and Applications*; John Wiley & Sons: 2001; Chapter 5, pp 156-225.

36. Ohmic Drop: Part 1 - Basic Principles. *Metrohm Autolab* **2019**.

37. Gardner, R. D.; Zhou, A.; Zufelt, N. A., Development of a microelectrode array sensing platform for combination electrochemical and spectrochemical aqueous ion testing. *Sensors and Actuators B: Chemical* **2009**, 136, 177-185.

38. Forster, R. J.; Keyes, T. E. 6 - Ultramicroelectrodes. In *Handbook of Electrochemistry*, Zoski, C. G., Ed.; Elsevier: Amsterdam, 2007, pp 155-171.

39. Wang, J. Practical Considerations. In *Analytical Electrochemistry*; John Wiley & Sons, Inc.: 2006; Chapter 4, pp 115-164.

40. Streeter, I.; Fietkau, N.; del Campo, J.; Mas, R.; Mũnoz, F. X.; Compton, R. G., Voltammetry at Regular Microband Electrode Arrays: Theory and Experiment. *The Journal of Physical Chemistry C* **2007**, 111, 12058-12066.

41. Varco Shea, T.; Bard, A. J., Digital simulation of homogeneous chemical reactions coupled to heterogeneous electron transfer and applications at platinum/mica/platinum ultramicroband electrodes. *Analytical Chemistry* **1987**, 59, 2101-2111.

42. Streeter, I.; Compton, R. G., Linear Sweep Voltammetry at Randomly Distributed Arrays of Microband Electrodes. *The Journal of Physical Chemistry C* **2007**, 111, 15053-15058.

43. Barnes, E. O.; Lewis, G. E.; Dale, S. E.; Marken, F.; Compton, R. G., Generator-collector double electrode systems: a review. *Analyst* **2012**, 137, 1068-81.

44. Min, J.; Baeumner, A. J., Characterisation and Optimisation of Interdigitated Ultramicroelectrode Arrays as Electrochemical Biosensor Transducers. *Electroanalysis* **2003**, 16.

45. Niwa, O.; Morita, M.; Tabei, H., Electrochemical behaviour of reversible redox species at interdigitated array electrodes with different geometries: consideration of redox cycling and collection efficiency. *Analytical Chemistry* **1990**, 62, 447-452.

46. Godino, N.; Borrisé, X.; Muñoz, F. X.; del Campo, F. J.; Compton, R. G., Mass Transport to Nanoelectrode Arrays and Limitations of the Diffusion Domain Approach: Theory and Experiment. *The Journal of Physical Chemistry C* **2009**, 113, 11119-11125.

47. Molina, A.; Gonzalez, J.; Henstridge, M. C.; Compton, R. G., Voltammetry of Electrochemically Reversible Systems at Electrodes of Any Geometry: A General, Explicit Analytical Characterization. *The Journal of Physical Chemistry C* **2011**, 115, 4054-4062.

48. Guerrette, J. P.; Percival, S. J.; Zhang, B., Voltammetric Behavior of Gold Nanotrench Electrodes. *Langmuir* **2011**, 27, 12218-12225.

49. Davies, T. J.; Compton, R. G., The cyclic and linear sweep voltammetry of regular and random arrays of microdisc electrodes: Theory. *Journal of Electroanalytical Chemistry* **2005**, 585, 63-82.

50. Davies, T. J.; Ward-Jones, S.; Banks, C. E.; del Campo, J.; Mas, R.; Muñoz, F. X.; Compton, R. G., The cyclic and linear sweep voltammetry of regular arrays of microdisc electrodes: Fitting of experimental data. *Journal of Electroanalytical Chemistry* **2005**, 585, 51-62.

51. Tekkaya, A. E.; Soyarslan, C. Finite Element Method. In *CIRP Encyclopedia of Production Engineering*, Laperrière, L.; Reinhart, G., Eds.; Springer Berlin Heidelberg: Berlin, Heidelberg, 2014, pp 508-514.

52. In *Multiphysics Cyclopedia*; COMSOL Multiphysics, 2016; Vol. 2021.

53. World Health Organisation, Global health risks: Mortality and burden of disease attributable to selected major risks. **2009**.

54. Meyer, P. A.; Pivetz, T.; Dignam, T. A.; Schoonover, J.; Brody, D., Surveillance for Elevated Blood Lead Levels Among Children - United States, 1997 - 2001. *Morbidity and Morality Weekly* **2003**, 52, 1.

55. World Health Organisation, Exposure to lead: A major public health concern. **2010**.

56. Gumpu, M. B.; Sethuraman, S.; Krishnan, U. M.; Rayappan, J. B. B., A review on detection of heavy metal ions in water – An electrochemical approach. *Sensors and Actuators B: Chemical* **2015**, 213, 515-533.

57. de Vries, W.; Römkens, P. F. A. M.; Schütze, G., Critical soil concentrations of cadmium, lead, and mercury in view of health effects on humans and animals. *Rev Environ Contam Toxicol* **2007**, 191, 91-130.

58. Claudio, E. S.; Godwin, H. A.; Magyar, J. S. Fundamental Coordination Chemistry, Environmental Chemistry, and Biochemistry of Lead(II). In *Progress in Inorganic Chemistry*; 2002, pp 1-144.

59. Nur Abdul Aziz, S. F.; Zawawi, R.; Alang Ahmad, S. A., An Electrochemical Sensing Platform for the Detection of Lead Ions Based on Dicarboxyl-Calix[4]arene. *Electroanalysis* **2018**, 30, 533-542.

60. HSE Lead in Drining Water. http://www.hse.ie/eng/health/hl/water/drinkingwater/lead/

61. Drinking water in areas has up to 10 and 11 times more lead than allowed. *Irish Examiner* 2020.

62. Pujol, L.; Evrard, D.; Groenen-Serrano, K.; Freyssinier, M.; Ruffien-Cizsak, A.; Gros, P., Electrochemical sensors and devices for heavy metals assay in water: the French groups' contribution. *Frontiers in Chemistry* **2014**, 2.

63. Waheed, A.; Mansha, M.; Ullah, N., Nanomaterials-based electrochemical detection of heavy metals in water: Current status, challenges and future direction. *TrAC Trends in Analytical Chemistry* **2018**, 105, 37-51.

64. Li, M.; Gou, H.; Al-Ogaidi, I.; Wu, N., Nanostructured Sensors for Detection of Heavy Metals: A Review. *ACS Sustainable Chemistry & Engineering* **2013**, 1, 713-723.

65. Hanrahan, G.; Patil, D. G.; Wang, J., Electrochemical sensors for environmental monitoring: design, development and applications. *J Environ Monit* **2004**, 6, 657-664.

66. Murphy, A.; Seymour, I.; Rohan, J.; O'Riordan, A.; O'Connell, I., Portable data acquisition system for nano and ultra-micro scale electrochemical sensors. *IEEE Sensors Journal* **2020**, 21, 3210-3215.

67. Li, Y.; Liu, J.; Yu, F.; Tang, H.; Zhao, F.; Ye, B.-C.; Chen, W.; Lv, X., Electrochemical determination of trace lead(II) with enhanced sensitivity and selectivity by three-dimensional nanoporous gold leaf and self-assembled homocysteine monolayer. *Journal of Electroanalytical Chemistry* **2015**, 758, 78-84.

68. Hale, P.; Thurgate, S.; Wilkie, P., Lead underpotential deposition on Au(110). *Surface and Interface Analysis* **2003**, 35, 842-851.

69. Herzog, G.; Arrigan, D. W., Determination of trace metals by underpotential deposition–stripping voltammetry at solid electrodes. *TrAC Trends in Analytical Chemistry* **2005**, 24, 208-217.

70. Arduini, F.; Calvo, J. Q.; Palleschi, G.; Moscone, D.; Amine, A., Bismuth-modified electrodes for lead detection. *TrAC Trends in Analytical Chemistry* **2010**, 29, 1295-1304.

71. Wang, J.; Lu, J.; Hocevar, S. B.; Farias, P. A. M.; Ogorevc, B., Bismuth-Coated Carbon Electrodes for Anodic Stripping Voltammetry. *Analytical Chemistry* **2000**, 72, 3218-3222.

72. Wang, L.; Jing, G.; Cui, T. Highly sensitive micro sensor with nafion coated bismuth for trace lead determination. In 2017 19th International Conference on Solid-State Sensors, Actuators and Microsystems (TRANSDUCERS), 18-22 June 2017, 2017; 2017; pp 1524-1527.

73. Economou, A., Bismuth-film electrodes: recent developments and potentialities for electroanalysis. *TrAC Trends in Analytical Chemistry* **2005**, 24, 334-340.

74. Hwang, G.-H.; Han, W.-K.; Park, J.-S.; Kang, S.-G., An electrochemical sensor based on the reduction of screen-printed bismuth oxide for the determination of trace lead and cadmium. *Sensors and Actuators B: Chemical* **2008**, 135, 309-316.

75. Serrano, N.; Díaz-Cruz, J. M.; Ariño, C.; Esteban, M., Ex situ Deposited Bismuth Film on Screen-Printed Carbon Electrode: A Disposable Device for Stripping Voltammetry of Heavy Metal Ions. *Electroanalysis* **2010**, 22, 1460-1467.

76. Hwang, J.-H.; Wang, X.; Zhao, D.; Rex, M. M.; Cho, H. J.; Lee, W. H., A novel nanoporous bismuth electrode sensor for in situ heavy metal detection. *Electrochimica Acta* **2019**, 298, 440-448.

77. Wang, L.; Jing, G.; Cui, T., Nafion coated flexible bismuth sensor for trace lead and cadmium determination. *Microsystem Technologies* **2018**, 24, 3697-3704.

78. Lezi, N.; Economou, A.; Dimovasilis, P. A.; Trikalitis, P. N.; Prodromidis, M. I., Disposable screen-printed sensors modified with bismuth precursor compounds for the rapid voltammetric screening of trace Pb(II) and Cd(II). *Analytica Chimica Acta* **2012**, 728, 1-8.

79. Rico, M. Á. G.; Olivares-Marín, M.; Gil, E. P., Modification of carbon screen-printed electrodes by adsorption of chemically synthesized Bi nanoparticles for the voltammetric stripping detection of Zn(II), Cd(II) and Pb(II). *Talanta* **2009**, 80, 631-635.

80. Kanyong, P.; Rawlinson, S.; Davis, J., Gold nanoparticle modified screen-printed carbon arrays for the simultaneous electrochemical analysis of lead and copper in tap water. *Mikrochimica Acta* **2016**, 183, 2361-2368.

81. Xuan, X.; Park, J. Y., A miniaturized and flexible cadmium and lead ion detection sensor based on micro-patterned reduced graphene oxide/carbon nanotube/bismuth composite electrodes. *Sensors and Actuators B: Chemical* **2018**, 255, 1220-1227.

82. Zou, Z.; Jang, A.; MacKnight, E.; Wu, P.-M.; Do, J.; Bishop, P. L.; Ahn, C. H., Environmentally friendly disposable sensors with microfabricated on-chip planar bismuth electrode for in situ heavy metal ions measurement. *Sensors and Actuators B: Chemical* **2008**, 134, 18-24.

83. Zhang, W.; Zhang, H.; Williams, S. E.; Zhou, A., Microfabricated three-electrode on-chip PDMS device with a vibration motor for stripping voltammetric detection of heavy metal ions. *Talanta* **2015**, 132, 321-326.

84. Xiao, L.; Xu, H.; Zhou, S.; Song, T.; Wang, H.; Li, S.; Gan, W.; Yuan, Q., Simultaneous detection of Cd(II) and Pb(II) by differential pulse anodic stripping voltammetry at a nitrogen-doped microporous carbon/Nafion/bismuth-film electrode. *Electrochimica Acta* **2014**, 143, 143-151.

85. Lee, S.; Park, S.-K.; Choi, E.; Piao, Y., Voltammetric determination of trace heavy metals using an electrochemically deposited graphene/bismuth nanocomposite film-modified glassy carbon electrode. *Journal of Electroanalytical Chemistry* **2016**, 766, 120-127.

86. Xu, Z.; Fan, X.; Ma, Q.; Tang, B.; Lu, Z.; Zhang, J.; Mo, G.; Ye, J.; Ye, J., A sensitive electrochemical sensor for simultaneous voltammetric sensing of cadmium and lead based on Fe3O4/multiwalled carbon nanotube/laser scribed graphene composites functionalized with chitosan modified electrode. *Materials Chemistry and Physics* **2019**, 238, 121877.

87. Qin, D.; Xu, R.; Shen, H.; Mamat, X.; Wang, L.; Gao, S.; Wang, Y.; Yalikun, N.; Wagberg, T.; Zhang, S.; yuan, Q.; Li, Y.; Hu, G., Protic salt-based nitrogen-doped mesoporous carbon for simultaneous electrochemical detection of Cd(ii) and Pb(ii). *RSC Advances* **2017**, 7, 36929-36934.

88. Tang, L.; Chen, J.; Zeng, G.; Zhu, Y.; Zhang, Y.; Zhou, Y.; Xie, X.; Yang, G.; Zhang, S., Ordered Mesoporous Carbon and Thiolated Polyaniline Modified Electrode for Simultaneous Determination of Cadmium(II) and Lead(II) by Anodic Stripping Voltammetry. *Electroanalysis* **2014**, 26, 2283-2291.

89. Xu, H.; Zeng, L.; Xing, S.; Xian, Y.; Shi, G.; Jin, L., Ultrasensitive Voltammetric Detection of Trace Lead(II) and Cadmium(II) Using MWCNTs-Nafion/Bismuth Composite Electrodes. *Electroanalysis* **2008**, 20, 2655-2662.

90. Hao, C.; Shen, Y.; Shen, J.; Xu, K.; Wang, X.; Zhao, Y.; Ge, C., A glassy carbon electrode modified with bismuth oxide nanoparticles and chitosan as a sensor for Pb(II) and Cd(II). *Microchimica Acta* **2016**, 183, 1823-1830.

91. Zhu, X.; Liu, B.; Wu, L.; Chen, S.; Yang, J.; Liang, S.; Xiao, K.; Hu, J.; Hou, H., Synthesis of 3D hierarchically porous carbon@Bi-BiOCl nanocomposites via in situ generated NaCl crystals as templates for highly sensitive detection of Pb2+ and Cd2+. *Electrochimica Acta* **2019**, 318, 460-470.

92. Lu, Z.; Dai, W.; Lin, X.; Liu, B.; Zhang, J.; Ye, J.; Ye, J., Facile one-step fabrication of a novel 3D honeycomb-like bismuth nanoparticles decorated N-doped carbon nanosheet frameworks: Ultrasensitive electrochemical sensing of heavy metal ions. *Electrochimica Acta* **2018**, 266, 94-102.

93. Shi, L.; Li, Y.; Rong, X.; Wang, Y.; Ding, S., Facile fabrication of a novel 3D graphene framework/Bi nanoparticle film for ultrasensitive electrochemical assays of heavy metal ions. *Analytica Chimica Acta* **2017**, 968, 21-29.

94. Cui, L.; Wu, J.; Ju, H., Synthesis of Bismuth-Nanoparticle-Enriched Nanoporous Carbon on Graphene for Efficient Electrochemical Analysis of Heavy-Metal Ions. *Chemistry – A European Journal* **2015**, 21, 11525-11530.

95. Lazanas, A. C.; Tsirka, K.; Paipetis, A. S.; Prodromidis, M. I., 2D bismuthene/graphene modified electrodes for the ultra-sensitive stripping voltammetric determination of lead and cadmium. *Electrochimica Acta* **2020**, 336, 135726.

96. Torma, F.; Kádár, M.; Tóth, K.; Tatár, E., Nafion®/2,2′-bipyridyl-modified bismuth film electrode for anodic stripping voltammetry. *Analytica Chimica Acta* **2008**, 619, 173-182.

97. Cheng, Y.-m.; Fa, H.-b.; Yin, W.; Hou, C.-j.; Huo, D.-q.; Liu, F.-m.; Zhang, Y.; Chen, C., A sensitive electrochemical sensor for lead based on gold nanoparticles/nitrogen-doped graphene composites functionalized with l-cysteine-modified electrode. *Journal of Solid State Electrochemistry* **2016**, 20, 327-335.

98. Xu, C.; Liu, J.; Bi, Y.; Ma, C.; Bai, J.; Hu, Z.; Zhou, M., Biomass derived worm-like nitrogen-doped-carbon framework for trace determination of toxic heavy metal lead (II). *Analytica Chimica Acta* **2020**, 1116, 16-26.

99. Yan, P.; Zhang, S.; Zhang, C.; Liu, Z.; Tang, A., Palygorskite modified with N-doped carbon for sensitive determination of lead(II) by differential pulse anodic stripping voltammetry. *Microchimica Acta* **2019**, 186, 706.

100. Qin, D.; Chen, A.; Mamat, X.; Li, Y.; Hu, X.; Wang, P.; Cheng, H.; Dong, Y.; Hu, G., Double-shelled yolk-shell Si@C microspheres based electrochemical sensor for determination of cadmium and lead ions. *Analytica Chimica Acta* **2019**, 1078, 32-41.

101. Gao, S.; Xu, C.; Yalikun, N.; Mamat, X.; Li, Y.; Wågberg, T.; Hu, X.; Liu, J.; Luo, J.; Hu, G., Sensitive and Selective Differential Pulse Voltammetry Detection of Cd(II) and Pb(II) Using Nitrogen-Doped Porous Carbon Nanofiber Film Electrode. *Journal of The Electrochemical Society* **2017**, 164, H967-H974.

102. Simpson, A.; Pandey, R. R.; Chusuei, C. C.; Ghosh, K.; Patel, R.; Wanekaya, A. K., Fabrication characterization and potential applications of carbon nanoparticles in the detection of heavy metal ions in aqueous media. *Carbon* **2018**, 127, 122-130.

103. Sun, Y.-F.; Sun, J.-H.; Wang, J.; Pi, Z.-X.; Wang, L.-C.; Yang, M.; Huang, X.-J., Sensitive and anti-interference stripping voltammetry analysis of Pb(II) in water using flower-like MoS2/rGO composite with ultra-thin nanosheets. *Analytica Chimica Acta* **2019**, 1063, 64-74.

104. Li, L.; Liu, D.; Shi, A.; You, T., Simultaneous stripping determination of cadmium and lead ions based on the N-doped carbon quantum dots-graphene oxide hybrid. *Sensors and Actuators B: Chemical* **2018**, 255, 1762-1770.

105. Guo, Z.; Li, D.-d.; Luo, X.-k.; Li, Y.-h.; Zhao, Q.-N.; Li, M.-m.; Zhao, Y.-t.; Sun, T.-s.; Ma, C., Simultaneous determination of trace Cd(II), Pb(II) and Cu(II) by differential pulse anodic stripping voltammetry using a reduced graphene oxide-chitosan/poly-l-lysine nanocomposite modified glassy carbon electrode. *Journal of Colloid and Interface Science* **2017**, 490, 11-22.

106. Lee, P. M.; Chen, Z.; Li, L.; Liu, E., Reduced graphene oxide decorated with tin nanoparticles through electrodeposition for simultaneous determination of trace heavy metals. *Electrochimica Acta* **2015**, 174, 207-214.

107. Khan, A. A. P.; Khan, A.; Asiri, A. M.; Alam, M. M.; Rahman, M. M.; Shaban, M., Surfactant-assisted graphene oxide/methylaniline nanocomposites for lead ionic sensor development for the environmental remediation in real sample matrices. *International Journal of Environmental Science and Technology* **2019**, 16, 8461-8470.

108. Bai, F.; Li, Q.; Yang, T.; Chen, J.; Hou, X., Simultaneous determination of Cd(II) and Pb(II) using electrode modified by FeAl2O4-AlOOH-reduced graphene oxide hybrids. *Ionics* **2019**, 25, 2351-2360.

109. Kong, Y.; Wu, T.; Wu, D.; Zhang, Y.; Wang, Y.; Du, B.; Wei, Q., An electrochemical sensor based on Fe3O4@PANI nanocomposites for sensitive detection of Pb2+ and Cd2+. *Analytical Methods* **2018**, 10, 4784-4792.

110. Oliveira, V. H. B.; Rechotnek, F.; da Silva, E. P.; Marques, V. d. S.; Rubira, A. F.; Silva, R.; Lourenço, S. A.; Muniz, E. C., A sensitive electrochemical sensor for Pb2+ ions based on ZnO nanofibers functionalized by L-cysteine. *Journal of Molecular Liquids* **2020**, 309, 113041.

111. Ye, W.; Li, Y.; Wang, J.; Li, B.; Cui, Y.; Yang, Y.; Qian, G., Electrochemical detection of trace heavy metal ions using a Ln-MOF modified glass carbon electrode. *Journal of Solid State Chemistry* **2020**, 281, 121032.

112. Ahmad, I.; Arshad, M. N.; Rahman, M. M.; Asiri, A. M.; Sheikh, T. A.; Aqlan, F. M., Crystal structure of N′-[(E)-(2-hydroxynaphthalen-1-yl) methylidene] benzenesulfonohydrazide (HNMBSH) and its application as Pb2+ ion sensor by its fabrication onto glassy carbon electrode. *Inorganica Chimica Acta* **2017**, 467, 297-306.

113. Huang, H.; Zhu, W.; Gao, X.; Liu, X.; Ma, H., Synthesis of a novel electrode material containing phytic acid-polyaniline nanofibers for simultaneous determination of cadmium and lead ions. *Analytica Chimica Acta* **2016**, 947, 32-41.

114. Kaur, B.; Srivastava, R.; Satpati, B., Ultratrace detection of toxic heavy metal ions found in water bodies using hydroxyapatite supported nanocrystalline ZSM-5 modified electrodes. *New Journal of Chemistry* **2015**, 39, 5137-5149.

115. Lin, H.; Li, M.; Mihailovič, D., Simultaneous Determination of Copper, Lead, and Cadmium Ions at a Mo6S9-xIx Nanowires Modified Glassy Carbon Electrode Using Differential Pulse Anodic Stripping Voltammetry. *Electrochimica Acta* **2015**, 154, 184-189.

116. Ji, C. Y.; Li, P.; Ma, H. W.; Yang, G. C.; Zhang, M., Ultrasensitive and stable determination of lead ions by a glassy carbon electrode modified with a phenanthroline-based electropolymerized film. *RSC Advances* **2015**, 5, 797-802.

117. Philips, M. F.; Gopalan, A. I.; Lee, K.-P., Development of a novel cyano group containing electrochemically deposited polymer film for ultrasensitive simultaneous detection of trace level cadmium and lead. *Journal of Hazardous Materials* **2012**, 237-238, 46-54.

118. Pan, D.; Wang, Y.; Chen, Z.; Lou, T.; Qin, W., Nanomaterial/Ionophore-Based Electrode for Anodic Stripping Voltammetric Determination of Lead: An Electrochemical Sensing Platform toward Heavy Metals. *Analytical Chemistry* **2009**, 81, 5088-5094.

119. Hassan, K. M.; Elhaddad, G. M.; AbdelAzzem, M., Voltammetric determination of cadmium(II), lead(II) and copper(II) with a glassy carbon electrode modified with silver nanoparticles deposited on poly(1,8-diaminonaphthalene). *Microchimica Acta* **2019**, 186, 440.

120. Zeinu, K. M.; Hou, H.; Liu, B.; Yuan, X.; Huang, L.; Zhu, X.; Hu, J.; Yang, J.; Liang, S.; Wu, X., A novel hollow sphere bismuth oxide doped mesoporous carbon nanocomposite material derived from sustainable biomass for picomolar electrochemical detection of lead and cadmium. *Journal of Materials Chemistry A* **2016**, 4, 13967-13979.

121. Zou, J.; Mao, D.; Arramel; Li, N.; Jiang, J., Reliable and selective lead-ion sensor of sulfur-doped graphitic carbon nitride nanoflakes. *Applied Surface Science* **2020**, 506, 144672.

122. Yantasee, W.; Charnhattakorn, B.; Fryxell, G. E.; Lin, Y.; Timchalk, C.; Addleman, R. S., Detection of Cd, Pb, and Cu in non-pretreated natural waters and urine with thiol functionalized mesoporous silica and Nafion composite electrodes. *Analytica Chimica Acta* **2008**, 620, 55-63.

123. Gumpu, M. B.; Veerapandian, M.; Krishnan, U. M.; Rayappan, J. B. B., Simultaneous electrochemical detection of Cd(II), Pb(II), As(III) and Hg(II) ions using ruthenium(II)-textured graphene oxide nanocomposite. *Talanta* **2017**, 162, 574-582.

124. Rahm, C. E.; Torres-Canas, F.; Gupta, P.; Poulin, P.; Alvarez, N. T., Inkjet Printed Multi-Walled Carbon Nanotube Sensor for the Detection of Lead in Drinking Water. *Electroanalysis* **2020**, n/a.

125. Wittstock, A.; Wichmann, A.; Biener, J.; Bäumer, M., Nanoporous gold: a new gold catalyst with tunable properties. *Faraday Discuss* **2011**, 152, 87-98; discussion 99-120.

126. Nagle, L. C.; Rohan, J. F., Nanoporous gold catalyst for direct ammonia borane fuel cells. *Journal of the Electrochemical Society* **2011**, 158, B772.

127. Biener, J.; Hodge, A. M.; Hayes, J. R.; Volkert, C. A.; Zepeda-Ruiz, L. A.; Hamza, A. V.; Abraham, F. F., Size effects on the mechanical behavior of nanoporous Au. *Nano letters* **2006**, 6, 2379-2382.

128. Ji, C.; Searson, P. C., Synthesis and Characterization of Nanoporous Gold Nanowires. *The Journal of Physical Chemistry B* **2003**, 107, 4494-4499.

129. Forty, A. J., Corrosion micromorphology of noble metal alloys and depletion gilding. *Nature* **1979**, 282, 597-598.

130. Bhattarai, J. K.; Neupane, D.; Nepal, B.; Mikhaylov, V.; Demchenko, A. V.; Stine, K. J., Structure and applications of gold in nanoporous form. *Noble and Precious Metals-Properties, Nanoscale Effects and Applications; Seehra, MS, Bristow, AD, Eds* **2018**, 341-365.

131. Nagle, L. C.; Wahl, A.; Ogourstov, V.; Seymour, I.; Barry, F.; Rohan, J. F.; Mac Loughlin, R., Electrochemical Discrimination of Salbutamol from Its Excipients in VentolinTM at Nanoporous Gold Microdisc Arrays. *Sensors* **2021**, 21, 3975.

132. Twomey, K.; Nagle, L. C.; Said, A.; Barry, F.; Ogurtsov, V. I., Characterisation of Nanoporous Gold for Use in a Dissolved Oxygen Sensing Application. *BioNanoScience* **2015**, 5, 55-63.

133. Galvin, P.; Padmanathan, N.; Razeeb, K. M.; Rohan, J. F.; Nagle, L. C.; Wahl, A.; Moore, E.; Messina, W.; Twomey, K.; Ogurtsov, V., Nanoenabling electrochemical sensors for life sciences applications. *Journal of Materials Research* **2017**, 32, 2883-2904.

134. Pia, G.; Sogne, E.; Falqui, A.; Delogu, F., Ag surface segregation in nanoporous Au catalysts during CO oxidation. *Scientific reports* **2018**, 8, 1-9.

135. Seker, E.; Reed, M. L.; Begley, M. R., Nanoporous gold: Fabrication, characterization, and applications. *Materials* **2009**, 2, 2188-2215.

136. Hossain, M. N.; Liu, Z.; Wen, J.; Chen, A., Enhanced catalytic activity of nanoporous Au for the efficient electrochemical reduction of carbon dioxide. *Applied Catalysis B: Environmental* **2018**, 236, 483-489.

137. Wang, R.; Liu, J.; Liu, P.; Bi, X.; Yan, X.; Wang, W.; Meng, Y.; Ge, X.; Chen, M.; Ding, Y., Ultra-thin layer structured anodes for highly durable low-Pt direct formic acid fuel cells. *Nano Research* **2014**, 7, 1569-1580.

138. Bhattarai, J. K.; Neupane, D.; Nepal, B.; Mikhaylov, V.; Demenchenko, A. V.; Stine, K. J., In *InTechOpen*, Seehra, M. S.; Bristow, A. D., Eds.; 2017.

139. Li, Y.; Liu, Y.; Liu, J.; Liu, J.; Tang, H.; Cao, C.; Zhao, D.; Ding, Y., Molecularly imprinted polymer decorated nanoporous gold for highly selective and sensitive electrochemical sensors. *Scientific Reports* **2015**, 5, 7699.

140. Seymour, I.; O'Sullivan, B.; Lovera, P.; Rohan, J. F.; O'Riordan, A., Electrochemical detection of free-chlorine in Water samples facilitated by in-situ pH control using interdigitated microelectrodes. *Sensors and Actuators B: Chemical* **2020**, 325, 128774.

141. Wasiewska, L. A.; Seymour, I.; Patella, B.; Inguanta, R.; Burgess, C. M.; Duffy, G.; O'Riordan, A., Reagent free electrochemical-based detection of silver ions at interdigitated microelectrodes using in-situ pH control. *Sensors and Actuators B: Chemical* **2021**, 333, 129531.

142. O'Sullivan, B.; Patella, B.; Daly, R.; Seymour, I.; Robinson, C.; Lovera, P.; Rohan, J.; Inguanta, R.; O'Riordan, A., A simulation and experimental study of electrochemical pH control at gold interdigitated electrode arrays. *Electrochimica Acta* **2021**, 395, 139113.

143. Read, T. L.; Bitziou, E.; Joseph, M. B.; Macpherson, J. V., In Situ Control of Local pH Using a Boron Doped Diamond Ring Disk Electrode: Optimizing Heavy Metal (Mercury) Detection. *Analytical Chemistry* **2014**, 86, 367-371.

144. Michaud, P. A.; Panizza, M.; Ouattara, L.; Diaco, T.; Foti, G.; Comninellis, C., Electrochemical oxidation of water on synthetic boron-doped diamond thin film anodes. *Journal of Applied Electrochemistry* **2003**, 33, 151-154.

145. Wang, J.; Tian, B.; Wang, J.; Lu, J.; Olsen, C.; Yarnitzky, C.; Olsen, K.; Hammerstrom, D.; Bennett, W., Stripping analysis into the 21st century: faster, smaller, cheaper, simpler and better. *Analytica Chimica Acta* **1999**, 385, 429-435.

Chapter 2 Electrode Design, Simulation, Fabrication & Characterisation

2.1 Introduction

This chapter takes an in-depth look at the design and fabrication of IDE arrays. The goal under-pinning this thesis is the development of a sensing platform for water quality monitoring. Therefore, key aspects governing the design of these IDE arrays are sensitivity, cost, and size. Many contaminants of water are in very low quantities, such as lead, which is measured in the ppb scale. Therefore, highly sensitive arrays are essential. Size and cost of the sensors go together, reducing the size of the sensors reduces the cost of material used and power consumption of the sensor thus reducing the cost. Size is also important for the implementation of the sensors; miniaturisation of sensors allows for use of smaller handheld and portable monitoring devices.

The simulation of proposed electrode designs was integral to this chapter. Much of the background information pertaining to the COMSOL Multiphysics® carried out in this chapter is discussed in Chapter 1. The simulation of both diffusion profiles and peak or steady state current of the oxidation of ferrocene carboxylic acid were used to get a clear indication of sensor performance. Initial simulations were carried out on the inter-electrode gap, scan rate and height of the electrodes. These highlighted the need for sufficient spacing to prevent diffusion layer overlap, the time dependence of diffusion and how the sensor performance increases with electrode area. The introduction of GC electrodes made it possible to place the electrodes closer together without being impacted by diffusion layer overlap. The ability to place the electrodes closer together greatly reduces the array footprint thus reducing the cost of fabrication and power consumption of the array. Additionally, the enhanced performance obtained from GC electrodes, as discussed in Chapter 1 indicated a 4.3x current amplification for the simulated current of some of the GC array designs. The final design feature investigated using simulations was the introduction of a Hafnium Oxide (HfO_2) capping layer. To our knowledge, the use of

HfO_2 as a capping layer is a novel idea. For this, a thin layer of HfO_2 is placed on top of the electrode, only allowing the reaction to occur at the sides of the electrode. The benefit of this capping layer is that it reduces the amount of reactant lost to the bulk solution. Another benefit of this capping is the ability to generate a nanoelectrode structure without needing costly e-beam evaporation techniques for the fabrication. The advantage of nanoelectrodes is that the benefits of microelectrodes can be achieved to a greater extent, such as improved mass transport, charging currents, and solution resistance. This improvement has the potential of offering faster and more sensitive analysis and improved kinetic measurement of electrochemical processes.[1-4] The simulations carried out with a capping layer showed a 10.8x amplification in current compared to uncapped electrodes. Based on the simulations carried out a variety of IDE array designs were fabricated and subsequently electrochemically characterised in 1 mM ferrocene carboxylic acid in 10 mM phosphate buffer. While the electrochemical characterisation results showed the same trends as the simulations, increased performance for GC and capped electrodes, they also highlighted some limitation and effects that were not considered in the simulations. These will be discussed in more details herein.

2.2 Experimental

2.2.1 Finite Element Simulations

FCA concentration profiles at gold bands were simulated using COMSOL Multiphysics® 5.2. The objective of these simulations was to explore the optimum electrode geometry by examining the diffusional behaviour and the electrodes with varied electrode spacing, scan rate, and Generator-Collector designs. The simulations were based on the approach discussed in chapter 1. The models used replicated the conditions in 1 mM FCA in 10 mM PBS as described above. For the reversible electron transfer process of FCA/FCA+, it was assumed that the associated diffusion coefficient (5.4×10^{-6} cm^2 s^{-1})[4] of the oxidised and reduced forms soluble in solution are equal, i.e., the sum of the concentration of both species is constant over the diffusion space and is assumed equal to the sum of their bulk concentration. An experimentally determined value of 0.3 V (vs. Ag/AgCl, sat. KCl) was used for E^0, the formal potential of FCA/FCA^+. A simplified 2D model known as the diffusion domain approach was adopted. In this approach, each electrode band was modelled as a small rectangle with varying height and width located at the centre of a much larger rectangle (space domain). The space domain area was selected to be large enough to ensure bulk-like conditions at the external boundaries and they remained unaffected by the electrochemical processes occurring at the electrodes.

2.2.2 Electrode Design and Fabrication

The proposed design for the chips is illustrated in Figure 2.1. The chip dimensions were 1.5 x 1.5 cm, and consisted of 12 interdigitated electrode arrays, platinum counter and reference electrodes and 26 contact pads and tracks for these electrodes. The counter and reference electrodes, tracks and pads are highlighted in orange. The interdigitated

electrodes arrays, tracks and pads are highlighted in brown. Each of the arrays were 50 µm in length (or width) and 100 µm in width (or length), the specific geometries of these arrays such as electrode width and spacing was determined by the simulations discussed in 2.3.1. The circles on the schematic highlight the position of an o-ring, which is used in the electrochemical cell set-up to create a seal keeping the contact pads protected from the electrolyte solution.

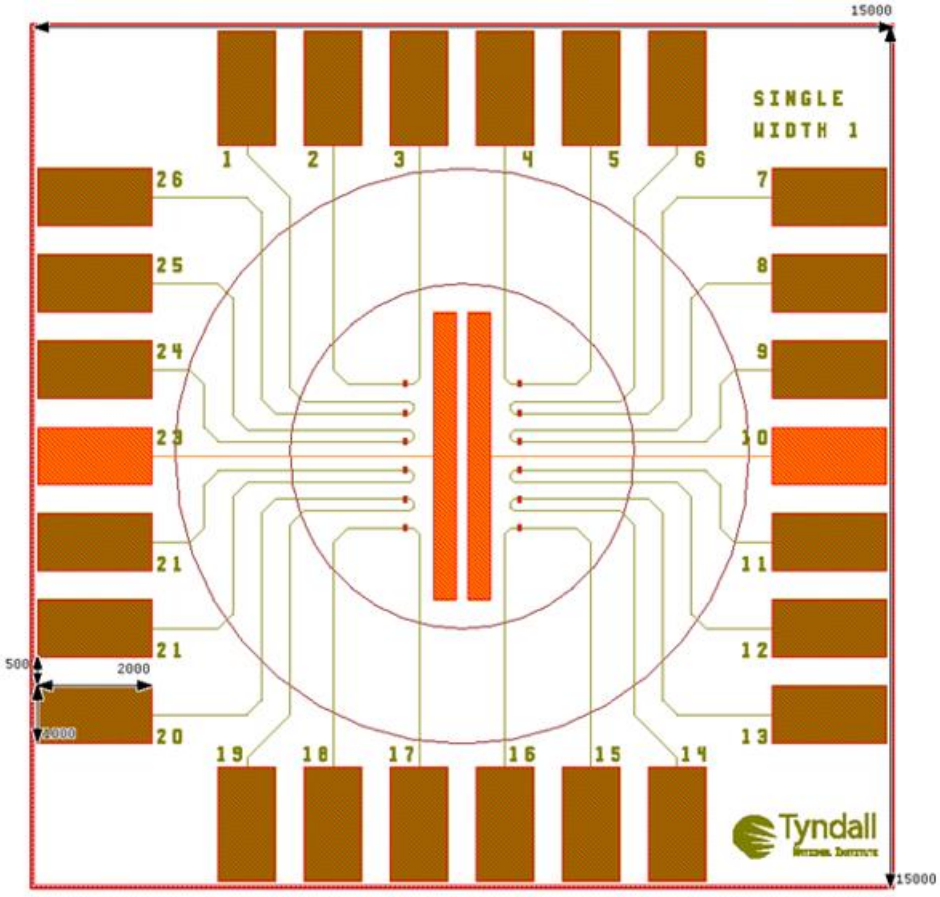


Figure 2.1 Mask design schematic for the chip fabrication process.

The specific array designs were chosen based on information gathered from simulations. The bulk of the chip design was decided on based on achieving the maximum number of arrays in the space available as well as allowing enough space for connection tracks and pads. As previously mentioned, the circles in Figure 2.1, highlight the o-ring, it is only within the inner o-ring circle that the chip is exposed to the electrolyte solution. Therefore,

the electrode arrays can only be placed in this location on the chip. Also required in this space are the reference and counter electrodes. As a result, the proposed design has two large platinum reference/counter electrodes in the centre surrounded by twelve electrode arrays with sufficient space on the chip for contact tracks to each of the arrays and the reference and counter electrode and contact pads that have sufficient spacing to be easily accessed by pins which will be discussed in a later section. The advantage of each electrode array having its own connection tracks and pads is that it allows the arrays to be used individually. An array can be used and once its functional lifetime has been reached, the next one can be used. Thus, greatly extending the functional lifetime of the chip over a single array chip.

The gold electrode bands were fabricated using photolithography processes on four-inch wafer silicon substrates with 1 µm layer of thermally grown silicon dioxide (Si/SiO_2) to avoid short circuiting in the metal layers. Spin-coating was used to deposit a layer of photoresist on the substrate which was then patterned with the designs highlighted in Figure 2.1. A titanium adhesion layer and gold were deposited into the pattern created by evaporation and the photoresist was lifted off. A silicon nitride (SiNx) passivation was deposited via low pressure chemical vapour deposition onto the wafer, this was then patterned and etched exposing the electrode and contact pads. An overview of this process is shown in Figure 2.2.

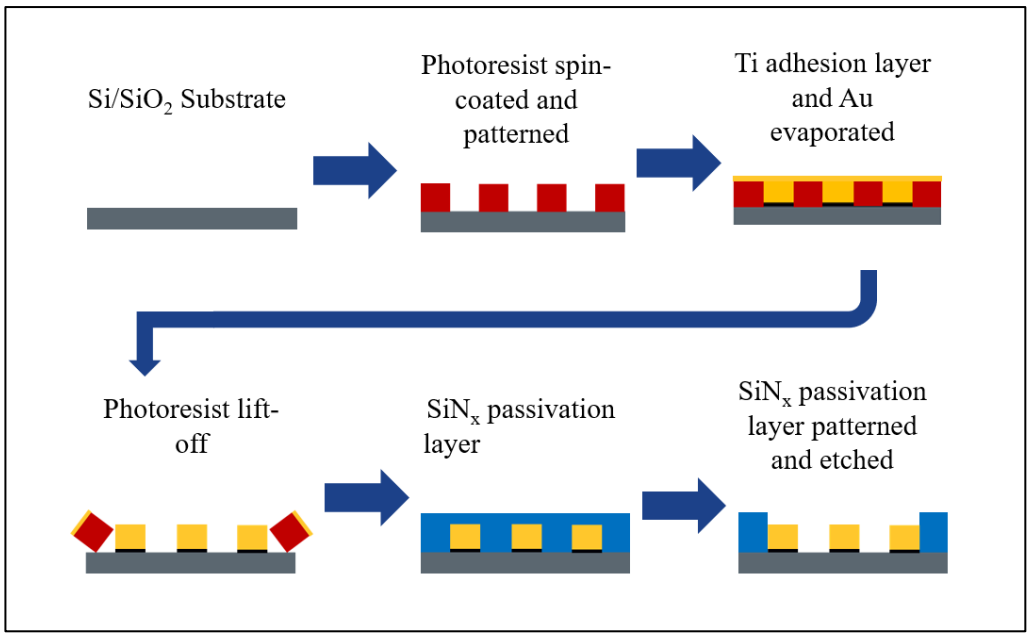


Figure 2.2 Process flow diagram for the fabrication of gold microbands using photolithographic techniques.

2.2.3 Electrochemical Cell Set-up

To allow both single and multiplexed electrochemical analysis, and to complete device packaging, chips were mounted into a custom-built chip holder that was designed and fabricated in-house. Electrical contact between the working, counter, and reference electrodes and the potentiostat was made through spring loaded probes. This contacted the on-chip peripheral pads and a connecting wire, enabling potentiostatic control of the device. The lower part of the holder was fabricated from a polytetrafluoroethylene (PTFE) base fixed to an aluminium tray onto which the chip was mounted. The tray into which the chip was placed was designed to only be ~0.1 mm larger than the chip edge dimensions to ensure that the chip would remain securely placed during the measurement. The PTFE cap comprised apertures to mount the spring-loaded probes and a central low volume sample reservoir, sealed from beneath with an O-ring (James Walker Ltd.), to accommodate the sample volume. The inner diameter (6 mm) of the O-ring was large enough to ensure that all electrodes on the chip had equivalent access to the analyte. The

spring-loaded probes (Connector Solutions Ltd., UK) had rounded tips 0.51 mm, (Series S Duraseal: S-00-J-1.3-G-DS-36-1), ensuring a good electrical contact with the contact pads (2 cm in length and 0.5 cm in width). When fully constructed, the cell was completely water-tight with a sample volume of ~100 µL. An image of the set-up can be seen in Figure 2.3.

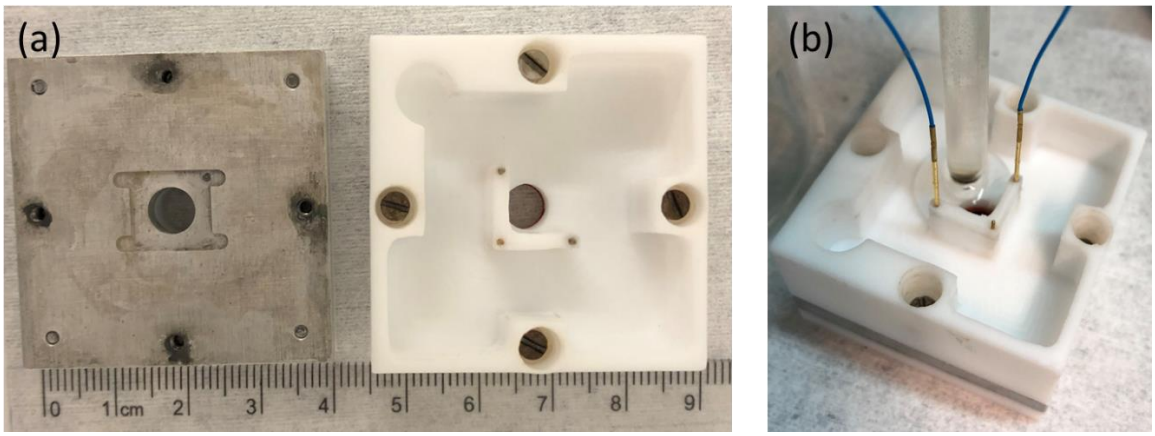


Figure 2.3 Image of a typical electrochemical cell set-up: (a) Cell components with measurements and (b) Cell in use with pins connecting to the working and counter electrodes and an external Ag/AgCl (sat. KCl) reference electrode

2.2.4 Microscopic Characterisation

Microscopic characterisation was undertaken using a calibrated microscope (Leitz, Eroglux) equipped with a camera, and a scanning electron microscope (Quanta FEG-SEM) operating at a beam voltage between 10 and 20 kV.

2.2.5 Electrochemical Characterisation

All electrochemical characterisation was performed using a CH760B Electrochemical Analyser and Faraday Cage CHI200B. Experiments were carried out in three- and four-electrode configurations using the gold Generator electrodes for three-electrode configuration and gold Collector electrodes as well for the four-electrode configuration with the on-chip platinum counter and an off-chip Ag/AgCl, sat. KCl reference electrode.

All measurements were carried out in the cell outlined in 2.2.3. Prior to electrochemical measurements, electrodes were cleaned by sequential immersion of chips for 10 minutes in acetone, iso-propyl alcohol (IPA), and DI water, followed by a thorough rinse with DI water and drying in a stream of filtered nitrogen. Cyclic voltammetry was undertaken in the range 0 to 0.6 V at a scan rate of 50 mV s^{-1} in 1 mM ferrocene monocarboxylic acid (FCA) in 10 mM phosphate buffered saline (PBS) solution (pH 7.4).

2.3 Results

2.3.1 Finite Element Simulations

2.3.1.1 *Varied Spacing Simulations*

The inter-electrode spacing, and interaction of electrodes is a key design feature for electrode arrays. Insufficient distance between electrodes can result in partial or complete overlap of the individual diffusion layers. This can lead to a reduction in current measured by the array due to the electrode acting as one large electrode equal to the total area of the array rather than individual microelectrodes. Simulations are used to establish the optimum inter-electrode spacing for the area. The following simulations were carried out using the procedures described in 2.2.1. Each of the electrodes were 2 µm in width and 50 nm in height, the scan rate was 50 mV/s and the spacing between the electrodes was varied from 1 to 100 µm. The resulting Comsol Multiphysics® simulations are shown in Figure 2.4. In the simulations the electrodes were swept from 0.0 V to 0.6 V, the point where the potential reaches 0.6 V, at t = 12 s, is captured in the diffusion profiles shown in Figure 2.4, and simulated diffusion profiles and current data used throughout this chapter. Figure 2.4 illustrates the space needed between electrodes in an array for them to be diffusionally independent of each other, which in this case is greater than 80 µm. The scale bar in this figure and subsequent figures in this section represents the concentration of the form of Fe in solution, where red is Fe^{2+} of the bulk solution and blue is the oxidised Fe^{3+} being generated at the electrode surface upon scanning to the appropriate potential.

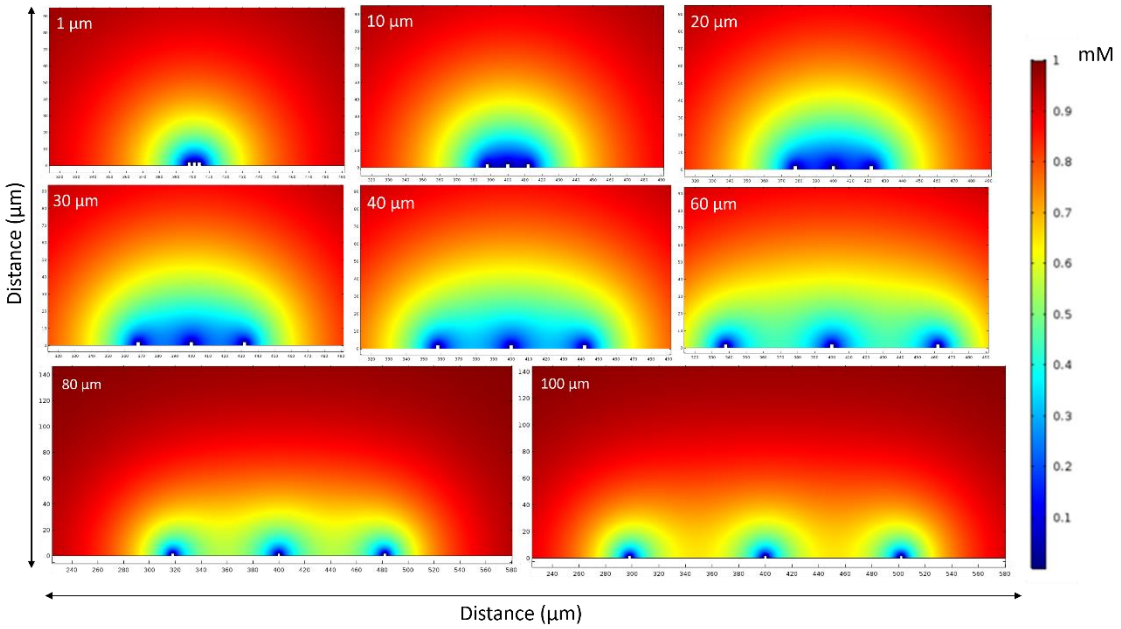


Figure 2.4 Cross-sectional view of 2D simulations of 1 mM FCA in 10 mM PBS diffusion profiles corresponding to CVs with 3 x 2 µm bands with varied inter-band spacing indicated in each tile. The images represent the condition at the end of a sweep to the potential 0.6 V vs Ag/AgCl (sat. KCl) at 50 mV s^{-1}. The scale bar on the right-hand side of the figure represents the concentrations of Fe^{2+} and Fe^{3+}, where 1 mM (red) is Fe^{2+} in the bulk solution and as it is oxidised at the electrode surface it is converted to Fe^{3+} (blue).

The observations made based on the diffusion profiles of the varied spacing between electrodes simulations are further backed up by simulated current values of the same geometric parameters. The plot in Figure 2.5, shows the simulated current values for each of the inter-electrode spacing examined. Here it can be seen that that current measured by the array increases with increasing inter-electrode spacing until it plateaus for 60, 80, and 100 µm where the simulated current values were 2.61, 2.67 and 2.70 nA, respectively. To establish what the expected current from a 3-electrode array with diffusionally independent electrodes is, the current of one band was simulated. The current of a single band was found to be 0.9 nA, therefore the ideal current for the 3-electrode diffusionally independent array is 2.7 nA. It can be seen from the current values highlighted above that this is achieved with a 100 µm inter-electrode gap. Other expectations that can be made of these proposed array designs is the resulting CV shape for this particular set-up where

the timescale for the CV is 24 s. In cases where the inter-electrode gap in 60 µm or above, the electrodes are spaced sufficiently apart that radial diffusion is predominant or fully achieved. Here, the response is steady-state and time independent, therefore a sigmoidal shaped CV curve is expected. Where the inter-electrode gap is below 60 µm, the inter-electrode gap is insufficient to avoid diffusion layer overlap leading to planar diffusion becoming the dominant effect. For planar diffusion, the response is diffusion-limited and time-dependent, resulting in a peaked CV curve.

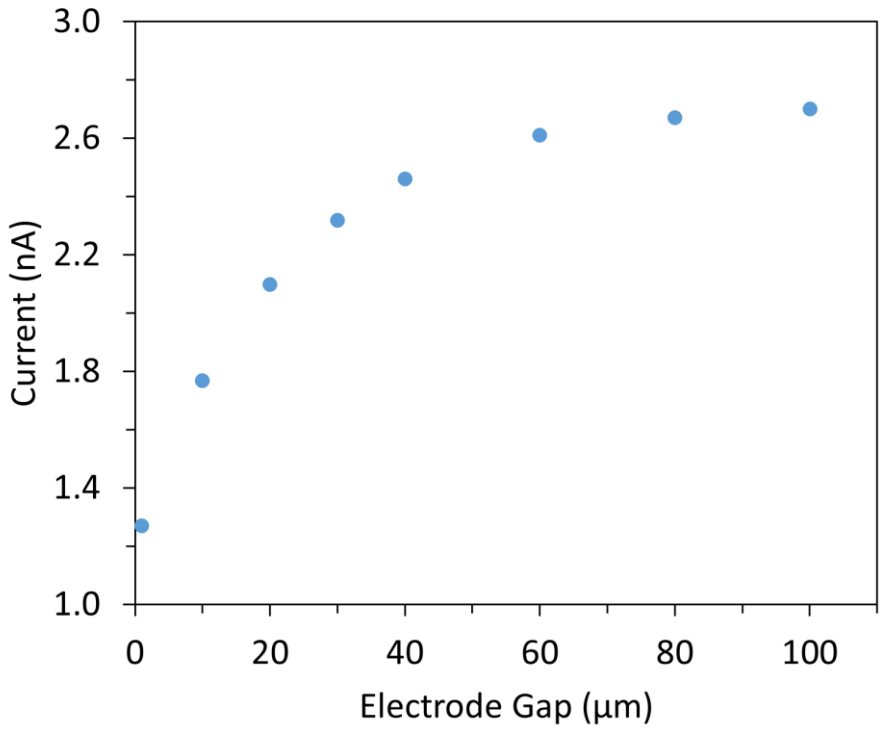


Figure 2.5 Plot of simulated current values for 2 µm band 3 electrode arrays with varied inter-electrode gap. Simulated current data point were taken from the limiting current of simulated CVs swept from 0 V to 0.6 V vs Ag/AgCl (sat. KCl) at 50 mV s^{-1}.

2.3.1.2 *Varied Scan Rate Simulations*

As well as inter-electrode spacing, scan rate can also be used to control diffusion overlap. By varying the scan rate, the size of the diffusion layers that form during the experiment can be controlled. For potential sweep experiments, scan rate directly affects the mass

transport of the system. Faster scan rates lead to a decreasing diffusion layer thickness,[5] which means that a smaller band separation can be tolerated, and the magnitude of overlap is reduced. However, faster scan rates are not ideal as the response generated is not steady state. At slower scan rates, the "shielding effect" can be induced due to overlapping diffusion fields. Therefore, slower scan rates require a larger band separation or less densely packed array.[6-9]

The following simulations were carried out using the procedures described in 2.2.5. Each of the electrodes were 2 µm in width and 50 nm in height and 100 µm apart. Three scan rates were investigated: 1, 10, and 100 mV s^{-1}. The resulting Comsol Multiphysics® simulations are shown in Figure 2.6. This simulation shows the impact of scan rate on diffusion at the electrodes. Faster scan rates reduce the growth of the diffusion profile at the electrode surface thus minimising but not entirely eliminating any diffusion overlap, resulting to the improved performance of the array. Slower scan rates give diffusion layers more time to grow and can cause them to overlap even at large electrode gaps such as 100 µm; leading to a reduction in the sensor performance. The observations made based on the simulated diffusion layer profiles are backed up by simulated current data which gave current values of 1.48, 2.14 and 2.93 nA for 1, 10, and 100 mV s^{-1}, respectively.

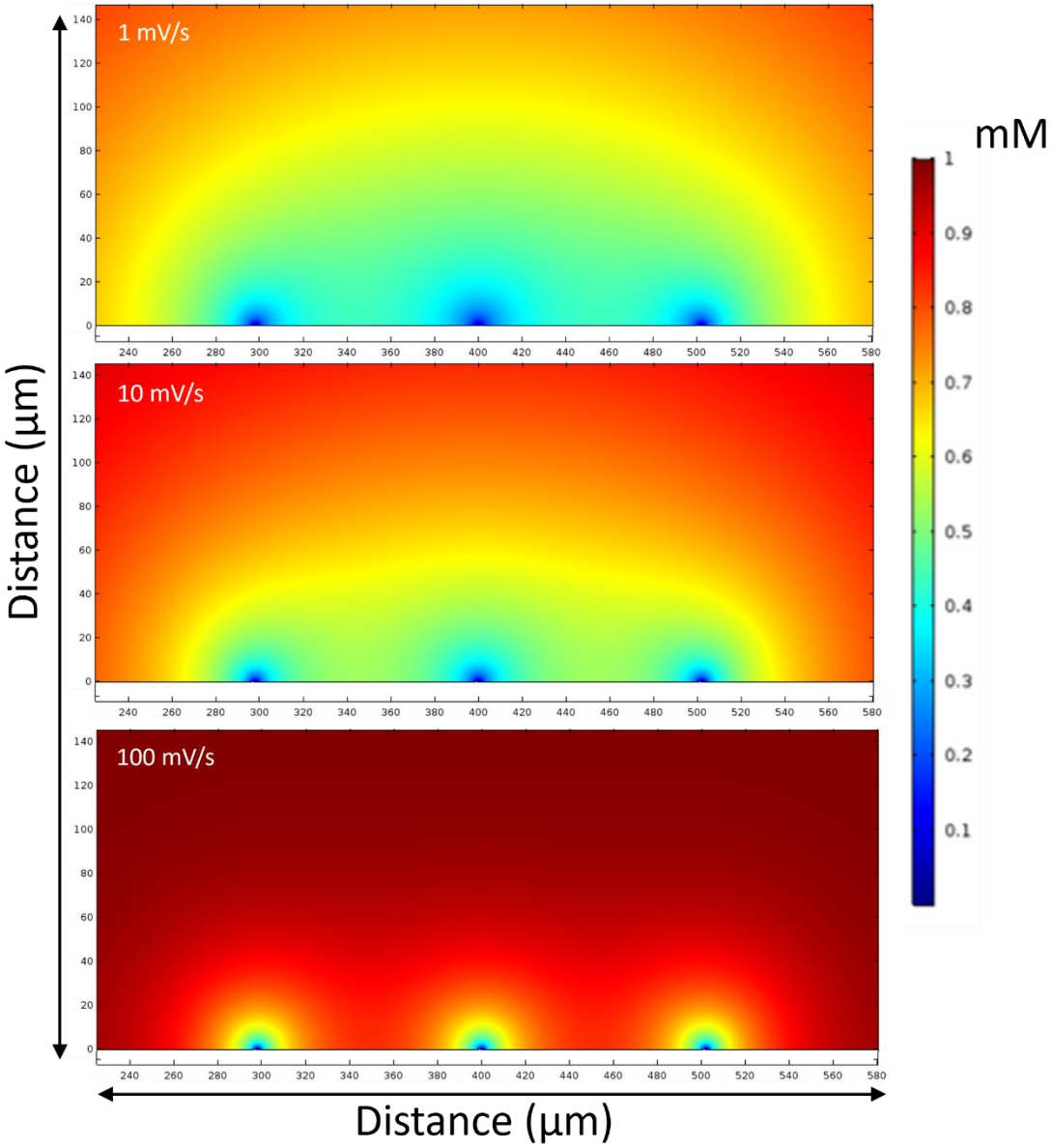


Figure 2.6 Cross-sectional view of 2D simulations of 1 mM FCA in 10 mM PBS diffusion profiles corresponding to CVs with 3 x 2 µm bands with 100 µm inter-electrode spacing. The images represent the condition at the end of a sweep to the potential 0.6 V vs Ag/AgCl (sat. KCl) at varied scan rates of 1, 10, and 100 mV s^{-1} as indicated on each tile. The scale bar on the right hand side of the figure represents the concentrations of Fe^{2+} and Fe^{3+}, where 1 mM (red) is Fe^{2+} in the bulk solution and as it is oxidised at the electrode surface it is converted to Fe^{3+} (blue).

2.3.1.3 *Varied Electrode Height Simulations*

Using the same parameters as the previous simulation, the effect of electrode height was also investigated. Here the electrode height was varied from 50 nm to 1 µm. A sample of the resulting simulated diffusion layer profiles can be seen in Figure 2.7. Here it can be seen that as the electrode height is increased, the blue area of the diffusion layer which indicates where Fe^{2+} has been oxidised to Fe^{3+}. This increase in the amount of Fe^{3+} being formed at the electrode surface is expected to correspond to an increase in the current output of the array.

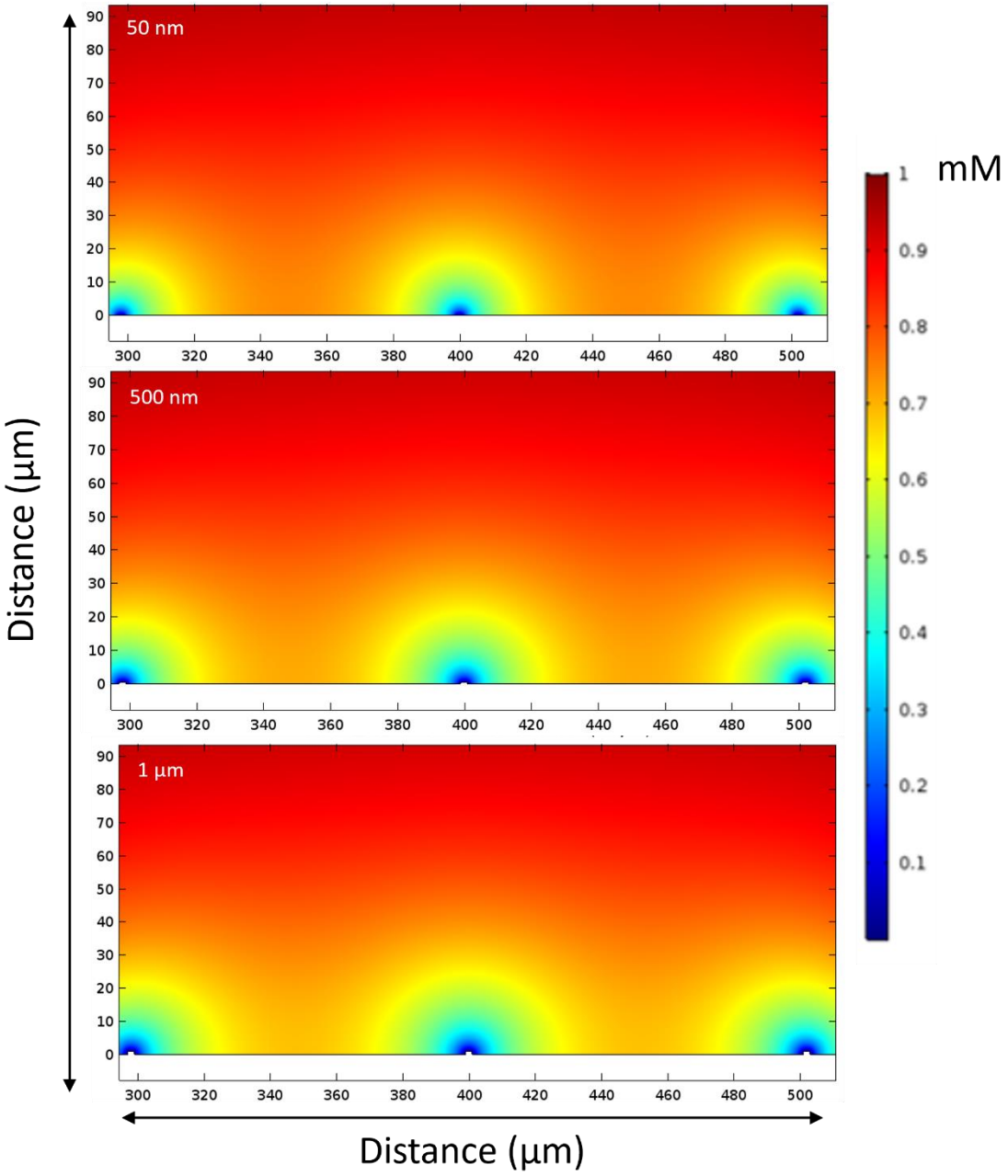


Figure 2.7 Cross-sectional view of 2D simulations of 1 mM FCA in 10 mM PBS diffusion profiles corresponding to CVs with 3 x 2 µm bands with 100 µm inter-electrode spacing and varied electrode height, as indicated on the tiles. The images represent the condition at the end of a sweep to the potential 0.6 V vs Ag/AgCl (sat. KCl) at varied scan rates of 1, 10, and 100 mV s^{-1} as indicated on each tile. The scale bar on the right hand side of the figure represents the concentrations of Fe^{2+} and Fe^{3+}, where 1 mM (red) is Fe^{2+} in the bulk solution and as it is oxidised at the electrode surface it is converted to Fe^{3+} (blue).

The expected increase in the array current with increasing electrode height is further backed up by the simulated limiting current data, as can be seen in Figure 2.8. Here it can be seen that the limiting current of the array increases linearly with electrode height. This result is expected based on the Randles-Sevcik equation[10] where the resulting current is directly proportional to electrode area.

$$i_p = (2.69 \times 10^5) n^{\frac{3}{2}} A C D^{\frac{1}{2}} v^{\frac{1}{2}} \quad 2.1$$

where *n* is the number of electrons, *A* the electrode area (cm^2), *C* the concentration (mol cm^{-3}), D the diffusion coefficient ($cm^2\ s^{-1}$), and ν the potential scan rate ($V\ s^{-1}$). However, the data is not perfectly linear in Figure 2.8 as only the height was taken into consideration here. Electrode height also plays a key role in the redox cycling of IDE arrays which will be discussed in the next section.

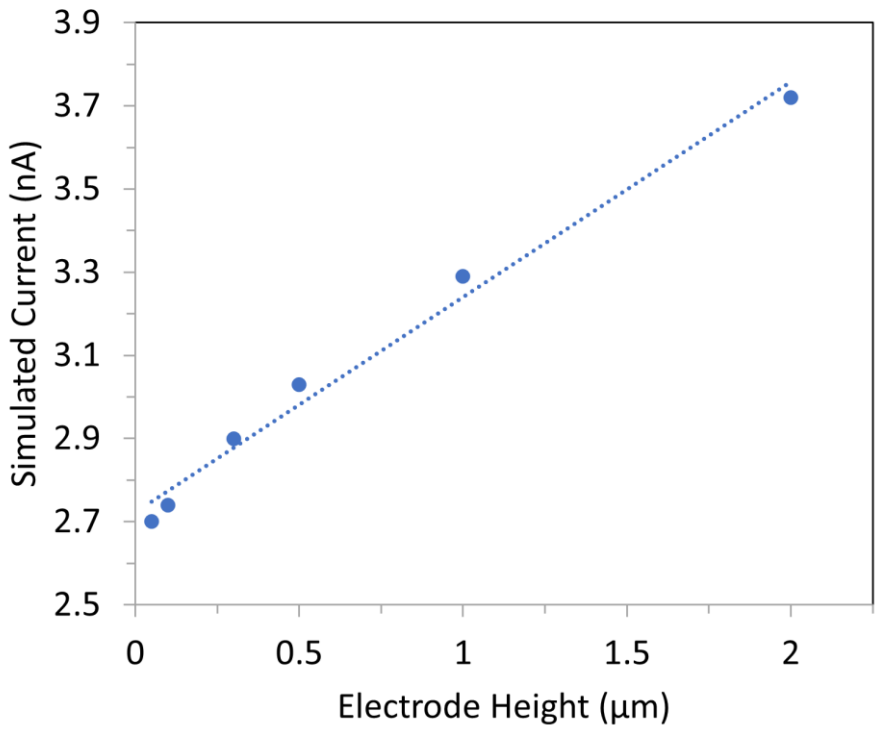


Figure 2.8 Plot of simulated limiting current for various electrode height of 2 µm bands in an array with 100 µm inter-electrode gaps. Simulated current data point were taken from the limiting current of simulated CVs swept from 0 V to 0.6 V vs Ag/AgCl (sat. KCl) at 50 mV s^{-1}.

2.3.1.4 *Generator-Collector Simulations*

A simulation of GC electrodes is shown in Figure 2.9. Here, (a) shows an IDE array where the collector electrode is left unconnected, i.e., "Non-GC Mode" and (b) where the collector electrode is held at 0.1 V during the CV where Fe3+ is converted back to Fe2+, i.e., "GC Mode". In Non-GC Mode, the Fe^{2+} in the FCA represented by red in the simulation outputs is being oxidised to Fe^{3+} represented by blue when the FCA is completely converted to Fe3+ or the intermediate colours for partial conversion. Because the electrodes are spaced close together the blue areas or Fe^{3+} being produced are overlapping. This causes the electrodes to act as one large electrode rather than individual microelectrodes, thus reducing the sensitivity and limit of detection of the electrodes. In the GC Mode, the reverse reaction is occurring at the collector, the Fe^{3+} is being reduced back to Fe^{2+}. This creates a barrier effect between the generator electrodes preventing the

Fe^{3+} diffusion layers from overlapping with each other. As a result, the electrodes can be spaced closer together while maintaining diffusional independence. Using GC mode analysis, the spacing between bands can be reduced from ~60 µm to 1 µm. Reducing the sensor footprint has many practical benefits. Less material is required to fabricate the sensors thus lowering the cost of production. Additionally, the increased amount of Fe^{2+} available for oxidation at the Generator increases the current output of the array, i.e., redox cycling occurs. The benefit of the Collector electrode is highlighted in Figure 2.9, an array of 2 µm wide electrode with a 2 µm inter-electrode gap where (a) the Collector electrode was left disconnected, Non GC Mode, and (b) the Collector was held at 0.1 V, GC Mode It can be seen here that the use of the Collector in (b) prevents the complete overlap of the blue diffusion layers which is seen in (a). It can be estimated based on the simulated diffusion profiles in Figure 2.9 that in non-GC mode, (a), the expected CV response would be peak shaped because of the diffusion-limited, time-dependent behaviour caused by the overlapping diffusion layers. For GC mode, (b), it is expected that the CV response would be a steady-state sigmoidal curve.

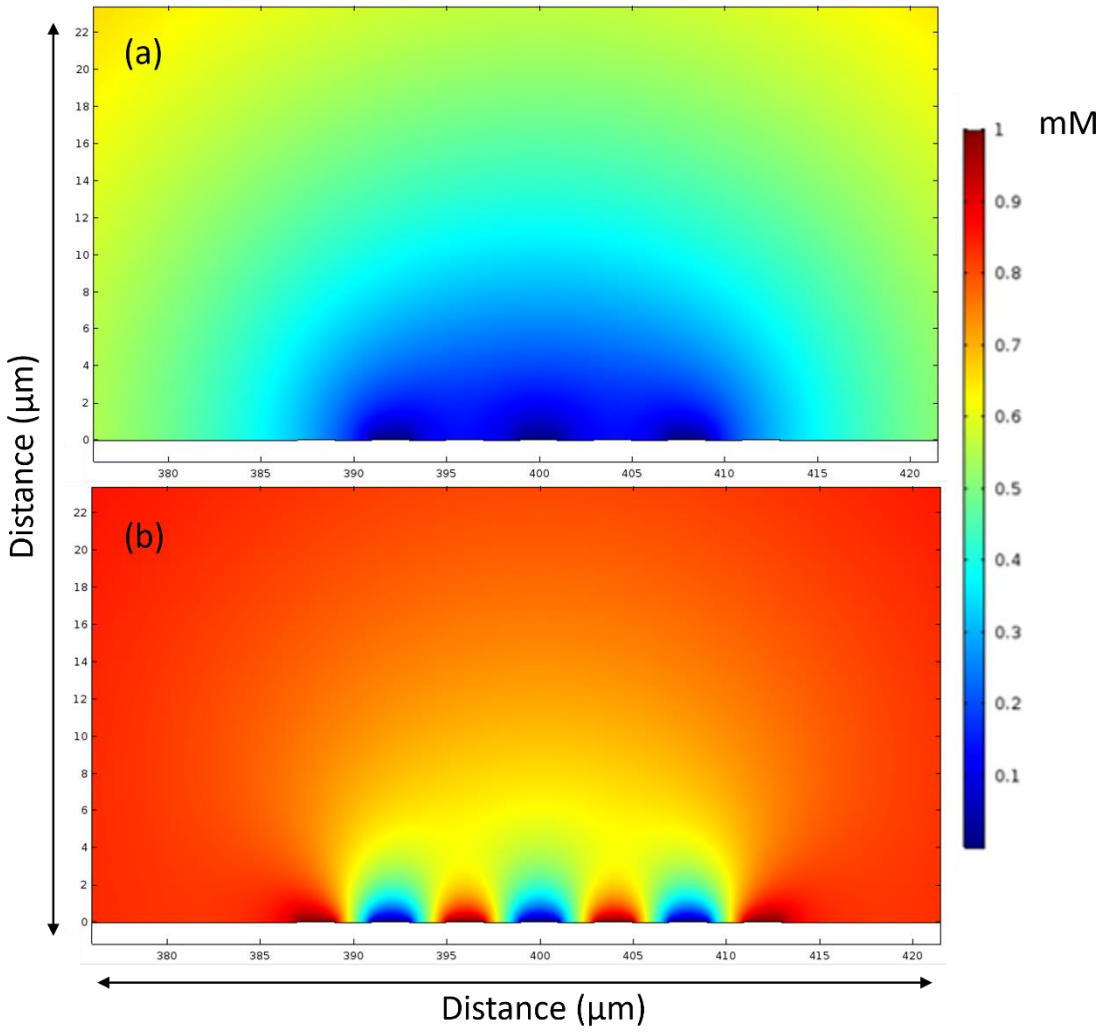


Figure 2.9 Cross-sectional view of 2D simulations of 1 mM FCA in 10 mM PBS diffusion profiles corresponding to CVs in (a) non GC mode where the generator electrode was swept from 0.0 V to 0.6 V while the collector electrode was unconnected and (b) GC mode where the generator was swept from 0.0 V to 0.6 V vs Ag/AgCl (sat. KCl) at 50 mV s^{-1} while the collector was held at 0.1 V vs Ag/AgCl (sat. KCl). The images represent the condition at the end of a sweep to the potential 0.6 V vs Ag/AgCl (sat. KCl). The scale bar on the right hand side of the figure represents the concentrations of Fe^{2+} and Fe^{3+}, where 1 mM (red) is Fe^{2+} in the bulk solution and as it is oxidised at the electrode surface it is converted to Fe^{3+} (blue).

The simulated CV responses for (a) Non GC Mode and (b) GC Mode show that the curves obtained are as predicted from observing the simulated diffusion profiles. The simulated CV responses are shown in Figure 2.10. Here it can be seen that (a) leads to a peaked curve response while (b) leads to a steady-state sigmoidal curve response. Figure 2.10 (b) also highlights the Collector response. As mentioned above, the opposite reaction to the Generator electrode occurs at the Collector, i.e., Fe^{2+} is being oxidised to Fe^{3+} at the Generator and at the Collector the Fe^{3+} produced by the Generator is being reduced back to Fe^{2+}. Therefore, the opposite CV curve is recorded by the Collector as is seen here. The simulated currents for the Generator electrodes showed an increase from (a) 4.36 nA to (b) 18.9 nA when switching from non-GC mode to GC mode, a 4.3x current amplification.

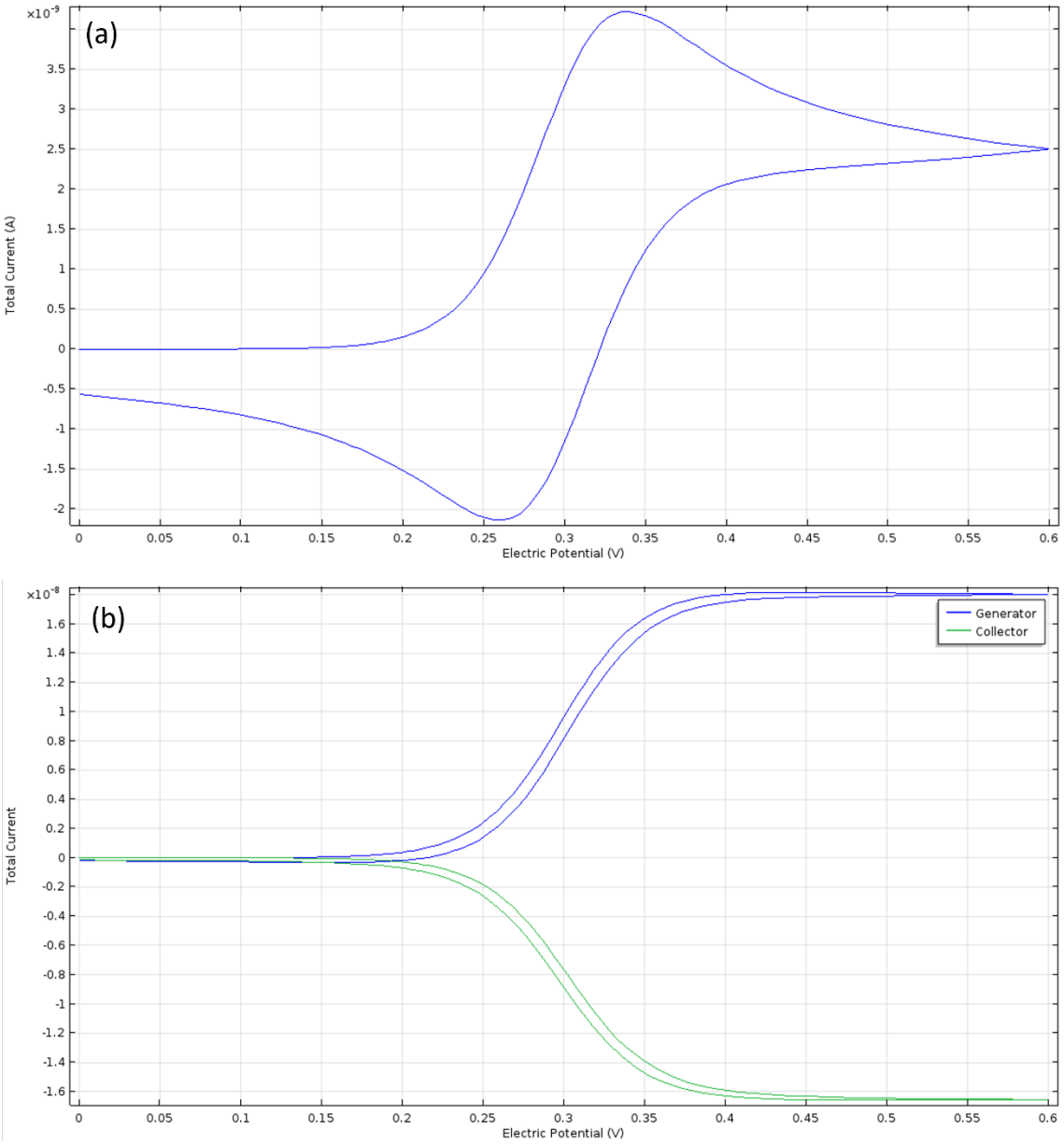


Figure 2.10 Simulated CV for 1 mM FCA from 0 to 0.6 V vs Ag/AgCl (sat. KCl) at 50 mV s^{-1} for 2 µm bands with 2 µm inter-electrode gaps for (a) the Collector left unconnected as the Generator was swept from 0.0 to 0.6 V vs Ag/AgCl (sat. KCl), Non GC Mode, and (b) the Collector was held at 0.1 V vs Ag/AgCl (sat. KCl) while the Generator was swept from 0.0 to 0.6 V vs Ag/AgCl (sat. KCl), GC Mode.

Several electrode array designs for GC electrodes were proposed with varying electrode widths (1, 2, and 5 µm) and inter-electrode gaps (1, 2, and 5 µm). A summary of the expected performance of these electrodes based on simulated currents is summarised in Table 2.1. This simulated data indicates that smaller electrodes, 1 and 2 µm bands, with smaller inter-electrode gaps, 1 and 2 µm inter-electrode gaps, will be the most efficient array designs with 1 µm bands with a 1 µm inter-electrode gap (1x1) expected to be best. As the inter-electrode gap increases to 5 µm, a larger electrode width of 2 µm to 5 µm is expected to achieve higher sensitivity and collection efficiency to 1 µm bands. This trend is consistent with studies in literature by Aoki et. al and Baeumner et. al which highlight the effect of array dimensions on the collection efficiency.[11, 12] Also incorporated in the designs is a single 1 µm band, the simulated current of which is expected to be 0.8 nA. An alternative method for calculating the expected current output from an array current is to multiply the current of a single band by the number of bands in the array. By this method, the expected currents for 1 µm band with 1 µm inter-electrode gap (1x1), the 1 µm band with 2 µm inter-electrode gap (1x2), and 1 µm band with 5 µm inter-electrode gap (1x5) would be 20, 13.6, and 7.2 nA, respectively. However, these values are not in agreement with those highlighted in Table 2.1. In non-GC mode, the simulated currents are greatly reduced compared to the estimate based on the single band current. The reason for this is that when the bands are operated in non-GC mode the diffusion layers overlap as highlighted in Figure 2.9(a). This demonstrates the "shielding effect" described earlier, which leads to a reduction in the current measured. In GC mode, the opposite is seen where the simulated current is higher than that calculated by the single band current. This is because of redox cycling that leads to an increase in the current output of the array. This effect is not considered using the single band current method.

Table 2.1 Summary of simulated current and expected collection efficiencies (N) values for proposed electrode array designs.

Design **Electrode width x gap**	Non-GC Current	GC Current		Collection Efficiency
		Generator	Collector	
[µm]	[nA]	[nA]	[nA]	[%]
1	0.8	-	-	-
1x1	4.4	39.0	-37.7	97
1x2	4.3	20.2	-19	95
1x5	3.8	8.0	-6.4	80
2x1	4.5	32.1	-30.1	94
2x2	4.4	18.9	-17.3	92
2x5	4.0	8.6	-6.9	81
5x1	4.1	20.2	-18.8	93
5x2	4.1	14.8	-12.7	86
5x5	3.7	7.2	-6.1	85

In addition to band width and inter-electrode gap, electrode height can also have an impact on the array performance. Taking the design of 2 µm bands with 2 µm inter-electrode gap (2x2) for example, when the electrode height is increased from 50 nm to 300 nm, the Generator current increases to 23.4 nA from 18.9 nA and the collection efficiency also increases to 93% from 92%. Unlike increasing the band width where the increases in surface area is negated by the increased loss of reactant to the bulk solution, the increased surface area created by height does not result in increased loss of reactants to the bulk solution. Therefore increasing the electrode height can lead to increased current output and collection efficiency.[12] Other design considerations for increasing collection efficiency were also investigated such as increasing the height of the collector electrodes. Increasing the height of the collector electrodes would increase the collection efficiency

as less species produced at the generator can escape to the bulk, as it is trapped by the collector electrodes. These results are highlighted in Figure 2.11, where the collector height is increased from 100 nm to 500 nm and finally 1 µm. As the collector height increases the orange area of the generator electrode decreases. The orange area is representative of the Fe^{3+} generated at the electrode surface being lost to the bulk solution. This is due to the collector confining more of the analyte at the generator which increases the amount available for reaction thus, increasing the collection efficiency. These observations are backed up by the simulated current data where the current from the Generator when the Collector height is the same (50 nm) is 18.9 nA and increases to 19, 21.5 and 23.7 nA as the Collector height is increased to 100, 500, and 1 µm, respectively, while the Generator remains at 50 nm. Increased collection efficiencies of 92% for 50 nm and 100 nm, 94% for 500 nm, and 95 % for 1 µm were also observed.

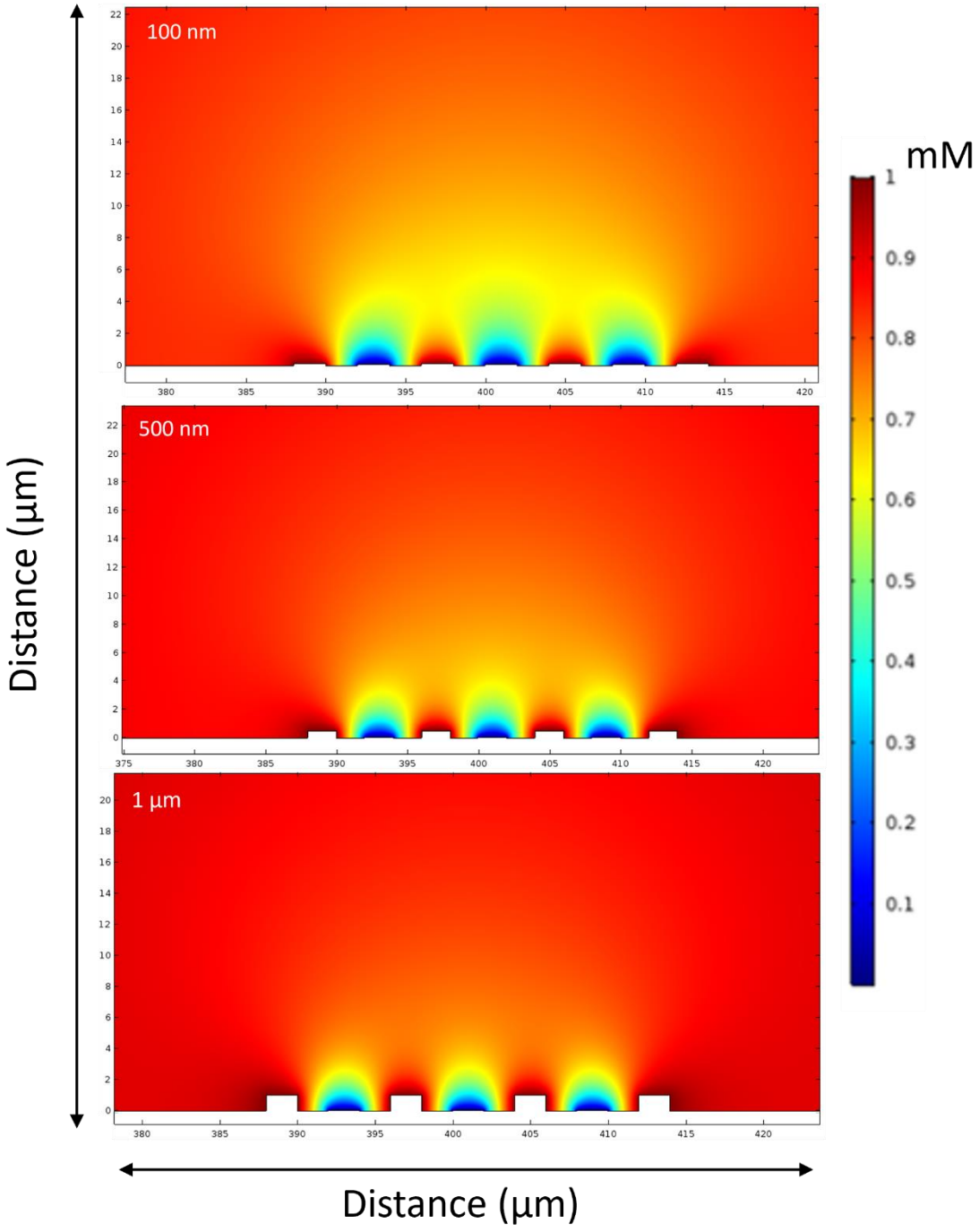


Figure 2.11 Cross-sectional view of 2D simulations of 1 mM FCA in 10 mM PBS diffusion profiles corresponding to CVs in GC mode with three 2 µm bands generator electrodes 50 nm in height and four 2 µm collector electrode with varied height as indicated on the individual tiles. The images represent the condition at the end of a sweep to the potential 0.6 V vs Ag/AgCl (sat. KCl) at 50 mV s^{-1}. The scale bar on the right hand side of the figure represents the concentrations of Fe^{2+} and Fe^{3+}, where 1 mM (red) is Fe^{2+} in the bulk solution and as it is oxidised at the electrode surface it is converted to Fe^{3+} (blue).

The final design feature investigated for increasing collection efficiency was the introduction of a capping layer on the electrodes, as highlighted by the blue lines on top of the electrodes in Figure 2.12(b). These capping layers on top of the electrodes were formed using an insulating HfO_2 layer on the gold electrodes. HfO_2 was chosen above other capping layer options such SiO_2 due to higher dielectric constant for the HfO_2 enabling thinner insulating films and the unreliability with respect to processing of SiO_2 thin films.[13] Capping the electrodes limits the reacting surface to the electrode sidewalls and greatly reduces the amount of the reaction being lost to the bulk solution from the top surface of the electrode which is significantly larger in area than the sidewalls, further increasing sensor performance. Uncapped and capped electrodes in GC mode are compared in Figure 2.12. Here it can be seen that the $Fe3^+$ rich area represented by blue, is greatly decreased and localised at the sidewalls for the capped electrodes (b) compared to the uncapped electrodes (a). This indicated a decrease in the loss of reactant to the bulk solution thus improving the current output and collection efficiencies. The simulated currents for these electrodes were normalised to the surface area to consider the capped electrode being 21 times smaller than the uncapped electrodes. The resulting data gave a current of 2.77 mA cm^{-2} for uncapped electrodes and 30 mA cm^{-2} for capped electrodes, a 10.8 current amplification for capped electrodes over uncapped electrodes.

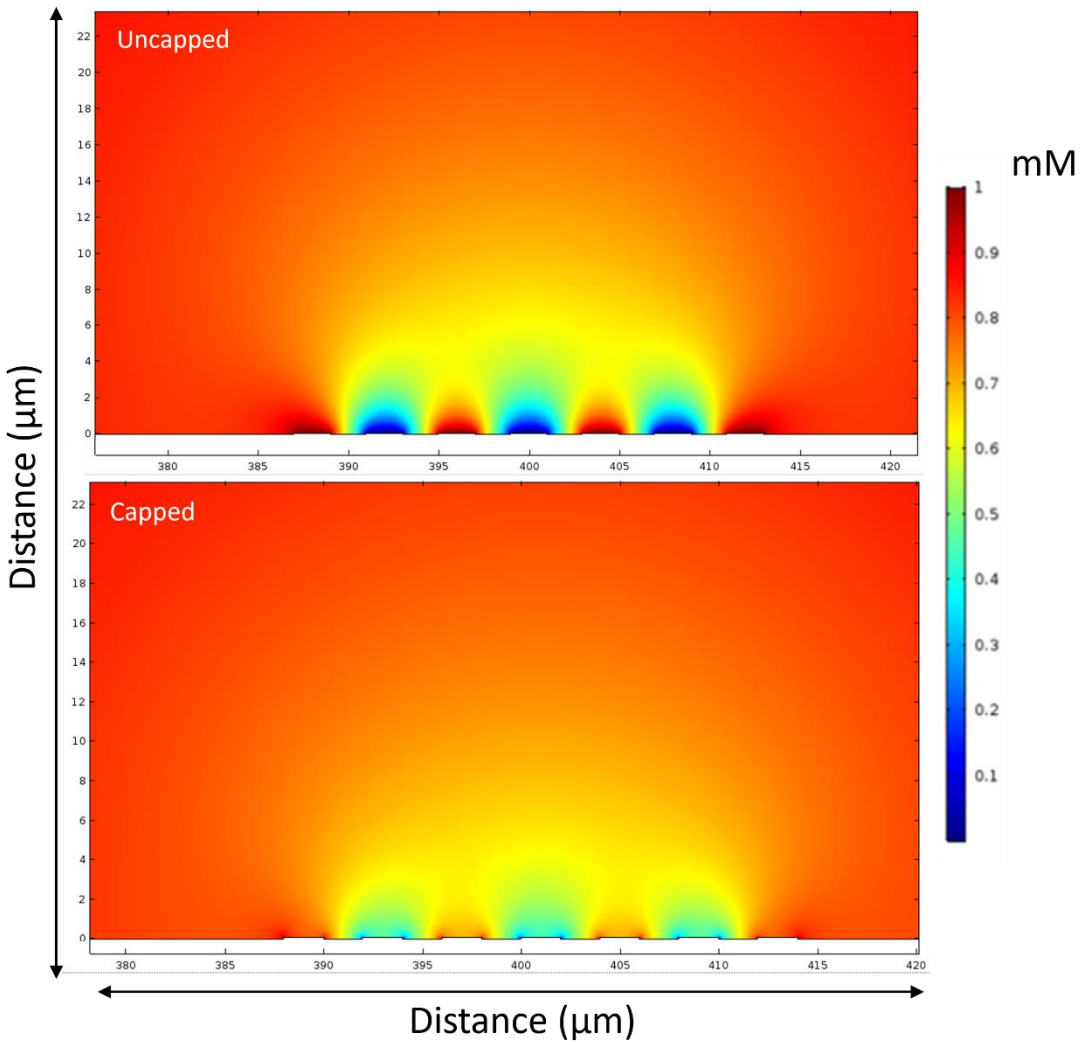


Figure 2.12 Cross-sectional view of 2D simulations 1 mM FCA in 10 mM PBS diffusion profiles corresponding to CVs when the potential at the generator electrode was swept from 0.0 V to 0.6 V vs Ag/AgCl (sat. KCl) at 50 mV s^{-1} while the collector was held at 0.1 V vs Ag/AgCl (sat. KCl) for uncapped and capped electrodes, as indicated on the tiles. The images represent the condition at the end of a sweep to the potential 0.6 V vs Ag/AgCl (sat. KCl). The scale bar on the right-hand side of the figure represents the concentrations of Fe^{2+} and Fe^{3+}, where 1 mM (red) is Fe^{2+} in the bulk solution and as it is oxidised at the electrode surface it is converted to Fe^{3+} (blue).

2.3.1.5 *Finite Element Simulation Summary*

The ability to simulate the performance of IDE arrays is key in establishing to optimum geometry of the arrays. With the help of simulated current responses above it was established that for non-IDE designs or IDE arrays where the Collector electrode was not used; the spacing between the electrodes needed to be 60 µm or more for the electrodes to be diffusionally independent of each other. In cases where the Collector was used in the IDE arrays, smaller electrode widths and inter-electrode gaps were established as optimum. Several designs were put forward for fabrication with various electrode widths of 1, 2, and 5 µm, and various inter-electrode gaps of 1, 2, and 5 µm. A single 1 µm band was also included in the design. It was shown that the performance of these IDE arrays could be further enhanced by the simple addition of an HfO_2 capping layer which is estimated to give ~10.8 times current amplification over uncapped electrodes.

2.3.2 Microscopic Characterisation

Following fabrication, analysis using a scanning electron microscope was undertaken to characterise the newly fabricated interdigitated arrays. Figure 2.13 shows a top view of the nine array designs. The bands and spacing of each array were measured and found to agree with the specified dimensions. The measurements for each design can be found in Table 2.2. The overall the average deviation for all designs was found to be 0.061 µm.

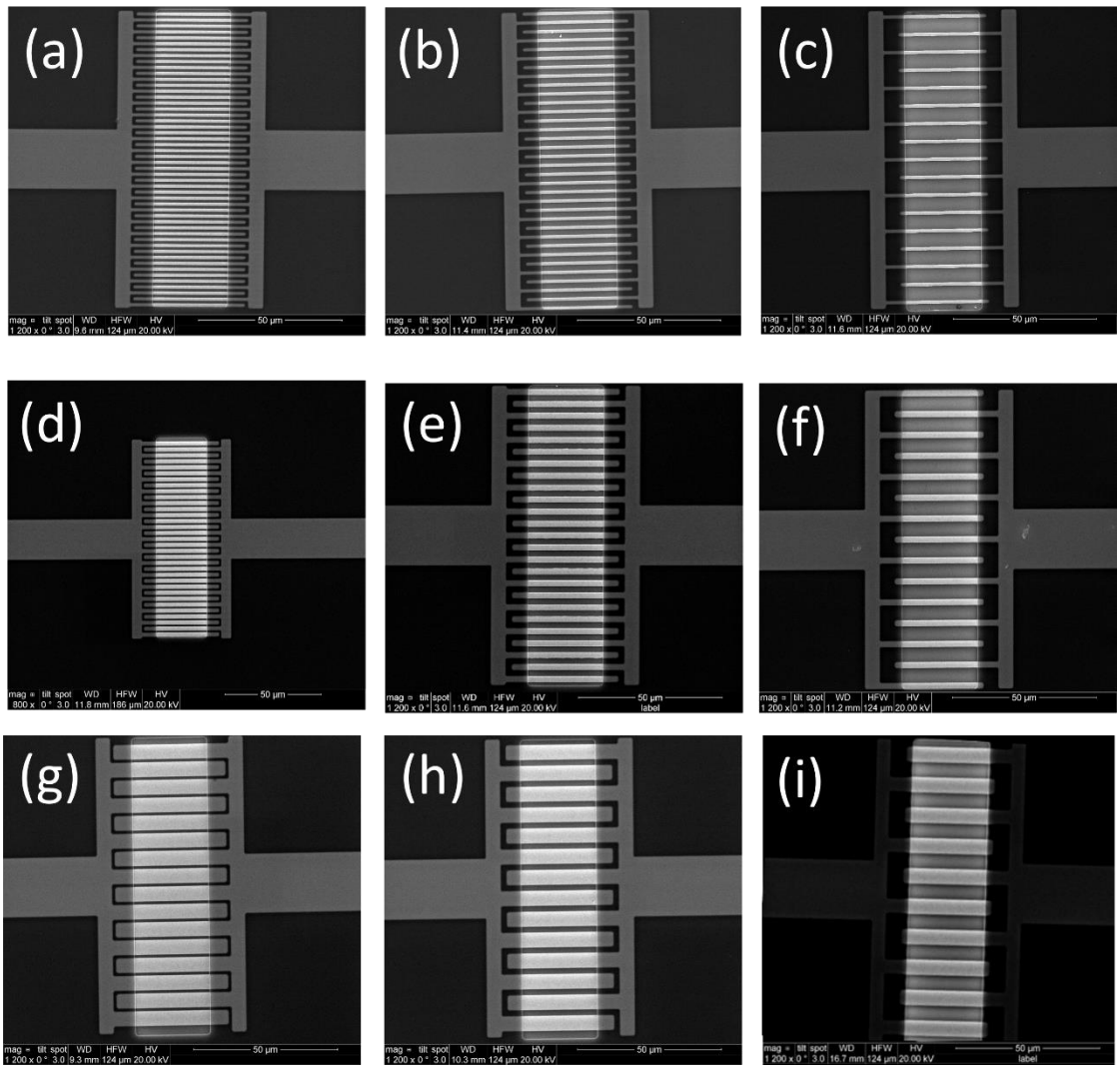


Figure 2.13 SEM of each array design; 1 µm bands with 1 µm (a), 2 µm (b) and 5 µm (c) spacing, 2 µm bands with 1 µm (d), 2 µm (e) and 5 µm (f) spacing, and 5 µm bands with 1 µm (g), 2 µm (h) and 5 µm (i) spacing.

Table 2.2 Average widths for electrode width and inter-electrode gap for the various IDE designs.

Design **electrode width × gap**		**Width**	**Deviation**
[µm]		[µm]	[µm]
1x1	Band	0.99	0.024
	Gap	1.05	0.024
1x2	Band	1.09	0.020
	Gap	2.10	0.003
1x5	Band	1.08	0.025
	Gap	5.31	0.063
2x1	Band	2.14	0.075
	Gap	1.00	0.091
2x2	Band	2.12	0.027
	Gap	2.04	0.047
2x5	Band	1.98	0.116
	Gap	5.02	0.058
5x1	Band	5.05	0.069
	Gap	1.12	0.137
5x2	Band	5.06	0.058
	Gap	2.07	0.002
5x5	Band	5.06	0.067
	Gap	5.13	0.291

2.3.3 Electrochemical Characterisation

2.3.3.1 *Uncapped Electrodes*

Electrochemical measurements were carried out as described in sections 2.2.3 and 2.2.5, with the additional step of the collector electrode being held at 0.1 V while the Generator electrode is swept from 0.0 V to 0.6 V for GC Mode. Where the collector was not used is referred to as Non GC Mode. In the simulated data an improvement in performance of GC Mode over Non GC Mode was observed. This is also seen in the experimental characterisation of the fabricated arrays and can been seen in Figure 2.14. For each array design tested, an increase in the limiting current achieved was seen. Additionally, the shape of the resulting cyclic voltammograms matches the predictions based in the simulated data. For Non GC Mode, the curve is peak shaped as was predicted by the overlapping of the diffusion layers of each band. For GC Mode, a steady-state sigmoidal curve is achieved due to the Collector electrode interrupting the overlapping diffusion layers of the Generator electrodes.

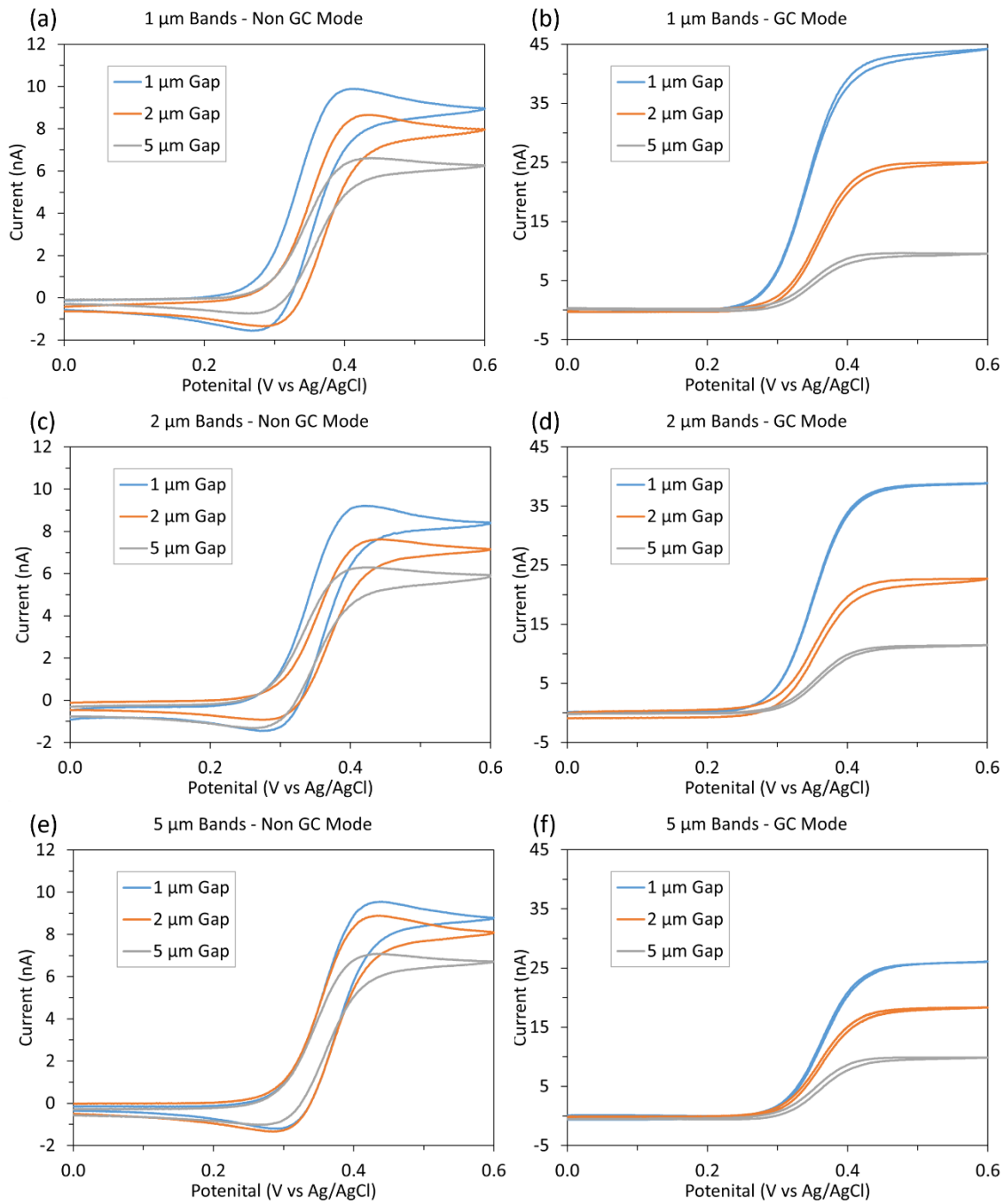


Figure 2.14 Typical cyclic voltammetric response of 1 mM FCA in 10 mM phosphate buffer from 0.0 to 0.60 V vs Ag/AgCl (sat. KCl) at 50 mV s^{-1} for (a) 1 µm bands with a 1 µm, 2 µm, and 5 µm gap in Non GC mode, (b) 1 µm bands with a 1, 2 and 5 µm gap in GC Mode, (c) 2 µm bands with a 1, 2 and 5 µm gap in Non GC mode, (d) 2 µm bands with a 1, 2 and 5 µm gap in GC Mode, (e) 5 µm bands with a 1, 2, and 5 µm gap in Non GC mode, (f) 5 µm bands with a 1, 2 and 5 µm gap in GC Mode.

In Figure 2.14(b), it was seen that the oxidation potential for ferrocene occurs at a lower potential for the 1 µm electrode bands with a 1 µm inter-electrode gap. A possible explanation for this phenomenon is that there is a larger number of bands in the 1 µm band with 1 µm interelectrode design making it more favourable for the reaction to occur. As the number of electrodes reduces the oxidation potential of the ferrocene increases. This effect can be seen in Figure 2.15, where the 1 µm gap designs have been plotted together. Here it can be seen that as the electrode band width increases which subsequently reduces the number of bands in the array, the oxidation potential for ferrocene increases.

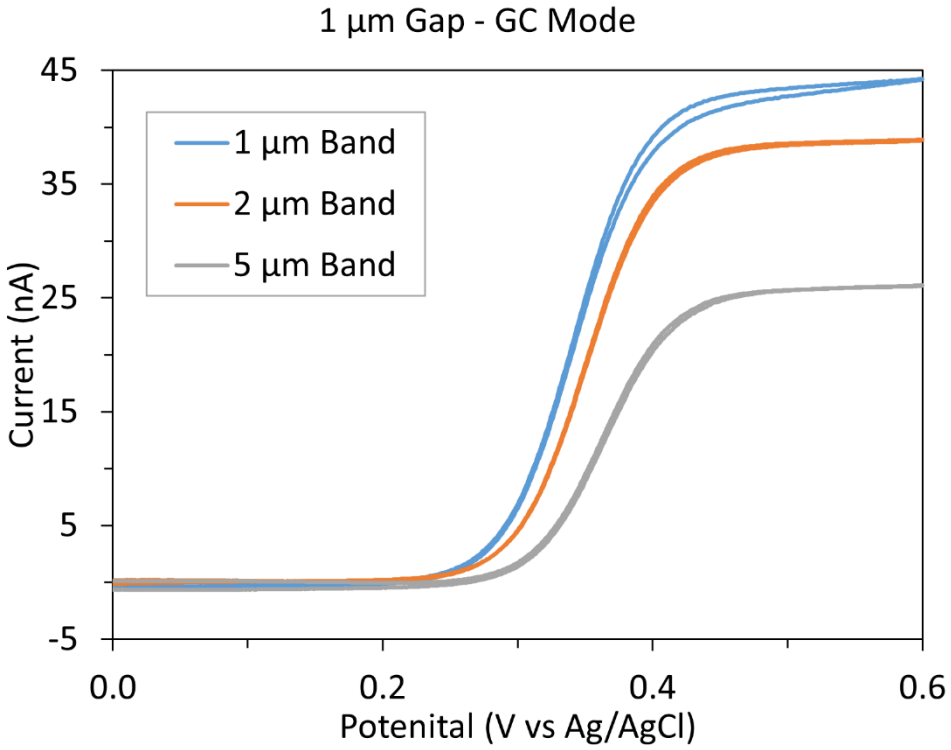


Figure 2.15 Typical cyclic voltammetric response of 1 mM FCA in 10 mM phosphate buffer from 0.0 to 0.60 V vs Ag/AgCl (sat. KCl) at 50 mV s^{-1} for IDE arrays with a 1 µm inter-electrode gap where the electrode band width was varied between 1 µm, 2 µm, and 5 µm as indicated by the legend.

A summary of the comparison of the simulated and experimental limiting currents for Non GC mode and GC Mode is given in Table 2.3. Both experimental and simulated data agree that the 1 µm bands with a 1 µm inter-electrode gap are the optimum design in both Non GC mode and GC Mode. Other aspects that agreed between the experimental and simulated data were that as the inter-electrode gap increases, a wider band gives better results compared to smaller bands. However, there are some discrepancies where the simulated data shows the 2 µm bands with 5 µm inter-electrode gap resulted in higher current values, whereas in the experimental data, the highest current values were a result of the 5 µm bands with a 5 µm inter-electrode gap. Overall, the experimental data gave higher limiting currents for all designs in both Non GC Mode and GC Mode compared to the simulated limiting currents. It is believed that the divergence between simulated and experimental data is due to limitations of the 2D model used for the simulated data. In the 2D model, only diffusion along the length of the electrode is accounted for. Experimentally, the bands operate in 3D, therefore not only is there diffusion along the length of the electrode but also diffusion at the electrode termini which is not accounted for in the 2D model. Thus, the limited currents recorded for the simulated data is lower than the experimental.[14] Another limitation of the simulations model is that it does not take into account charging at the electrode which also leads to higher experimental currents than simulated. Other factors influencing the increase in experimental current over the simulated current include the electrode surface being larger than in the simulated data as indicated by the SEM analysis and measurements taken in 2.3.2.

Table 2.3 Summary of simulated and experimental limiting current data for various array designs

	Simulated		**Experimental**	
Design **Electrode width × gap**	**Non-GC Current**	**GC Current**	**Non-GC Current**	**GC Current**
[µm]	[nA]	[nA]	[nA]	[nA]
1x1	4.4	39.0	9.9	44.2
1x2	4.3	20.2	8.7	25.0
1x5	3.8	8.0	6.6	9.6
2x1	4.5	32.1	9.2	38.9
2x2	4.4	18.9	7.6	22.7
2x5	4.0	8.6	6.3	11.4
5x1	4.1	20.2	9.5	26.1
5x2	4.1	14.8	8.9	18.4
5x5	3.7	7.2	7.1	9.9

Another important aspect of GC electrodes is th performance of the Collector electrode. The role of the Collector includes being a source of interuption to the diffusion layers of the Generator electrodes overlapping, allowing independent diffusion at each of the Generator electrodes while still maintaining a small inter-electrode gap. The Collector electrode also improves the current seen at the Generator electrodes by redox cycling. An example of the Collector response can be seen in Figure 2.16, which shows the typical GC electrode CV responses using the 1 µm bands with varied spacing as an example.

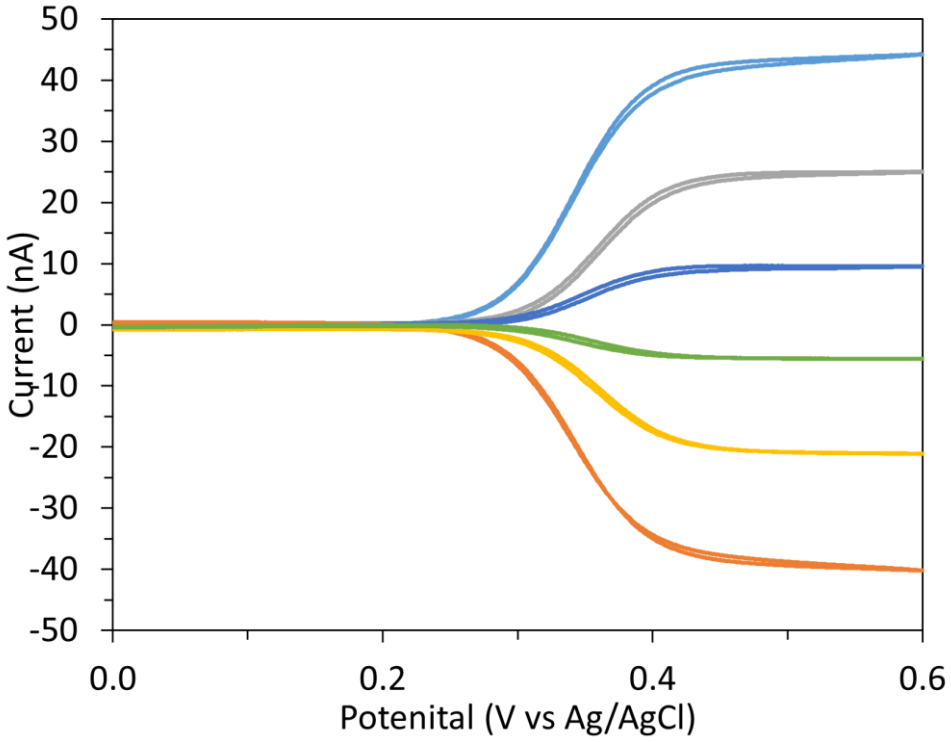


Figure 2.16 Typical CV of 1 mM FCA in 10 mM PBS from 0.0 to 0.6 V vs Ag/AgCl (sat. KCl) at 50 mV s^{-1} at 1 µm gold bands with various spacing where the Generator is swept between 0.0 to 0.6 V Ag/AgCl (sat. KCl) and the Collector was held at 0.1 V Ag/AgCl (sat. KCl). The scans were carried out at 1 µm electrode bands with 1 µm inter-electrode gaps generator (light blue) and collector (orange), 1 µm electrode bands with 2 µm inter-electrode gaps generator (grey) and collector (yellow), and 1 µm electrode bands with 5 µm inter-electrode gaps generator (dark blue) and collector (green).

The efficiency of the Collector electrode performance is measured by collection efficiency N, the ration of collector current to the generator current. The currents used to calculate N were taken from the steady state currents at 0.6 V vs Ag/AgCl (sat. KCl) of the generator and collector, respectively. An overview of the collection efficiencies obtained by the different electrode designs examined in this work can be seen in Table 2.4. The trend for Collector performance and collection efficiencies follows those seen previously in the comparison of experimental and simulated data for the Generator electrodes. However, unlike the current values, the collection efficiencies for the simulated data were reported as higher than those obtained for the experimental data. This over-estimation is due to the use of a 2D model for the simulated data. As previously

mentioned, the 2D model does not consider that the molecules diffuse away from the electrode termini in the y-axis. Therefore, an assumption is made that all molecules undergo redox cycling, resulting in an increase in expected performance.[14] Another point of interest in Table 2.4, is that the increase in the experimental collector current is not as significant as the generator. The reason for this is that the collector is not affected by capacitance as it is held at a constant potential, therefore the collector experimental current values deviate less from the simulated values.

Table 2.4 Summary of simulated and experimental Generator and Collector limiting currents and collection efficiencies (N) for 1 µm, 2 µm and 5 µm band designs.

	Simulated			**Experimental**		
Design **Electrode width × gap**	**Generator Current**	**Collector Current**	**Collection Efficiency**	**Generator Current**	**Collector Current**	**Collection Efficiency**
[µm]	[nA]	[nA]	[%]	[nA]	[nA]	[%]
1x1	39.0	-37.7	97	44.2	-39.9	90
1x2	20.2	-19.0	95	25.0	-21.1	84
1x5	8.0	-6.4	80	9.6	-5.6	59
2x1	32.1	-30.1	94	38.9	-34.8	89
2x2	18.9	-17.3	92	22.7	-19.9	88
2x5	8.6	-7.0	81	11.4	-7.8	69
5x1	20.2	-18.8	93	26.1	-21.8	84
5x2	14.8	-12.7	86	18.4	-14.2	77
5x5	7.2	-6.1	85	9.9	-6.3	64

2.3.3.2 *Capped Electrodes*

For the capped electrodes a simple capping layer the same width as the electrodes was chosen to test for improving GC sensor performance. Comparison of the electrochemical characterisation data of uncapped and capped electrode in non-GC and GC mode can be seen in Figure 2.17. As expected from the simulations completed for capped electrodes, an increase in sensor performance was seen for capped electrodes compared to uncapped in both Non GC Mode and GC Mode. In Figure 2.17 (a), for the Non GC Mode, the capped electrodes gave a 4.6 current amplification over the uncapped electrodes. In Figure 2.17 (b), for GC Mode the capped electrode current amplification over uncapped electrodes was recorded as 3.7. This is lower than the simulated performance for capped electrodes which indicated a 10.8 current amplification of capped electrodes over uncapped. However, due to the limitations of the simulation model it is believed that the simulated current amplification was over-estimated.[14] The simulation is assuming that the only reaction occurring is the redox reaction at the sides of the electrodes. In reality while the capping layer prevent a redox reaction at the top of the electrode, it may still experience capacitance which causes a reduction in current amplification in the experimental data.

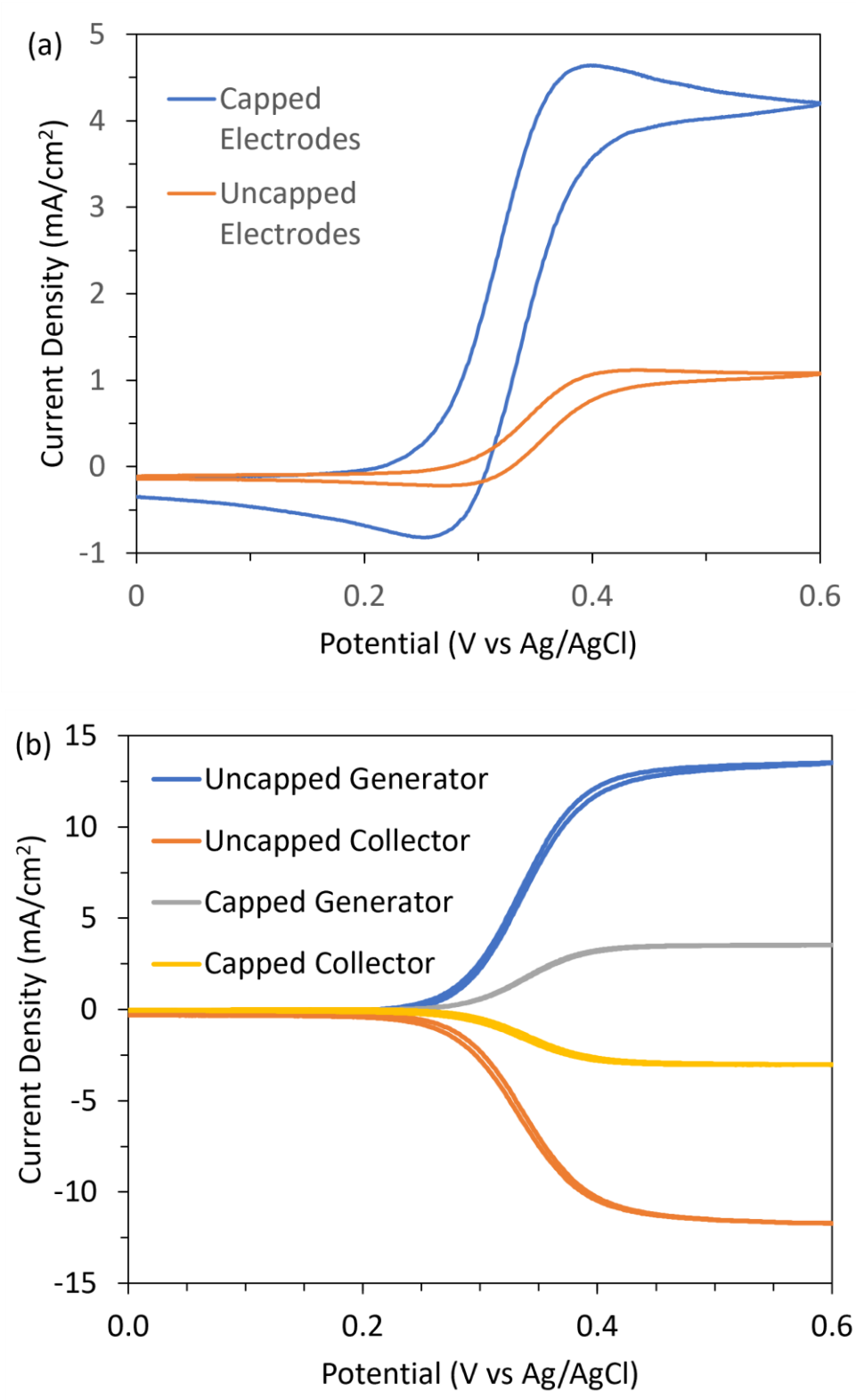


Figure 2.17 Typical CVs of 1 mM FCA in 10 mM PBS from 0.0 to 0.6 V vs Ag/AgCl (sat. KCl) at 50 mV s^{-1} at 2 µm gold bands with 2 µm inter-electrode gaps uncapped and capped electrode where (a) the Collector electrode is left unconnected while the Generator is swept from 0 to 0.6 V vs Ag/AgCl (sat. KCl), Non GC Mode, and (b) the Collector is held at 0.1 V Ag/AgCl (sat. KCl) while the Generator is swept from 0 to 0.6 V Ag/AgCl (sat. KCl), GC Mode.

2.4 Conclusion

Simulations of gold band electrode arrays were carried out varying the electrode spacing, scan rate, and incorporating GC mode designs. The simulations carried out here were an important tool for identifying the best geometries to fabricate. The initial simulations highlighted that IDE arrays would lead to smaller array footprints with a reduction in inter-electrode spacing from >60 µm to 1-5 µm while maintaining diffusionally independent electrodes. This can potentially reduce the array footprint in size by 1000x, subsequently reducing size which is important for real world applications and the materials needed which would also reduce the cost compared to larger areas. Furthermore, operating the IDE arrays in GC mode predicted a current amplification of 4.3x for an array of 2 µm wide bands with 2 µm inter-electrode gap. Additional simulations of GC designs showed the possibility of further enhancing electrode performance with GC mode by introducing a novel electrode cap, this indicated a current amplification of 10.8x for capped electrodes over uncapped electrodes Based on these simulations, several designs were put forward for fabrication. These fabricated arrays were tested structurally and electrochemically. Structural assessment by SEM showed that the electrode dimensions were in good agreement with the proposed designs. Electrochemical characterisation showed good agreement with the simulations, in that the performance followed the same trend as that for the simulated currents where the 1 µm and 2 µm bands with the 1 µm and 2 µm gaps performed best in terms of current output. These electrode designs gave 4.9 – 4.6x current amplification in GC mode compared to non-GC mode. With respect to actual current measurements, the experimental values were higher than those predicted by the simulations. This is believed to be a result of several factors including limitation in the 2D simulation design, non-faradaic currents in the real electrodes and roughness of the real electrodes. The increase in current was not

as significant at the collector electrodes due to these electrodes being held at a constant potential meaning resulting in less impact from non-faradaic currents. The addition of the novel electrode capping layer which required just a simple extra step in the fabrication process of the arrays, led to a further increase of the GC mode performance with a current amplification of 3.7x. This is lower than simulated which is attributed to limitations of the 2D simulation model discussed previously and due to the fact non-faradaic currents can still occur through the capping layer which was not taken into considerations in the simulations which reduces the current amplification. Overall, the arrays developed in this chapter have proven to be promising, novel devices for use as low-power, low-cost portable sensors.

2.5 References

1. Arrigan, D. W., Nanoelectrodes, nanoelectrode arrays and their applications. *Analyst* **2004**, 129, 1157-1165.

2. Wahl, A.; Dawson, K.; MacHale, J.; Barry, S.; Quinn, A. J.; O'Riordan, A., Gold nanowire electrodes in array: simulation study and experiments. *Faraday Discussions* **2013**, 164, 377-390.

3. Wahl, A. J. C.; Seymour, I. P.; Moore, M.; Lovera, P.; O'Riordan, A.; Rohan, J. F., Diffusion profile simulations and enhanced iron sensing in generator-collector mode at interdigitated nanowire electrode arrays. *Electrochimica Acta* **2018**, 277, 235-243.

4. Dawson, K.; Wahl, A.; Murphy, R.; O'Riordan, A., Electroanalysis at Single Gold Nanowire Electrodes. *The Journal of Physical Chemistry C* **2012**, 116, 14665-14673.

5. Elgrishi, N.; Rountree, K. J.; McCarthy, B. D.; Rountree, E. S.; Eisenhart, T. T.; Dempsey, J. L., A Practical Beginner's Guide to Cyclic Voltammetry. *Journal of Chemical Education* **2018**, 95, 197-206.

6. Streeter, I.; Compton, R. G., Linear Sweep Voltammetry at Randomly Distributed Arrays of Microband Electrodes. *The Journal of Physical Chemistry C* **2007**, 111, 15053-15058.

7. Streeter, I.; Fietkau, N.; del Campo, J.; Mas, R.; Mũnoz, F. X.; Compton, R. G., Voltammetry at Regular Microband Electrode Arrays: Theory and Experiment. *The Journal of Physical Chemistry C* **2007**, 111, 12058-12066.

8. Davies, T. J.; Compton, R. G., The cyclic and linear sweep voltammetry of regular and random arrays of microdisc electrodes: Theory. *Journal of Electroanalytical Chemistry* **2005**, 585, 63-82.

9. Chevallier, F. G.; Compton, R. G., Regular Arrays of Microdisk Electrodes: Numerical Simulation as an Optimizing Tool to Maximize the Current Response and Minimize the Electrode Area Used. *Electroanalysis* **2006**, 18, 2369-2374.

10. Wang, J. Study of Electrode Reactions and Interfacial Properties. In *Analytical Electrochemistry*; 2006, pp 29-66.

11. Aoki, K.; Morita, M.; Niwa, O.; Tabei, H., Quantitative analysis of reversible diffusion-controlled currents of redox soluble species at interdigitated array electrodes under steady-state conditions. *Journal of Electroanalytical Chemistry and Interfacial Electrochemistry* **1988**, 256, 269-282.

12. Min, J.; Baeumner, A. J., Characterisation and Optimisation of Interdigitated Ultramicroelectrode Arrays as Electrochemical Biosensor Transducers. *Electroanalysis* **2003**, 16.

13. Robertson, J., High dielectric constant oxides. *The European Physical Journal-Applied Physics* **2004**, 28, 265-291.

14. O'Sullivan, B.; O'Sullivan, S.; Naruyan, T.; Shao, H.; Patella, B.; Seymour, I.; Inguanta, R.; O'Riordan, A., Comparison of 2D versus 3D diffusion analysis at Nanowire Electrodes: Finite element analysis and experimental study. **2021**.

Chapter 3 Electrode Surface Optimisation for the Detection of Lead

3.1 Introduction

This chapter looks at optimising the electrode surface and experimental surface for the detection of lead initially in buffered solutions before moving onto tap water. NPG, as discussed in Chapter 1, was chosen as the material to enhance the gold electrodes due to its many favourable characteristics. The process for depositing NPG has been well established at MDAs by work carried out by Nagle et. al. Therefore, initial analysis in this chapter was carried out at MDAs to prove the surface enhancement with NPG and establish initial conditions for detecting lead in acetate buffer pH 4.6. At these MDAs, it was found that NPG increased the peak current for 10 ppb lead by 1.5x and the LOD was found to be 0.32 ppb with $R^2 = 0.991$ in the 0 to 10 ppb range. The deposition of NPG on the IDE arrays designed in Chapter 2 was successfully achieved. The NPG modified IDEs gave an LOD of 0.43 ppb with $R^2 = 0.9951$ in the 0 to 10 ppb range.

Prior to the analysis of lead in buffer at NPG modified arrays, the phenomenon of UPD-ASV which was also discussed in Chapter 1, was investigated. For this CV analysis was carried out at high concentrations of lead. The potential was swept through the regions where lead deposits and strips and the results peaks were assigned as bulk or UPD based on literature findings. This analysis indicated that below 100 ppb, the lead deposition and stripping was associated with UPD and not bulk.

This chapter concludes with migrating the optimised conditions for lead analysis at NPG modified IDE arrays to tap water. It was found that moving analysis from a pH-controlled buffer to tap water impeded the ability to detect lead. Further discussion on the reason for this is given herein.

3.2 Experimental

3.2.1 Electrochemical Cell Set-up, Microscopic and Electrochemical Analysis

Details of the electrochemical cell set-up and microscopic analysis have been described earlier in Chapter 2 sections in 2.2.3 and 2.2.4, respectively. Electrochemical measurements (CV and chronoamperometry) were performed using a CHI660C Electrochemical Analyser. Lead analysis was carried out on a Metrohm Auotlab/M101 potentiostat with a Metrohm Autolab Faraday Cage. Experiments were carried out in a three-electrode configuration with on-chip platinum counter and off-chip Ag/AgCl, sat. KCl reference electrode. Prior to electrochemical measurements, electrodes were cleaned by sequential immersion of the chips for 10 minutes in acetone, iso-propyl alcohol (IPA), and DI water, followed by a thorough rinse with DI water and drying in a stream of filtered nitrogen.

3.2.2 Electrode Modification with Nanoporous Gold

The gold electrode arrays were characterised in 1 M NaOH by recording a standard CV from -0.90 to 0.88 V vs Ag/AgCl (sat. KCl) at 50 mV/s prior to depositing a gold-silver alloy, as a precursor to NPG. This required the reduction of gold and silver ions from a cyanide bath. The plating bath used was made up of 20 mM potassium gold cyanide ($KAu(CN)_2$), 100 mM potassium silver cyanide ($KAg(CN)_2$) and 250 mM sodium carbonate (Na_2CO_3) as the supporting electrolyte. Reduction of the gold and silver onto the micro-disc arrays was achieved using chronoamperometry at a potential at -1.19 V vs Ag/AgCl (sat. KCl) for 3 s. Another 1 M NaOH CV was run to confirm the alloy had been deposited. Selective etching of the silver was done by placing the chip into a solution

of 25% nitric acid for 2 mins. Removal of the silver is confirmed by another CV in 1 M NaOH. Removal of the silver causes almost 30% volume shrinkage of the gold-silver alloy. The ratio of silver to gold deposited in the alloy dictates the size of the pores and ligaments created in the resulting NPG structure, i.e., tuneable porosity. In this case, the deposit ratio used was $Au_{0.18}Ag_{0.82}$ which results in NPG structures with ~20 nm pores and ~30 nm ligaments. This approach is based on the work of Searson et al.[1], who demonstrated that this particular composition of $Au_{0.18}Ag_{0.82}$ yields the largest NPG surface area following etching. The CVs from the characterisation in 1 M NaOH after each NPG modification step can be seen in Figure 3.1.

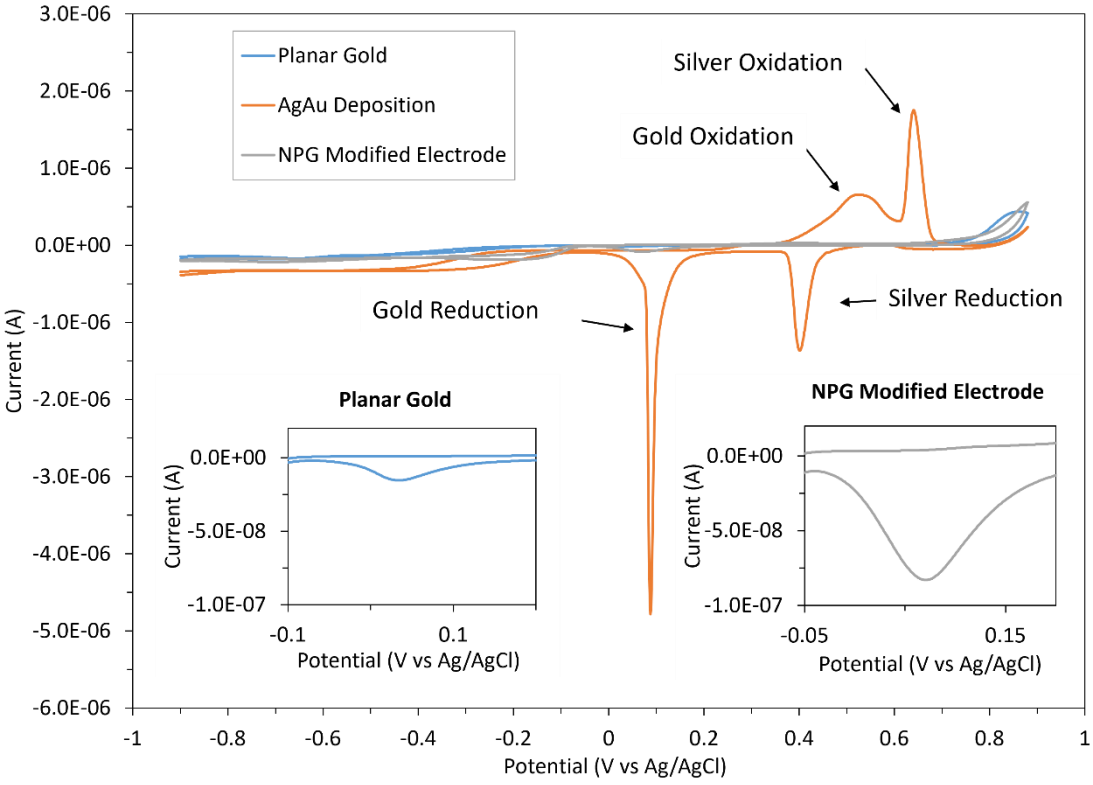


Figure 3.1 CVs in 1 M NaOH recorded from -0.90 to 0.88 V vs Ag/AgCl (sat. KCl) at 10 mVs^{-1} recorded at a gold micro-disc array (blue), after $Au_{0.18}Ag_{0.82}$ electrodeposition (orange) and at an NPG modified array (grey). Inserts show gold oxide reduction peaks at planar gold and NPG modified arrays (left and right, respectively)

The CV at a planar gold micro-disc array (blue line) shows negligible current flows over the potential range from -0.9 V to 0.2 V prior to the onset of gold oxide monolayer formation, while, on the reverse scan, the corresponding reduction peak is observed at around 0.035 V. The magnitude of the reduction peak was found to be highly reproducible, -13.6 $\pm$ 1.3 nA (n=18) and -3.5 $\pm$ 0.55 nA (n=24) for micro-disc and IDE arrays, respectively. The average electrochemically active area was estimated from the charge associated with the gold oxide reduction peak. The electrochemically active areas were found to be 3.84 $\pm$ 0.43 x 10^{-4} cm^2 for micro-disc arrays and 1.37 $\pm$ 0.27 x10^{-4} cm^2 for IDE arrays. The electrochemically active surface area was calculated by recording the charge of the gold oxide reduction peak and dividing it by the charge associated with the reduction of the gold oxide layer, 390 µC cm^{-2}. These were almost twice that estimated by the geometric surface area (1.98 x 10^{-4} cm^2 and 6.48 x 10^{-6} cm^2 for micro-disc and IDE arrays, respectively). It is believed the reason for this increase is due to the assumption of a monolayer oxide formation only with 1:1 stoichiometric conditions, which are difficult to achieve practically at the micron scale; the estimated electrochemically active area value may be due to the formation of oxide multilayers.[2]

The chronoamperometric data obtained representing the electrodeposition of $Au_{0.18}Ag_{0.82}$ alloy were found to be highly reproducible; the shape and magnitude of the recorded signal was very consistent from chip to chip. Electrodeposition of $Au_{0.18}Ag_{0.82}$ involves the reduction of gold and silver ions present in the plating bath at the gold micro-disc electrode surface. In its simplest form, the reaction may be described as:

$$Au^{+}(aq) + Ag^{+}(aq) + 2e^{-} \rightarrow AuAg(s) \qquad 3.1$$

The thickness T of the electrodeposited layer may be estimated using equation 3.2:

$$T = \frac{QM_{wt}}{nFAd} \quad 3.2$$

where Q is the total charge associated with the electrodeposition (C), M_{wt} is the molecular weight of the resulting $Au_{0.18}Ag_{0.82}$ alloy (g mol^{-1}), n is the number of electrons involved in the reaction, F is Faraday's constant (C mol^{-1}), A is the area of the deposit (cm^2), and d is the density of the alloy (g cm^{-3}). An average thickness 364.8 $\pm$ 24.9 nm (n=24) for IDE arrays was measured. The CV of the $Au_{0.18}Ag_{0.82}$ alloy (Figure 3.1) clearly indicated the presence of Au and Ag from the characteristic metal oxide peaks seen at 0.6 V and 0.67 V, respectively, in the anodic region and from the corresponding reduction peaks seen at 0.13 V and 0.44 V, respectively, in the cathodic region. The alloy deposition was highly reproducible, as the current magnitude of the oxidation and reduction peaks were found to be consistent: 0.71 ± 0.07 µA for Au oxidation, 1.81 ± 0.29 µA for Ag oxidation, -4.1 ± 2.26 µA for Au reduction and -1.3 ± 0.07 µA for Ag reduction for micro-disc arrays (n=18) and 0.1 ± 0.02 µA for Au oxidation, 0.27 ± 0.06 µA for Ag oxidation, -5.0 ± 0.1 µA for Au reduction and -0.17 ± 0.03 µA for Ag reduction for IDE arrays. Following the etching step of a 2 mins immersion in 25% nitric acid, the resulting de-alloyed electrode yields a CV response in 1 M NaOH (shown in grey) that is typical of gold and shows the absence of silver oxidation and reduction peaks, indicating selective removal of the silver component. The gold oxide reduction peak current has increased by an order of magnitude, which is associated with an increase in electrochemical active surface area. This peak current was also found to be reproducible across NPG modified arrays: -98.6 ± 20 nA (n=18) and -21.5 $\pm$ 3.6 nA (n=24) for micro-disc and IDE arrays, respectively.

An average electrochemically active surface area of $3.44 \pm 0.68 \times 10^{-3}$ cm^2 for micro-disc arrays and $7.91 \pm 1.77 \times 10^{-4}$ cm^2 for IDE arrays was estimated from the charge associated with gold oxide reduction peak, which is approximately 9 and 6 times higher than the planar gold micro-disc and IDE arrays, respectively.

SEM characterisation of the NPG modified arrays showed a thin film NPG that partially filled the recessed micro-disc arrays and covered the protruding IDE arrays. A high magnification image of an individual NPG modified micro-disc shows that the NPG film diameter is the same as the underlying planar gold, as highlighted in Figure 3.2(a). For IDE arrays, a high magnification image of individual bands revealed that the NPG modified bands were 0.8 µm thicker than unmodified planar gold IDE bands, as seen in Figure 3.2(b). High magnification tilted images of the substrates showed that the NPG film deposited in the micro-disc arrays was approximately 251 ± 22 nm and the NPG film deposited onto the IDE arrays was approximately 329 ± 21.5 nm, which agrees with the average thickness calculated from the deposition charge data. Overall, the band height increased from 350 nm to ~ 1 µm. As mentioned previously, the etching of the silver leads to 30% shrinkage of the NPG structure. This leads to cracks in the structure as can be seen in both Figure 3.2(a) and (b). The cracks on the IDE arrays in Figure 3.2(b) are primarily in the centre of the band, this is a result of this being the weakest part of the deposit. Increased magnification of the SEM images also highlighted the sponge-like 3D structure with interconnecting pores of 20-30 nm and ligaments of 30-50 nm that typifies NPG films, which can be seen in Figure 3.2(c). While the pores and ligaments could be measured from the SEM images, it does not show that the pores are interconnecting, this is an assumption made based on comparison with other literature of NPG deposited from $Au_{0.18}Ag_{0.82}$.

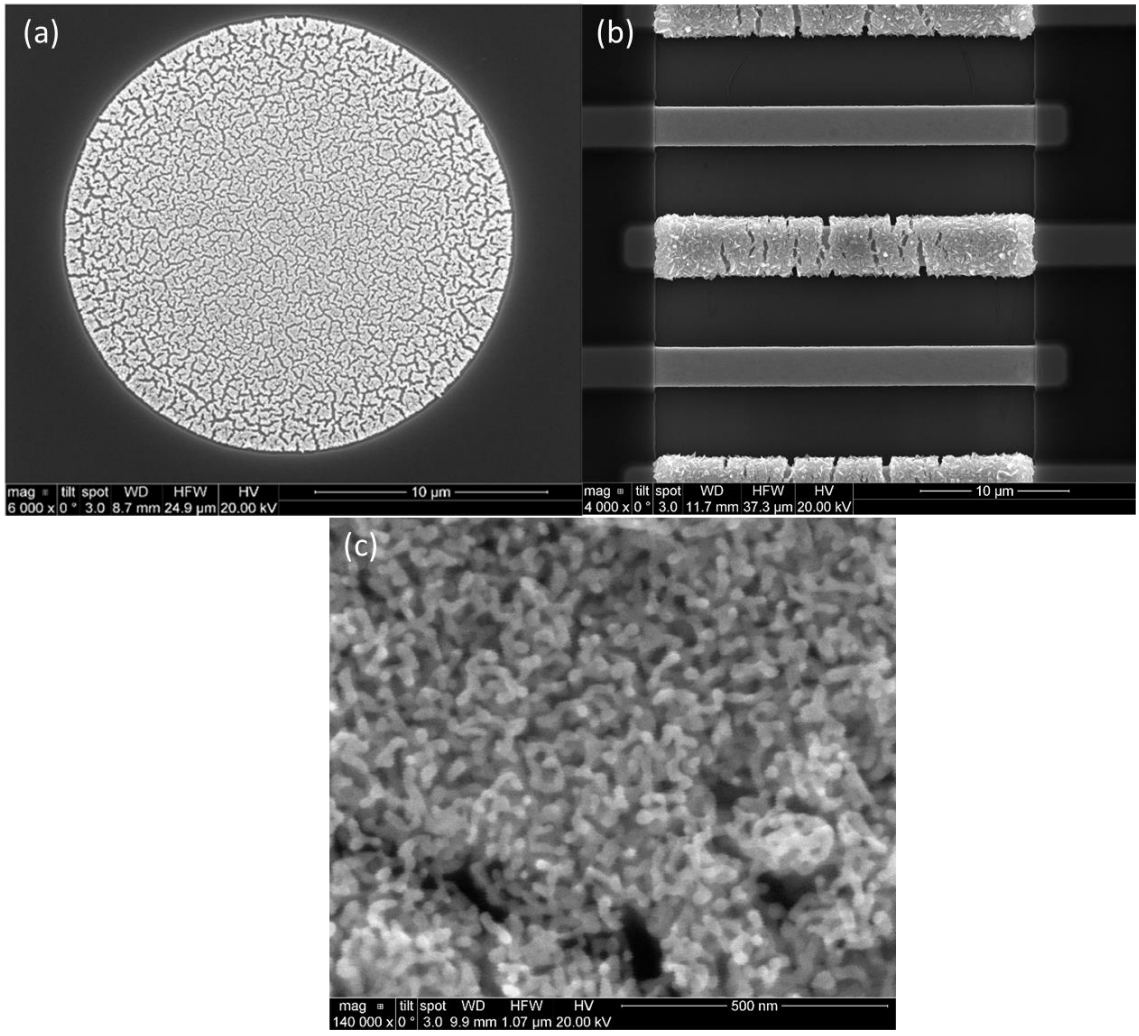


Figure 3.2 SEM Images of (a) NPG deposition in an individual 20 µm diameter micro-disc, (b) NPG deposited on several 3 µm wide micro-band electrodes in an IDE array (c) high magnification image of NPG deposit.

3.2.3 Electrochemical Detection of Lead at Micro-Disc and IDE Arrays

Lead analysis measurements were carried out on a Metrohm Auotlab/M101 potentiostat with a Metrohm Autolab Faraday Cage. Initial lead analysis measurements were carried out in 0.1 M acetate buffer pH 4.6, which was made up of 0.05 M acetic acid and 0.05 M sodium acetate. The pH 4.6 acetate buffer was chosen based on information in the literature that studied the detection of lead at gold-modified electrodes.[3-7] From these works, a pH of 4.5 to 5 was highlighted as optimal for the detection of lead. Lower pH values, such as pH 3, gave a reduced stripping current of lead due to the electrode surface

being disturbed by a large number of hydrogen ions (H^+).[3, 4] A reduction in lead stripping current was also seen at higher pH values, above pH 6, due to hydrolysis of the lead ions.[3, 4, 6] Finally acetate buffer was chosen as it was deemed the best supporting electrolyte when tested against phosphate buffered saline and HCl.[6] Various concentrations of lead(II) nitrate were added to acetate buffer, the solution was held at the optimum potential established in the optimisation process for lead accumulation on the electrode surface, followed by stripping using square wave stripping voltammetry at an amplitude of 25 mV, step increment 5 mV and frequency 50 Hz. The same procedure was used for the analysis of lead in tap water collected from the drinking fountain in the Tyndall National Institute instead of 0.1 M acetate buffer pH 4.6. All measurements were performed in triplicate.

3.3 Results and Discussion

3.3.1 Analysis at Gold Micro-Disc Arrays

3.3.1.1 *Lead Analysis in 0.1 M Acetate Buffer pH 4.6*

3.3.1.1.1 Determination of Underpotential Deposition of Lead

Initial analysis of UPD lead deposition was carried out at planar gold micro-disc arrays with a high concentration of lead, 10 ppm. CV analysis was used where the potential was swept from 0.0 V to -1.0 V, and the results can be seen in Figure 3.3. As the potential is swept in the negative direction, reduction of oxygen commences at -0.2 V and continues over the entire potential range in the CV creating a competing reaction for the lead analysis. The lead deposition peaks identified at -0.37 V and -0.58 V corresponding to UPD and bulk deposition, respectively. On the reverse scan, the bulk lead deposit strips first at 0.43 V and the UPD lead at the less negative potential of -0.31 V due to stronger interactions of the deposited lead on the gold electrode in the UPD layer than in the bulk deposit.[8] This behaviour is consistent with previous publications which investigated the UPD behaviour of lead at gold electrodes.[8-11]

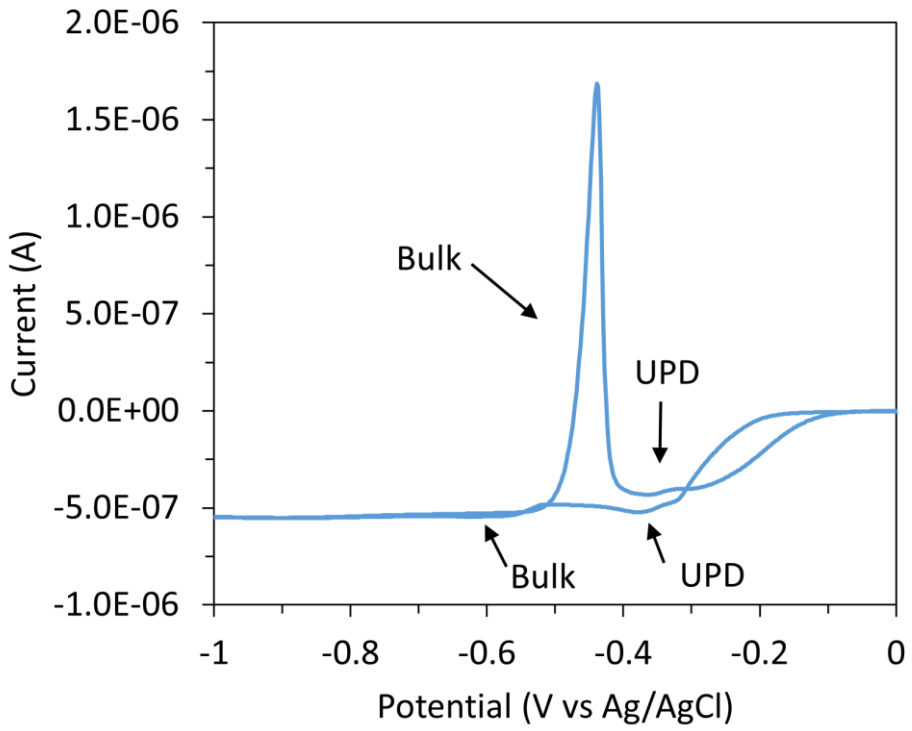


Figure 3.3 Typical CV of 10 ppm lead nitrate in 0.1 M acetate buffer pH 4.6 swept from 0.0 V to -1.0 V vs Ag/AgCl (sat. KCl) at 100 mV s^{-1} at 20 µm gold micro-disc array, highlighting the deposition and stripping peaks attributed to UPD and bulk.

Analysis to investigate the UPD of lead at lower concentrations was carried out at planar gold micro-disc arrays using separate deposition and stripping steps. A deposition potential of -0.95 V was applied using chronoamperometry for 600 s and subsequent anodic stripping was carried out using square wave voltammetry. These conditions were chosen based on optimised deposition and stripping conditions which were established and are highlighted further below. The concentration ranges investigated for this work were 10 ppb to 500 ppb lead(II) nitrate in 0.1 M acetate buffer pH 4.6. In the square wave stripping voltammograms recorded following deposition of lead in the concentration range of 100 ppb to 500 ppb, peaks indicative of UPD and bulk deposition were identified which is shown in Figure 3.4. The peak at -0.35 V is attributed to bulk lead as it strips at lower potentials while the more positive peak at -0.22 V is a result of stripping of a layer that was deposited in a UPD process. The peak shape also matches that seen for the

detection of lead under similar conditions in the literature.[3, 6] In the range of 10 ppb to 75 ppb, a single peak is observed for the detection of lead, as highlighted by the insert in Figure 3.4. The single peak appears at -0.22 V which indicates that at these concentrations only UPD of lead occurs, where only a monolayer or sub-monolayer of lead is being deposited onto the electrode surface.

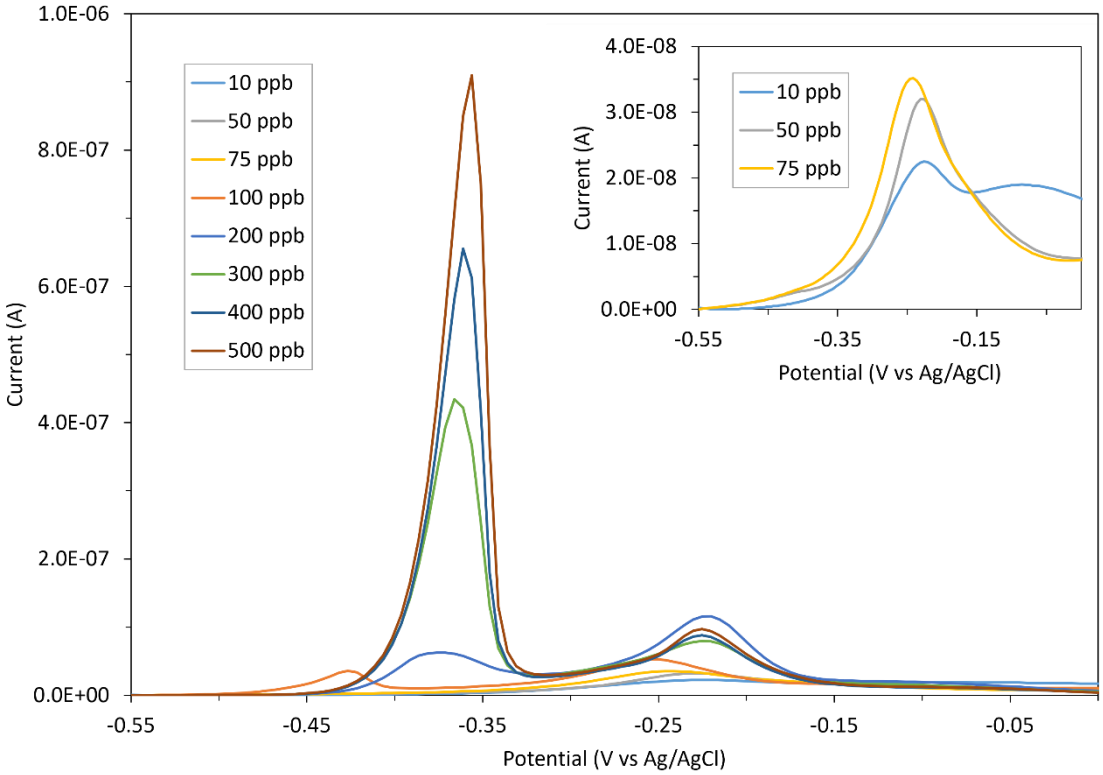


Figure 3.4 SWV of 10 ppb - 500 ppb lead(II) nitrate in 0.1 M acetate buffer pH 4.6 deposited at -0.95 V vs Ag/AgCl (sat. KCl) for 600 s at planar gold 20 µm micro-disc arrays. Insert highlights the response of the lower concentration range of 10 ppb – 75 ppb lead(II) nitrate.

Investigation of lead deposition was carried out at NPG-modified micro-disc arrays at 10 ppm using CV analysis where the potential was swept from 0.5 V to -1.0 V, and the results can be seen in Figure 3.5. Stripping of the bulk lead deposit was noted at -0.42 V. Two UPD deposition peaks were noted at -0.37 V and at -0.05 V, while the corresponding stripping peaks occurred at -0.21 (UPD1) and -0.03 V (UPD2), respectively. The UPD peak at -0.21 V occurs at the same potential as that observed at planar gold micro-disc

arrays shown in Figure 3.4 while the peak at -0.04 V may be assigned to the presence of different surface facets in NPG. It was reported by Qian et al.[12] that different types of surface facets can be discriminated on the basis of their differing lead UPD stripping peak potentials and the lead UPD process on gold may be exploited as a means of identifying the presence of different surface facets in NPG. Qian et al.[12] discerned three UPD stripping peaks at NPG in 1 M sulphuric acid at 0.32 V, 0.45 V and 0.61 V vs RHE which they attributed to the presence of kinks/step sites, Au{111} facets, and a combination of Au{110} and Au {100} facets, respectively. The former two peak potentials of 0.32 and 0.45 V correspond to potentials of -0.15 V and -0.02 V vs Ag/AgCl (sat. KCl) at pH 4.6, which are similar to the potentials associated with UPD1 and UPD2 peaks, respectively highlighted here in Figure 3.5(b), allowing the tentative assignment of UPD1 to the presence of kinks/steps and UPD2 to Au{111} facets. Further comparison of CVs of 10 ppm lead depositions and stripping peaks at planar gold (Figure 3.3) and NPG (Figure 3.5), highlighted an increase in hydrogen evolution at the NPG electrodes. This aligns with literature where, Sukeri and Bertotti[13] reported on the notable electrocatalytic activity of a NPG film electrode for the hydrogen evolution reaction (HER) with respect to low onset potential and overpotential and a large cathodic current density. The performance for HER observed was comparable to platinum.

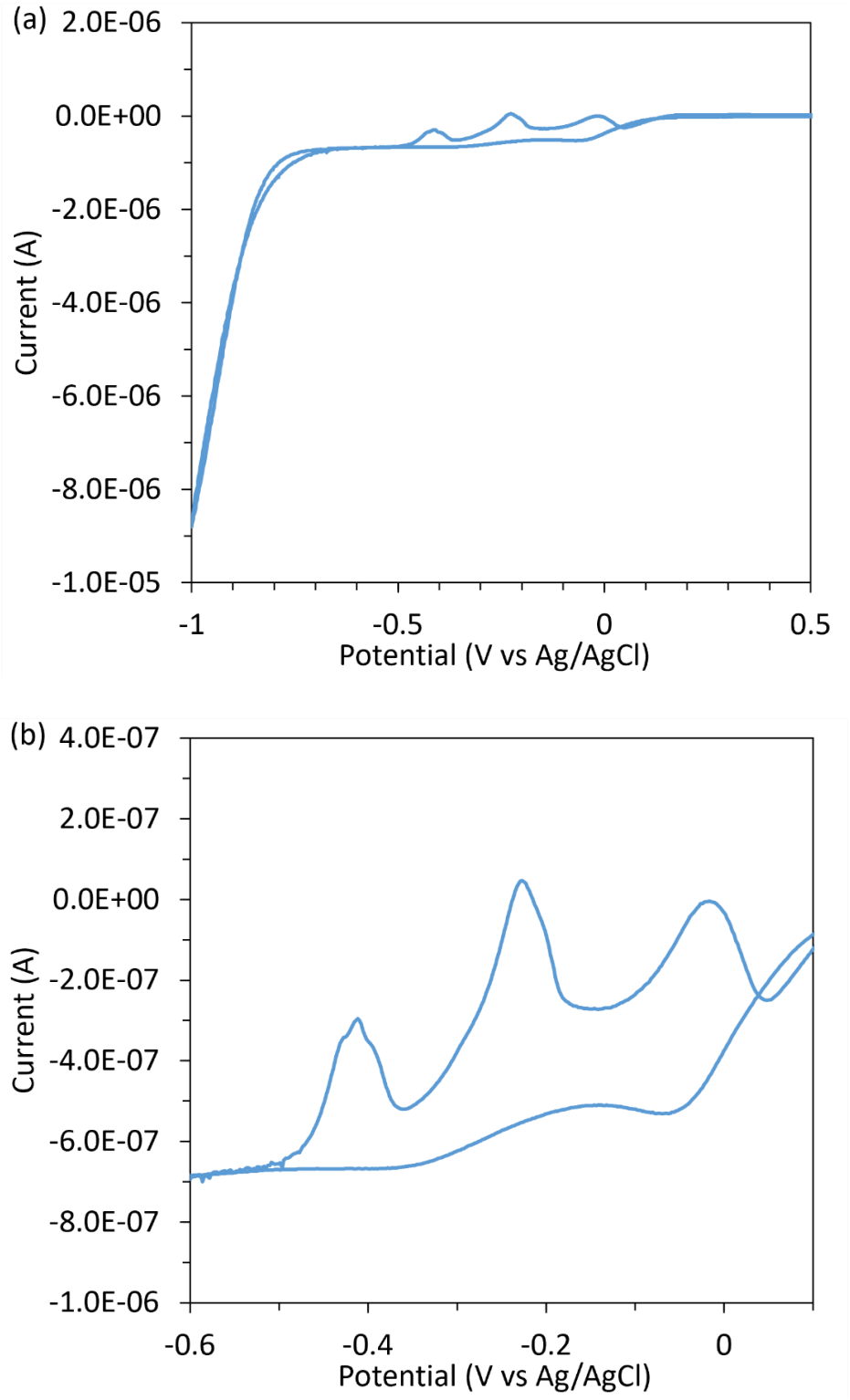


Figure 3.5 Typical CV of 10 ppm lead nitrate in 0.1 M acetate buffer pH 4.6 swept from 0.5 V to -1.0 V vs Ag/AgCl (sat. KCl) at 50 and at 100 mV s^{-1} at 20 µm gold micro-disc array, where (a) is the full CV range and (b) is highlighting the depositions and stripping peaks in the 0.1 to -0.6 V range.

The lead concentration ranges investigated for this work were 10 ppb to 500 ppb lead(II) nitrate in 0.1 M acetate buffer pH 4.6. In the square wave stripping voltammograms recorded following deposition of lead in this concentration range, stripping peaks indicative of UPD and bulk deposition were identified, as shown in Figure 3.6. The stripping peak at -0.44 V is attributed to a bulk lead deposit while the UPD stripping peaks at ca. -0.17 V and 0.05 V are assigned to UPD1 and UPD2, respectively. For lead detection in the concentration range of 10 ppb to 100 ppb, a single UPD peak is observed for the detection of lead, UPD2. Unlike the planar gold, the NPG structures do not reach bulk deposition in the 100 ppb to 500 ppb range. Bulk deposition only forms once the UPD is at maximal charge. The results in Figure 3.6 indicate that the maximal charge of UPD2 has not yet been reached. A possible explanation as to why bulk forms at lower concentrations in planar than NPG is because the increase in surface facets of gold in NPG increasing the maximal charge that needs to be reached in the UPD region before bulk deposition is achieved.

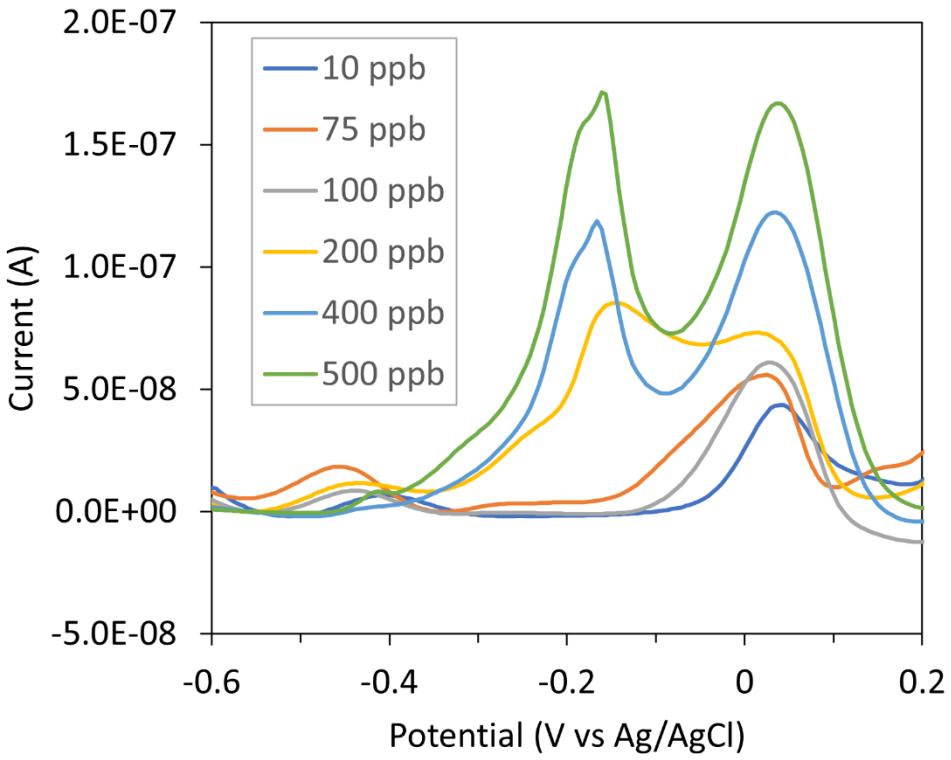


Figure 3.6 SWV of 10 ppb - 500 ppb lead(II) nitrate in 0.1 M acetate buffer pH 4.6 deposited at -0.95 V vs Ag/AgCl (sat. KCl) for 600 s at NPG-modified 20 µm micro-disc arrays.

3.3.1.1.2 Influence of Deposition and Stripping Conditions

Both the lead deposition potential and time as well as the frequency for the SWV stripping step were varied in order to obtain a guide for what the parameters should be set at. For the determining deposition time, the deposition potential was held at -0.95 V while the time was varied in the range of 75 s to 900 s. It was found that the lead peak current increased with increasing deposition to 600 s, after this time the performance plateaus, highlighted in Figure 3.7 (a). As a result, 600 s was chosen as the deposition time for lead analysis deposition. For deposition potential, the deposition time used was 600 s while the deposition potential was varied in the range of -0.55 V to -1.05 V. In this instance it was found that the lead peak current increased with decreasing deposition potential to -0.95 V, after this the performance plateaus for NPG samples and declines for planar samples, as seen in Figure 3.7 (b). Here, -0.95 V was chosen as the potential for lead deposition.

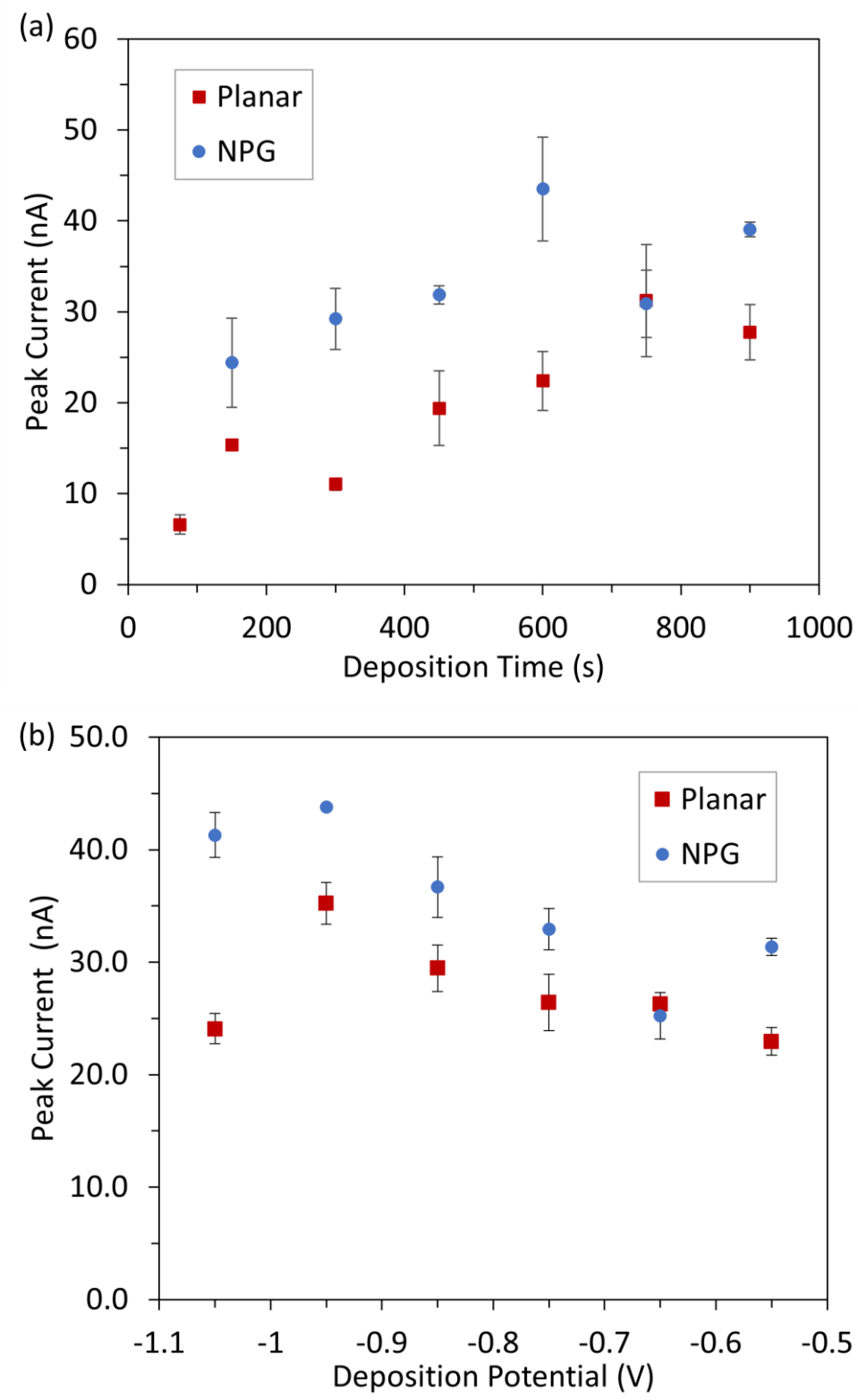


Figure 3.7 SWV peak current responses for 10 ppb Lead Nitrate in 0.1 M Acetate Buffer pH 4.6 for (a) deposition at -0.95 V vs Ag/AgCl (sat. KCl) with varied time and (b) deposition for 600 s with varied deposition potential at planar and NPG-modified 20 µm gold micro-disc arrays.

For optimum stripping, the SWV frequency was investigated. For this analysis, the stripping followed a deposition step using the optimum deposition conditions outlined above. The frequency controls the pulse width and scan rate of the SWV stripping step. The sensor performance increased with increasing frequency up to 50 Hz, after which it declined, as can be seen in Figure 3.8. As a result, 50 Hz was deemed optimum for the lead analysis stripping step.

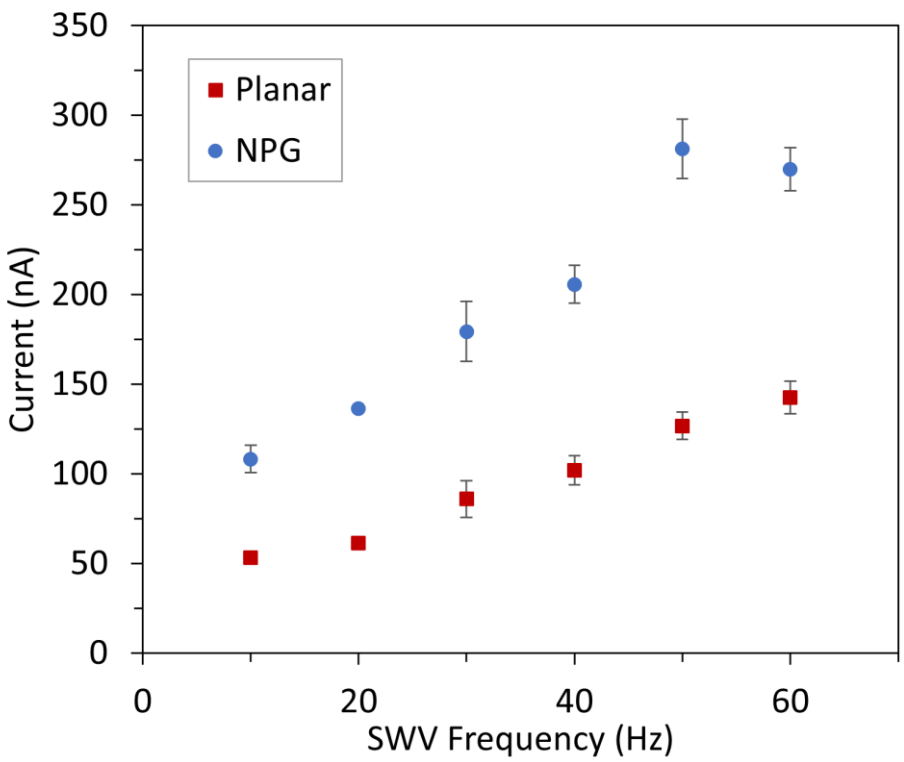


Figure 3.8 SWV peak current responses for 10 ppb Lead Nitrate in 0.1 M Acetate Buffer pH 4.6 deposited at -0.95 V vs Ag/AgCl (sat. KCl) for 600 s with varied frequency in the SWV stripping step at planar and NPG-modified 20 µm gold micro-disc arrays.

Using the optimum conditions for deposition and stripping established above, the performance of an unmodified 20 µm micro-disc array and an NPG modified 20 µm micro-disc array was examined in a solution of 10 ppb lead nitrate in 0.1 M acetate buffer pH 4.6. These results showed a 1.5-fold increase in current response for the detection of lead at NPG, peak at 0.05 V, compared to planar gold, peak at -0.25 V, as can be seen in

Figure 3.9. In the SWV responses, there are other peaks present outside of those indicated to be lead. These peaks have been determined as a background reaction as then are present in both NPG and planar results and are independent of lead concentration. The improved electroactivity of NPG is attributed to the highly unique, curved morphology of the 3D "sponge-like" containing a high density of steps, holes and kinks. These features are populated by low-coordination atoms which interact more strongly with the target molecules.[2, 14-16] Figure 3.9 also highlights a difference in the UPD peak potentials for the NPG and planar samples, where the NPG sample occurs at a more positive potential of 0.08 V. This suggests the existence of different surface facets in NPG than are present in planar Au, as was discussed in 3.3.1.1. The UPD peak at NPG may be associated with Au{111} and that at planar Au with surface steps and kink sites, based on the comparison made earlier with the work of Qian et al.[19] The dependence of the lead UPD peak potential on the surface facets has been highlighted in work carried out recently by both Castillo et al.[17] and Qian et al.[12] where different lead UPD peaks have been assigned to the different surface facets of gold. In previous analysis of the NPG structures, it was found that modification of gold electrodes increases the surface area by a factor of 9. Here however there was only a 1.5x current amplification for the NPG modified electrodes compared to the planar electrodes. There are two factors contributing to the reduction in expected enhancement from NPG. The first is that the initial increase in NPG of 9x was calculated by CVs carried out in NaOH with a scan rate of 10 mV s^{-1} which is much slower than the SWV carried out to strip the lead which is 250 mV s^{-1}, faster scan rates can negate the increase that would be seen from NPG. Additionally, the lead molecules may not penetrate as deeply into the NPG structure as NaOH which would also reduce the enhancement expected from NPG.

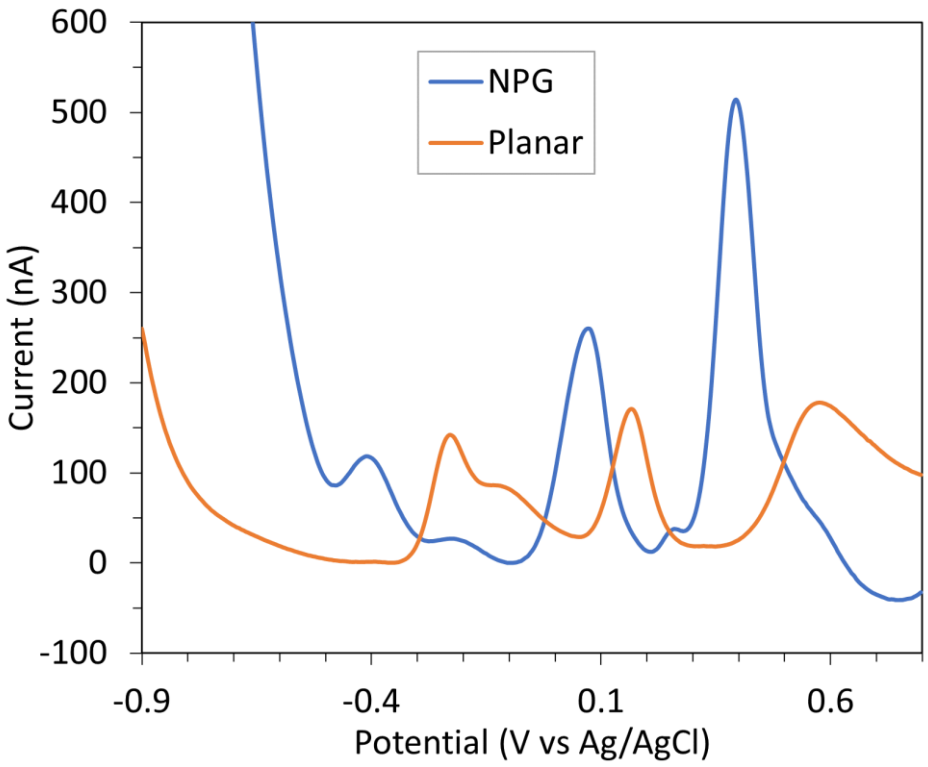


Figure 3.9 SWV current peaks for 10 ppb Lead Nitrate in 0.1 M Acetate Buffer pH 4.6 at unmodified 20 µm micro-disc arrays (red) and NPG modified 20 µm micro-disc arrays (blue)

3.3.1.1.3 Calibration of Lead in Acetate Buffer pH 4.6

To explore the performance of NPG modified micro-disc arrays for the detection of lead, samples were tested in a solution of 0.1 M acetate buffer with varying concentrations of lead nitrate. As established in 3.3.1.1.2, lead was deposited on the arrays at -0.95 V for 600 s and a frequency of 50 Hz was used during the square wave stripping step. However, in practice, a deposition potential of -0.75 V proved to be better, particularly for concentrations below 10 ppb. The reason for this could be due to the evolution of hydrogen which could interfere with the detection of lower concentrations of lead.[18] Cyclic voltammograms for planar gold and NPG modified micro-disc arrays in 0.1 M acetate buffer pH 4.6 are shown in Figure 3.10 and highlight that hydrogen evolution begins at a more positive potential of -0.75 V at NPG modified arrays. This is again consistent with NPG being more catalytically active, in this case, for the evolution of hydrogen. As seen in Figure 3.7(b), the extent of hydrogen evolution at -0.95 V did not

impact detection for a 10 ppb sample. However, it is known that the generation of hydrogen gas can interfere with the accumulation of metal ions from the bulk solution onto the electrode surface.[19] As a result, detection of sub 10 ppb concentrations could be impeded at a deposition potential of -0.95 V. Therefore -0.75 V was used for the following work.

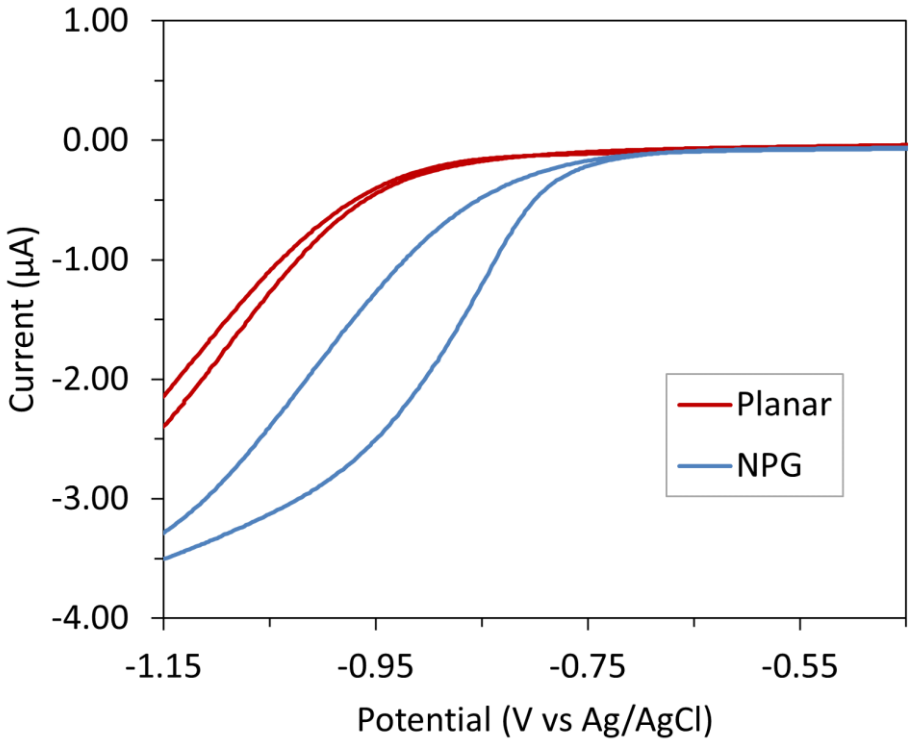


Figure 3.10 Typical CV at 10 mVs^{-1} of planar and NPG modified 20 µm micro-disc array in 0.1 M acetate buffer pH 4.6 from -0.45 V to -1.15 V vs Ag/AgCl (sat. KCl) highlighting the onset of hydrogen evolution.

Square wave stripping voltammograms were obtained using the conditions outlined above which can be seen in Figure 3.11. The peak for lead occurs at ~0.05 V. A slight shift in peak potential is observed. This is not unusual and can be seen in several sources in the literature however, it is never acknowledged nor is an explanation given as to why this occurs.[6, 19-21] A possible reason this shift in this instance is that there are different arrays used for each measurement which will lead to a degree of variability between measurements. Also seen in Figure 3.11 is a peak in the blank scan, this appears to be a

background reaction. The stripping peak for lead in this analysis gives a single peak associated with UPD1. This is expected based on the analysis carried out previously establishing UPD and bulk deposition and stripping of lead at NPG which indicated that from 100 ppb and below there is a single lead peak associated with UPD1.

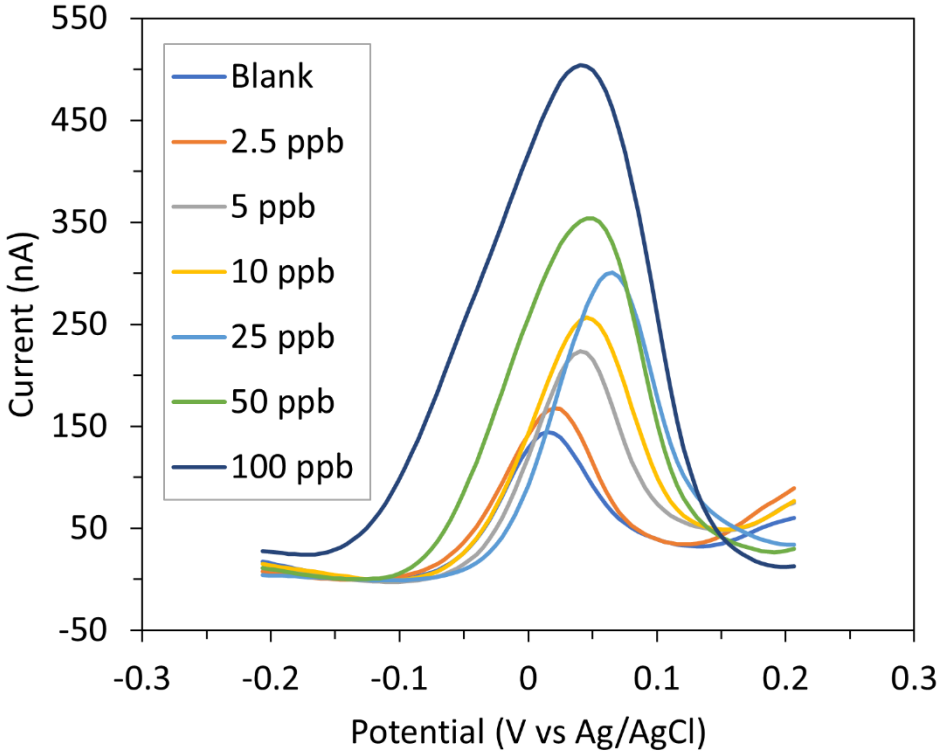


Figure 3.11 SWV of for varied concentrations of lead nitrate in 0.1 M acetate buffer pH 4.6 at NPG-modified 20 µm gold micro-disc arrays. Each measurement was carried out in triplicate with a new array used for each measurement.

The peak current values were plotted as a calibration plot; see Figure 3.12. As highlighted from Figure 3.11, it was found that the lead peak current was proportional to the concentration of lead nitrate in the solution tested (R^2 = 0.9257 for the range 0 ppb to 100 ppb, see Figure 3.12 (a)). Improved linearity (R^2 = 0.991) is seen when focusing on the range 0 to 10 ppb, Figure 3.12(b), which is the commercial range of interest for electrochemical lead sensors as 10 ppb is the maximum allowable level of lead in drinking water.[22] Above 10 ppb, a tapering effect of the peak current is seen leading to a reduction

in the R^2 value for the overall range of 0 ppb to 100 ppb. Based on the equation of the line obtained in Figure 3.11(b), the LOD was found to be 0.32 ppb. The LOD was calculated from the calibration plot using the following equation:[11]

$$LOD = (3.3\frac{SD}{S}) \quad 3.3$$

Where *SD* is the standard deviation of the lowest measurable concentration and *S* is the sensitivity of the electrode, as defined by the slope of the calibration plot.

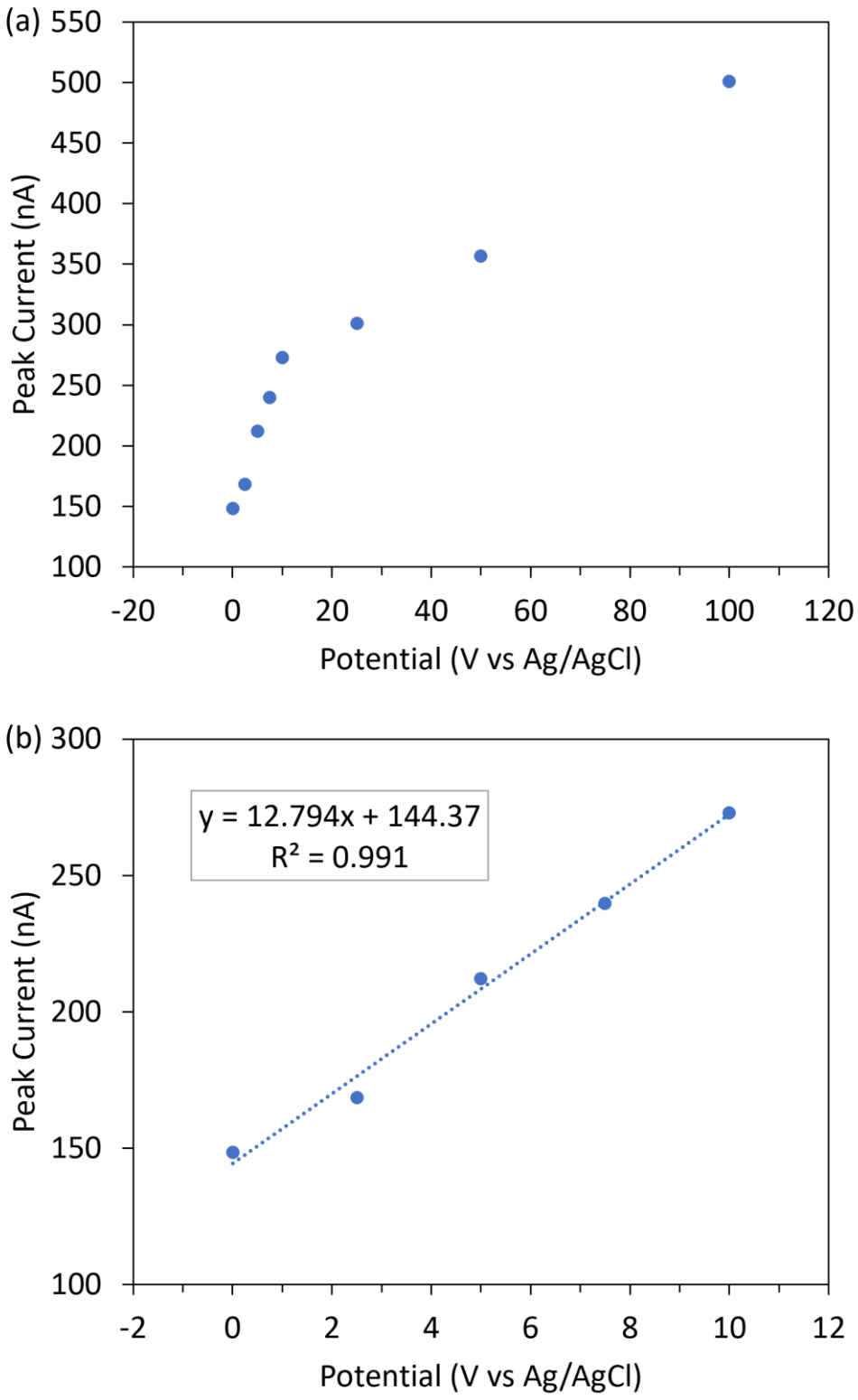


Figure 3.12 Calibration plots of lead peak stripping current at NPG modified 20 µm micro-disc arrays for (a) 0 to 100 ppb and (b) 0 to 10 ppb. Each measurement was carried out in triplicate with a new array used for each measurement.

3.3.2 Analysis at Nanoporous Gold Modified Interdigitated Electrode Arrays

3.3.2.1 *Lead Analysis in Acetate Buffer pH 4.6*

3.3.2.1.1 Investigating the Influence of Deposition and Stripping Conditions

As the process for lead analysis moved from micro-disc arrays to interdigitated electrode arrays, the deposition and stripping conditions were re-examined. Initially, deposition time was investigated with a deposition potential of -0.75 V, which was the optimised deposition time for micro-disc arrays. The deposition times investigated were in the range of 100 to 600 s. The results showed that for lower deposition times of 100 and 200 s, the 10 ppb lead peak was lower and more varied than higher deposition times. The reason for this was due to insufficient time being given for a measurable layer of lead to be deposited on the surface leading to variable results as the lower concentrations are more susceptible to interference from hydrogen evolution that occurs while the lead in being deposited. From 300 to 600 s the peak current seemed to plateau and the deviation between measurements was reduced. Therefore, 300 s was chosen as the optimum deposition time for interdigitated arrays. Using 300 s as the deposition time, the deposition potential was investigated in the range of -0.55 to -1.05 V. Here, it was found that the 10 ppb lead peak current peaked at -0.65 V, after which the peak current declines and plateaus for the lower deposition potentials of -0.85 to -1.05 V. Therefore, -0.65 V was chosen as the optimum deposition potential for interdigitated electrode arrays. The results for investigating both deposition time and potential can be seen in Figure 3.13.

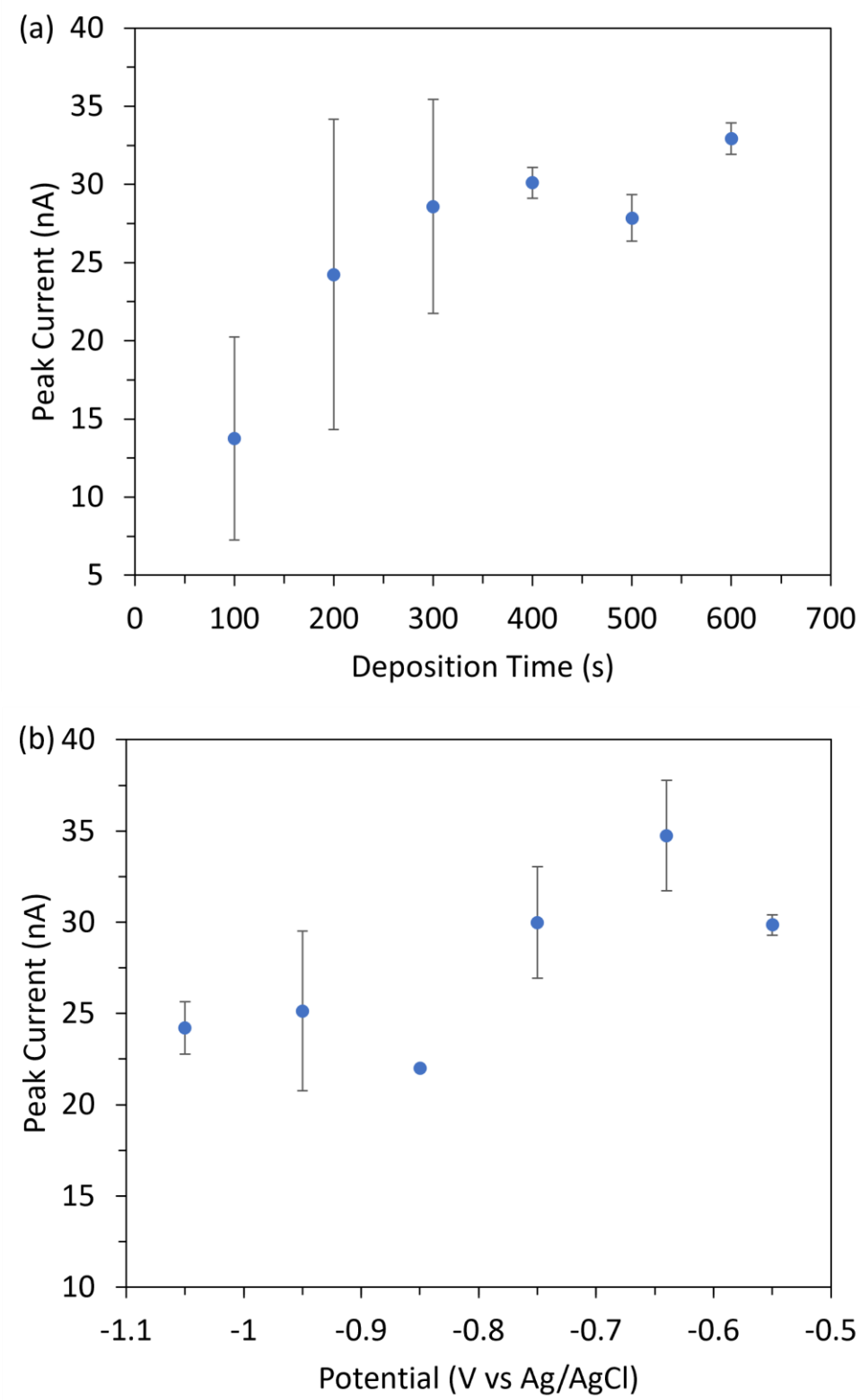


Figure 3.13 SWV peak current responses for 10 ppb Lead Nitrate in 0.1 M Acetate Buffer pH 4.6 for (a) deposition at -0.75 V vs Ag/AgCl (sat. KCl) with varied time and (b) deposition for 300 s with varied deposition potential at NPG-modified 3 µm gold IDEs with a 3 µm inter-electrode gap. Each measurement was carried out in triplicate with a new array used for each measurement.

Using the optimised conditions for the detection of lead in acetate buffer at IDEs, the resulting square wave stripping voltammograms can be seen in Figure 3.14. The lead stripping peak emerges at ~ -0.15 V and the peak current increases linearly with increasing concentration of lead.

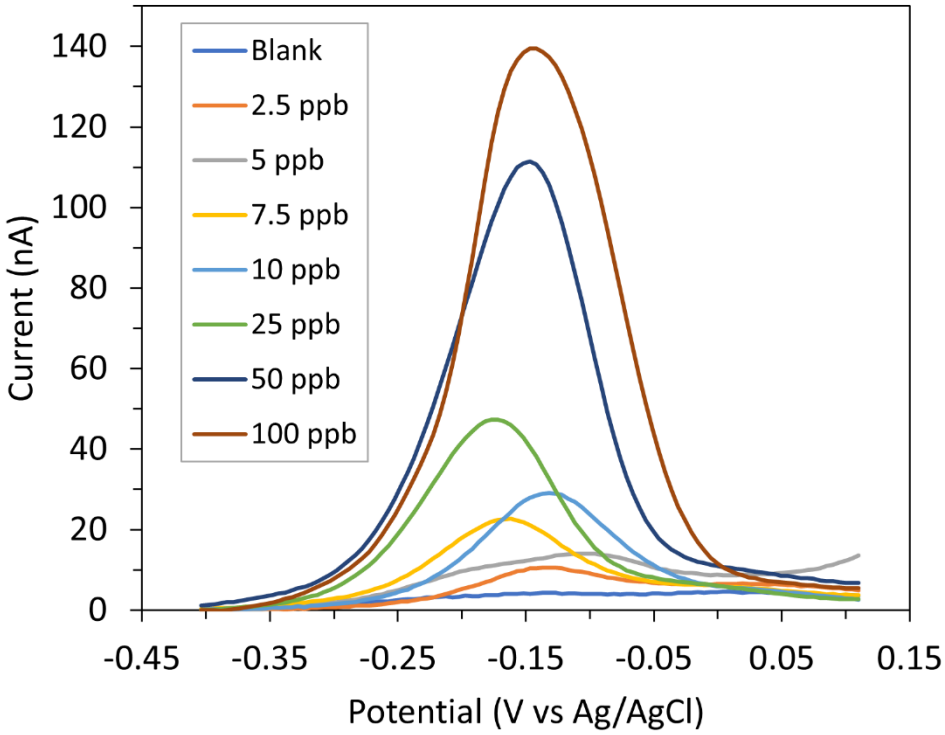


Figure 3.14 SWV for lead nitrate in 0.1 M acetate buffer pH 4.6 at NPG-modified 3 µm gold IDEs with a 3 µm inter-electrode gap. Each measurement was carried out in triplicate with a new array used for each measurement.

The lead stripping peak currents were plotted in calibration plots, as seen in Figure 3.15. The R^2 value obtained for the calibration plot in the range 0 to 100 ppb was 0.9392. Again, improved linearity (R^2 = 0.9951) is seen when focusing on the range of most interest, the 0 to 10 ppb range. As with the MDAs, a tapering off of the lead peak current was seen for concentrations above this range resulting in the decreased R^2 value. The results for 0 to 100 ppb lead in acetate buffer at IDEs can be seen in Figure 3.15. Based on the equation of the line obtained from Figure 3.15 (b), the LOD was found to be 0.43 ppb.[11]

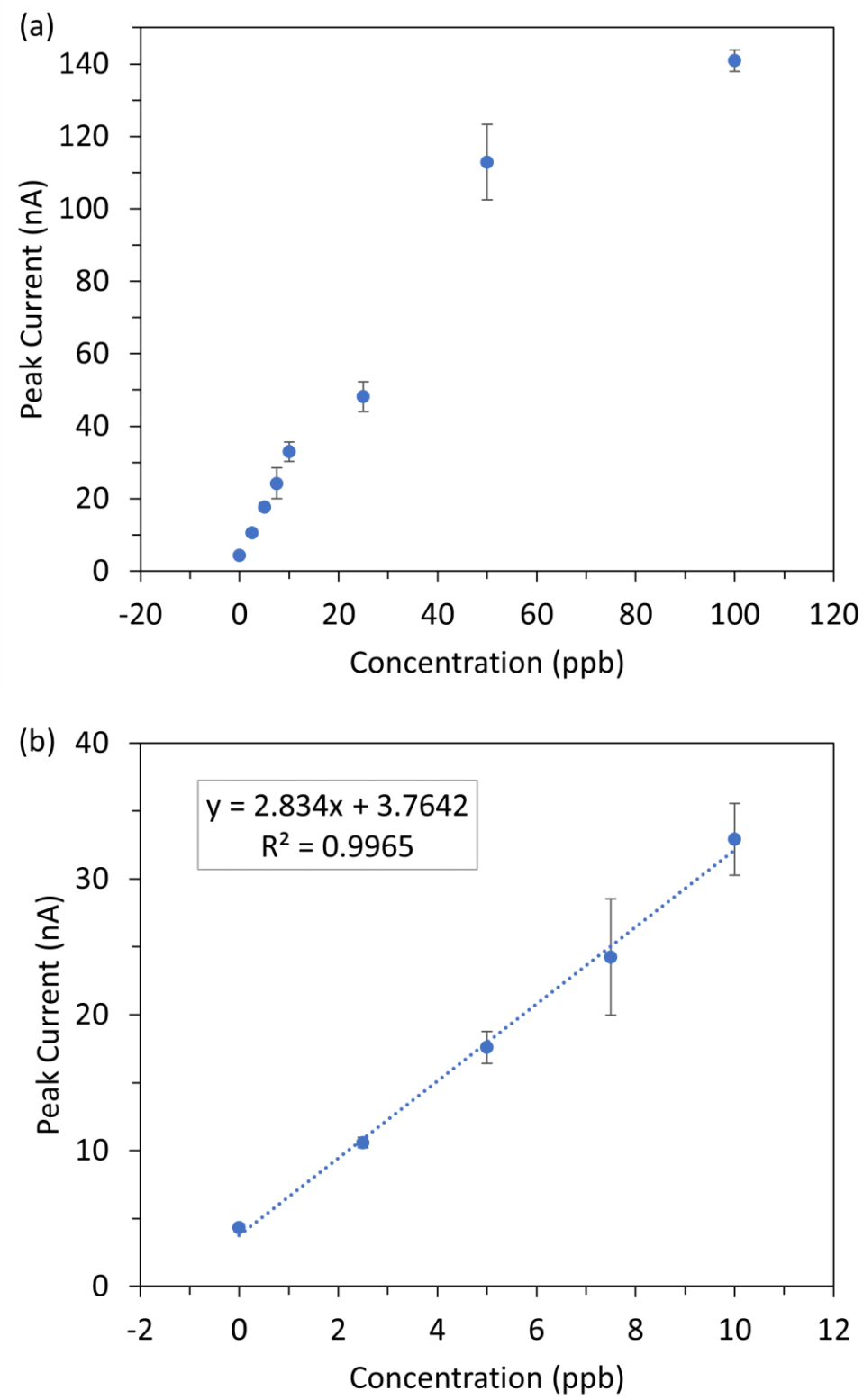


Figure 3.15 Calibration plots of lead peak stripping current at NPG-modified interdigitated electrodes arrays for (a) 0 to 100 ppb and (b) 0 to 10 ppb. Each measurement was carried out in triplicate with a new array used for each measurement.

3.3.2.2 *Lead Analysis in Tap Water*

NPG modified IDEs were also tested in tap water with lead(II) nitrate concentrations in the range 0 to 100 ppb. These results were compared with those obtained in acetate buffer pH 4.6, as can be seen in Figure 3.16. Here it can be seen that the currents obtained for analysis of lead in tap water are greatly reduced compared to those in buffer. Additionally, a distinguishable peak for lead does not emerge until between 50 to 100 ppb, as opposed to 2.5 ppb in buffer. The reduction in performance of the detection of lead in tap water compared to buffer can be mainly attributed to the increase of pH. Reduction in lead stripping current has been reported in literature for high pH values (above pH 6). The reduction in current is a result of hydrolysis, where the lead is converted to $[Pb(OH)]^{+}$, $[Pb_3(OH)_4]^{2+}$, $Pb_3(OH)_5]^{+}$, $Pb_4(OH)_4]^{4+}$, or $Pb_6(OH)_8]^{4+}$.[3, 4, 6, 23]

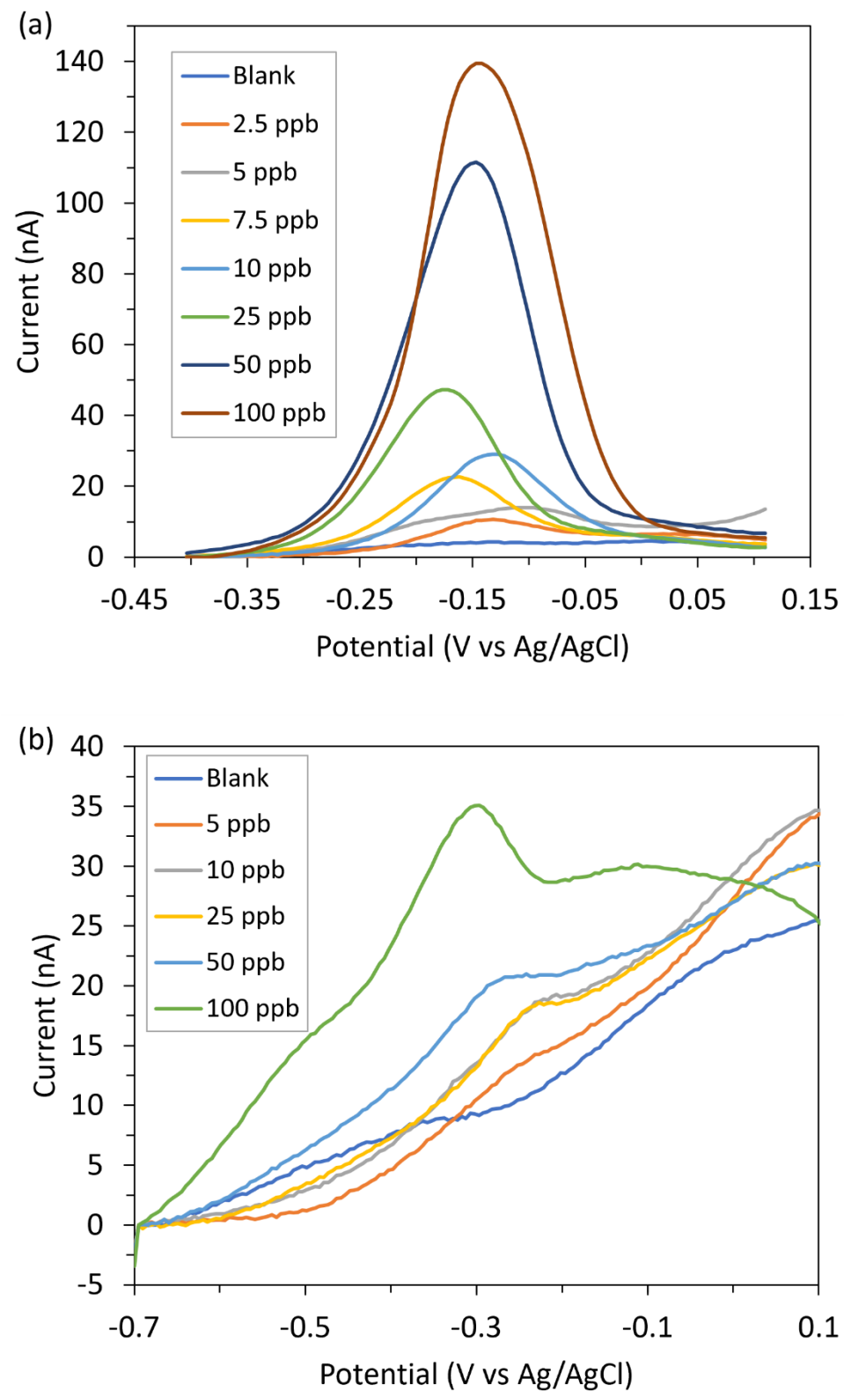


Figure 3.16 Square wave stripping voltammograms of for varied concentrations of lead nitrate at NPG modified gold interdigitated electrode arrays in (a) 0.1 M acetate buffer pH 4.6 and (b) tap water. Each measurement was carried out in triplicate with a new array used for each measurement.

The calibration data from the graphs outlined in Figure 3.16 are shown below in Figure 3.17. This comparison easily illustrates the improvement in analysis results in a pH-controlled buffer solution compared to tap water of a neutral pH. Also clearly highlighted here is the increase in background current for tap water compared to acetate buffer pH 4.6 recorded from the blank solutions. Increased background currents are evidence of background reactions occurring that further complicate the ability to detect lead in tap water. In tap water the background currents are often a result of dissolved oxygen reduction which occurs around -0.4 V.

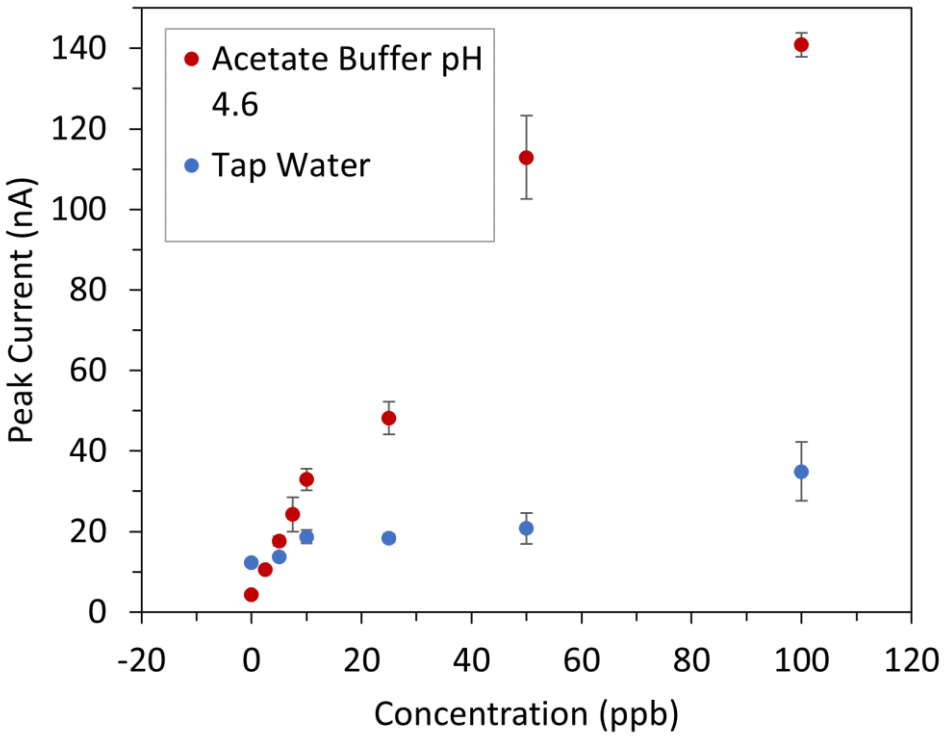


Figure 3.17 Calibration plot of the lead stripping peak current versus varied lead concentrations using NPG modified IDE arrays in acetate buffer pH 4.6 (red) and tap water (blue). Each measurement was carried out in triplicate with a new array used for each measurement.

The effect of pH can also be seen in the lead stripping peak potentials. As the pH of the solution increases, the stripping peak potential becomes more negative. This is highlighted in Figure 3.18, where the peak current for a 100 ppb lead samples occurs at -

0.15 V in a solution that is pH 4.6 and the potential shifts to -0.3 V for the sample in tap water which is pH 7. This difference in potential with pH shift is in accordance with the expected Nernstian 59 mV/pH unit shift.[24]

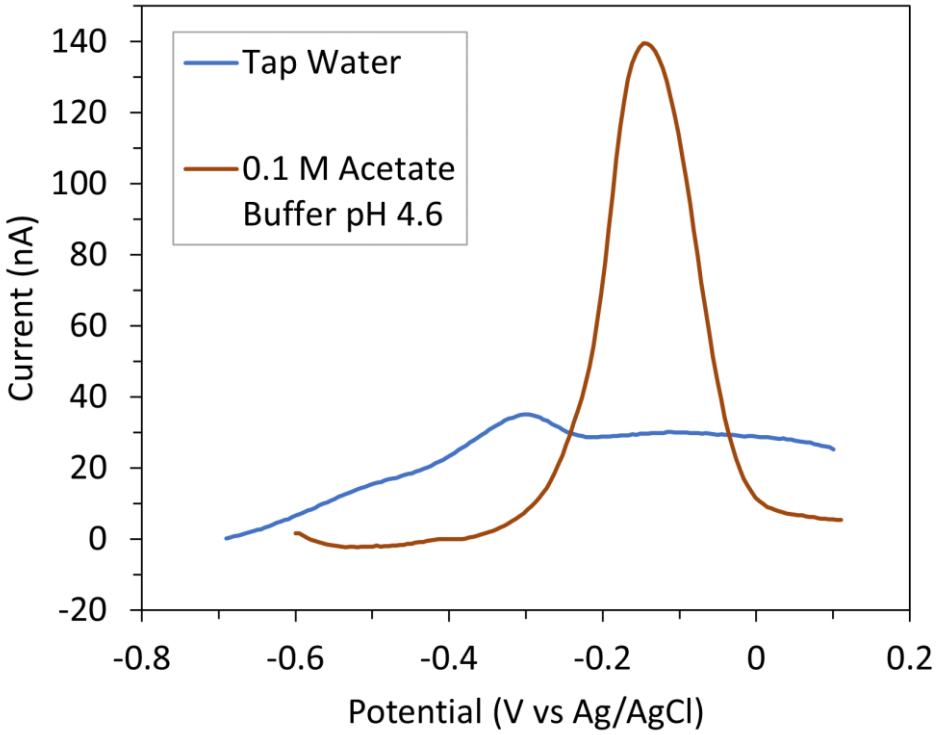


Figure 3.18 Square wave stripping voltammograms of for 100 ppb lead nitrate at NPG-modified interdigitated electrode arrays in 0.1 M acetate buffer pH 4.6 and tap water. Each measurement was carried out in triplicate with a new array used for each measurement.

3.4 Conclusions

The results from this chapter give insight into the electrochemical detection of lead at microelectrodes. It was established that at concentrations below 100 ppb, deposition and stripping is solely attributed to UPD lead. This is advantageous to the reusability of the sensor and reduces the need for mechanical or electrochemical pre-treatment of the electrodes. Modification of gold micro-disc arrays with NPG resulted in an increase in the electrochemically active surface area by approximately 9 times. Subsequently it was found that these modified arrays gave a 1.5 times current amplification over planar gold arrays due to the increase in surface area, electrocatalytic activity and conductivity because of NPG modification. It is believed that the current amplification does not match the amplification based on the surface area for several reasons. Firstly, the increased electroactivity of NPG makes it more susceptible to competing reactions prevent such as hydrogen evolution and oxygen reduction, which also limits the benefit of the increased surface area. Sukeri and Bertotti[13] reported on the notable electrocatalytic activity of a NPG film electrode for the hydrogen evolution reaction (HER) in terms of the low onset potential and overpotential and large cathodic current density. The performance observed for HER was comparable to platinum. Secondly, as the lead is deposited on the NPG structure it may not penetrate entirely into the interior of the pores therefore the full effect of the increased internal NPG surface area may not be realised. Application of NPG modified micro-disc and IDE arrays to a range of lead concentrations in 0.1 M acetate buffer pH 4.6 saw excellent linearity and reproducibility. The linear range was established in the 0 to 10 ppb range (R^2 = 0.991) and the limit of detection was found to be 0.32 ppb. The detection of lead transferred well to NPG modified IDE arrays, again excellent linearity and reproducibility were seen, a linear range was established between 0 to 10 ppb (R^2= 0.9951) and the limit of detection was found to be 0.43 ppb. A decline in the

performance of the arrays was observed when used in samples of tap water, where a discernible peak was not observed until 50 ppb. The decline in performance is attributed to the higher pH of tap water. Other factors affecting the performance for the detection of lead in tap water include low conductivity, and the presence of organic carbon and other species that may react and form insoluble lead compounds.[25] A strategy to electrochemically control the pH of tap water analysis with IDEs will be discussed in the following chapter.

3.5 References

1. Ji, C.; Searson, P. C., Synthesis and Characterization of Nanoporous Gold Nanowires. *The Journal of Physical Chemistry B* **2003**, 107, 4494-4499.

2. Nagle, L. C.; Wahl, A.; Ogourstov, V.; Seymour, I.; Barry, F.; Rohan, J. F.; Mac Loughlin, R., Electrochemical Discrimination of Salbutamol from Its Excipients in VentolinTM at Nanoporous Gold Microdisc Arrays. *Sensors* **2021**, 21, 3975.

3. Xu, X.; Duan, G.; Li, Y.; Liu, G.; Wang, J.; Zhang, H.; Dai, Z.; Cai, W., Fabrication of Gold Nanoparticles by Laser Ablation in Liquid and Their Application for Simultaneous Electrochemical Detection of Cd2+, Pb2+, Cu2+, Hg2+. *ACS Applied Materials & Interfaces* **2014**, 6, 65-71.

4. Cheng, Y.-m.; Fa, H.-b.; Yin, W.; Hou, C.-j.; Huo, D.-q.; Liu, F.-m.; Zhang, Y.; Chen, C., A sensitive electrochemical sensor for lead based on gold nanoparticles/nitrogen-doped graphene composites functionalized with l-cysteine-modified electrode. *Journal of Solid State Electrochemistry* **2016**, 20, 327-335.

5. Cheng, Y.; Sun, F.; Lee, J.; Shi, T.; Wang, T.; Li, Y. Gold-nanoparticles-graphene modified glassy carbon electrode for trace detection of lead ions. In E3S Web of Conferences, 2019; EDP Sciences: 2019; Vol. 78; p 03007.

6. Xiong, W.; Zhou, L.; Liu, S., Development of gold-doped carbon foams as a sensitive electrochemical sensor for simultaneous determination of Pb (II) and Cu (II). *Chemical Engineering Journal* **2016**, 284, 650-656.

7. Li, Y.; Liu, J.; Yu, F.; Tang, H.; Zhao, F.; Ye, B.-C.; Chen, W.; Lv, X., Electrochemical determination of trace lead(II) with enhanced sensitivity and selectivity by three-dimensional nanoporous gold leaf and self-assembled homocysteine monolayer. *Journal of Electroanalytical Chemistry* **2015**, 758, 78-84.

8. Herzog, G.; Arrigan, D. W., Determination of trace metals by underpotential deposition–stripping voltammetry at solid electrodes. *TrAC Trends in Analytical Chemistry* **2005**, 24, 208-217.

9. Martínez-Paredes, G.; González-García, M. B.; Costa-García, A., In situ electrochemical generation of gold nanostructured screen-printed carbon electrodes. Application to the detection of lead underpotential deposition. *Electrochimica Acta* **2009**, 54, 4801-4808.

10. Bonfil, Y.; Brand, M.; Kirowa-Eisner, E., Characteristics of subtractive anodic stripping voltammetry of Pb and Cd at silver and gold electrodes. *Analytica chimica acta* **2002**, 464, 99-114.

11. Patella, B.; O'sullivan, B.; Daly, R.; Lovera, P.; Inguanta, R.; O'Riordan, A., Simultaneous detection of copper, lead and mercury in river water with in-situ pH control using electrochemical stripping techniques. **2020**.

12. Lu, X.; Yu, T.; Wang, H.; Qian, L.; Lei, P., Electrochemical fabrication and reactivation of nanoporous gold with abundant surface steps for CO2 reduction. *ACS Catalysis* **2020**, 10, 8860-8869.

13. Sukeri, A.; Bertotti, M., Nanoporous gold surface: An efficient platform for hydrogen evolution reaction at very low overpotential. *Journal of the Brazilian Chemical Society* **2018**, 29, 226-231.

14. Pia, G.; Sogne, E.; Falqui, A.; Delogu, F., Ag surface segregation in nanoporous Au catalysts during CO oxidation. *Scientific Reports* **2018**, 8, 15208.

15. Wittstock, A.; Wichmann, A.; Biener, J.; Bäumer, M., Nanoporous gold: a new gold catalyst with tunable properties. *Faraday discussions* **2011**, 152, 87-98; discussion 99-120.

16. Fujita, T.; Guan, P.; McKenna, K.; Lang, X.; Hirata, A.; Zhang, L.; Tokunaga, T.; Arai, S.; Yamamoto, Y.; Tanaka, N.; Ishikawa, Y.; Asao, N.; Yamamoto, Y.; Erlebacher, J.; Chen, M., Atomic origins of the high catalytic activity of nanoporous gold. *Nature Materials* **2012**, 11, 775-780.

17. Castillo, E.; Xie, Y.; Dimitrov, N., Filling in nanoporous gold with silver via bulk deposition and surface-limited redox replacement approaches. *Electrochimica Acta* **2021**, 380, 138196.

18. Lu, Z.; Dai, W.; Liu, B.; Mo, G.; Zhang, J.; Ye, J.; Ye, J., One pot synthesis of dandelion-like polyaniline coated gold nanoparticles composites for electrochemical sensing applications. *Journal of Colloid and Interface Science* **2018**, 525, 86-96.

19. Bui, M.-P. N.; Li, C. A.; Han, K. N.; Pham, X.-H.; Seong, G. H., Simultaneous detection of ultratrace lead and copper with gold nanoparticles patterned on carbon nanotube thin film. *Analyst* **2012**, 137, 1888-1894.

20. Wan, H.; Sun, Q.; Li, H.; Sun, F.; Hu, N.; Wang, P., Screen-printed gold electrode with gold nanoparticles modification for simultaneous electrochemical determination of lead and copper. *Sensors and Actuators B: Chemical* **2015**, 209, 336-342.

21. Kanyong, P.; Rawlinson, S.; Davis, J., Gold nanoparticle modified screen-printed carbon arrays for the simultaneous electrochemical analysis of lead and copper in tap water. *Mikrochimica Acta* **2016**, 183, 2361-2368.

22. HSE Lead in Drinking Water. https://www.hse.ie/eng/health/hl/water/drinkingwater/lead/ (07/09/2021),

23. Sylva, R. N.; Brown, P. L., The hydrolysis of metal ions. Part 3. Lead(II). *Journal of the Chemical Society, Dalton Transactions* **1980**, 1577-1581.

24. Wang, J. Controlled-Potential Techniques. In *Analytical Electrochemistry*; 2006, pp 67-114.

25. Rahm, C. E.; Torres-Canas, F.; Gupta, P.; Poulin, P.; Alvarez, N. T., Inkjet Printed Multi-Walled Carbon Nanotube Sensor for the Detection of Lead in Drinking Water. *Electroanalysis* **2020**, n/a.

Chapter 4 Electrochemical *In Situ* pH Control for the Detection of Lead in Water

4.1 Introduction

This chapter explores the use of the IDE arrays designed in Chapter 2 for the analysis of lead in tap water with electrochemical pH control. pH control is essential for the detection of lead as highlighted in the previous chapter. The process by which the pH is changed electrochemically at the electrode surface is a very fast process. Work carried out by Lee et. al. calculated that the experimental diffusion coefficient of protons is 9.31 x 10^{-5} cm^2 s^{-1}. The inter-electrode gap is also important to know for determining how fast electrochemical pH control is established. In this work the IDE arrays used have a 3 µm inter-electrode gap. Modifying the calculation for diffusion layer thickness gives the equation:

$$\frac{\delta^2}{\pi D} = t$$

4.1

From this equation it was calculated that the protons will diffuse far enough to encapsulate the sensing electrode 3 µm away in 0.01 seconds.

The potential at which to hold the protonator electrode to induce a specific potential was established by exploiting the pH dependence of the gold oxide peak. The gold oxide reduction peak has been shown recently to function as a probe to determine the local pH conditions in the vicinity of microelectrodes.[1-4] In acidic conditions the gold oxide reduction peak is well-documented and is known to occur at 1.18 V vs RHE in 1 M H_2SO_4.[5]

$$Au + 3H_2O = Au_2O_3 + 6H^+ + 6e^-$$

4.2

In alkaline conditions, 1 M NaOH, the gold oxide reduction peak occurs at approximately 1.07 V vs RHE, which correspond to approximately 0.05 V vs Ag/AgCl (sat. KCl).[5, 6] The relationship between the gold oxide reduction peak and pH follows near Nernstian behaviour with a 60 to 70 mV shift per pH unit.[3] Slight deviations from Nernstian behaviour can be attributed to the extent of oxide formation which can differ over a similar potential range in solutions of the same pH.

A review of literature highlighted work carried out by Patella et. al. have utilised electrochemical pH control in the detection of lead in river water samples.[7] Gold IDE arrays of 1 µm in width with a 2 µm inter-electrode gap were applied to the detection of lead in river water where the protonator was held at 1.74 V to induce a local pH at the IDE arrays of pH 3.5. The lowest detectable lead concentration achieved was 100 ppb. Herein we applied this technique to detection of lead in water samples collecting from Tyndall National Institute using gold IDE arrays that are 3 µm wide with a 3 µm inter-electrode gap. The results showed good linearity (R^2 = 0.9959) in the range of 0 ppb to 100 ppb. The lowest detectable lead concentration was 10 times lower than achieved in literature with 10 ppb being the lowest concentration detected for the analysis carried out in this thesis.

4.2 Experimental

4.2.1 Electrode Design and Fabrication

The electrodes were designed and fabricated as outlined in 2.2.2. The IDE array dimensions used for this chapter were 3 µm wide bands with a 3 µm inter-electrode gap.

4.2.2 Electrochemical Cell Set-up, Microscopic and Electrochemical Analysis

As outlined in 3.2.2.

4.2.3 Electrode Modification with Nanoporous Gold

The IDE arrays were modified with NPG as outlined in 3.2.3.

4.2.4 Electrochemical Detection of Lead

The detection of lead was carried out as described in 3.2.4. Some differences apply here in that rather than using 0.1 M acetate buffer pH 4.6, initial tests were carried out in tap water which was chemically modified to pH 4.6 with sodium acetate and acetic acid. Subsequently, unmodified tap water was used where the pH was electrochemically controlled by the application of a potential to the protonator electrode.

4.2.5 pH Adjustment of Water Samples

Artificial drinking water (ADW) was used to assess pH control at the IDE arrays. The ADW was prepared by dissolving 1 g of sodium bicarbonate, 65.4 mg of magnesium sulphate (sigma Aldrich, 99.5% anhydrous), 341.4 mg of calcium sulphate dehydrate (Honeywell, 99%0, 7 mg potassium phosphate dibasic (Fluka, 98%), potassium phosphate monobasic (Sigma Aldrich, 99%) and 10 mg sodium nitrate (Sigma Aldrich,

99%) in 10 l of deionised water. The preparation of ADW was based on work carried out by Seymour et. al.[1, 3, 4] To monitor the shift in the gold oxide reduction peak with pH, CVs were carried out at planar gold IDE arrays where the sensing electrode was swept from 0 V to 1.5 V while the protonator was left unbiased in the ADW samples. H_2SO_4 was added to the ADW samples to adjust the pH. CVs at each pH value were carried out in triplicate.

Tap water sourced from Tyndall was chemically adjusted to pH 4.6 by adding 405.86 mg of sodium acetate (Sigma Aldrich, 99%) and 303.4 mg of acetic acid (Sigma Aldrich, 99%) to 100 ml tap water.

4.2.6 Electrochemical *In Situ* pH Control

In situ pH control was established by biasing the protonator electrode at a positive potential, a range of protonator potentials was investigated from 1.35 V to 1.75 V. The effect of pH control was demonstrated in ADW and tap water samples where CVs were carried out at the sensing electrode as described previously in 4.2.5, while the protonator was held at one at a potential in the aforementioned range. This technique was also applied to the detection of lead in water samples where lead deposition and stripping was carried out at the sensing electrode while the protonator was held at a constant potential.

4.3 Results and Discussion

4.3.1 Monitoring pH Based on the Potential of the Gold Oxide Reduction Peak

Slight deviations from Nerstian behaviour can be attributed to the extent of oxide formation which can differ over a similar potential range in solutions of the same pH. To monitor the gold oxide reduction peak, the potential is first swept to a positive potential such as 1.5 V to form the gold oxide. In the reverse scan, the gold oxide is reduced, and the potential of this peak corresponds to the pH of the solution. A series of pH buffers were used, the results for which can be seen in Figure 4.1 (a). An increase of gold oxide reduction potential was observed with decreasing solution pH as expected. The gold oxide reduction peak potentials were plotted versus solution pH, and the resulting calibration plot is shown in Figure 4.1(b). The calibration plot indicated a linear relationship between the gold oxide reduction potential and solution pH ($R^2 = 0.9407$). Each measurement was carried out in triplicate and found to be highly reproducible, as highlighted by the negligible error bars in Figure 4.1(b). Also highlighted by the calibration plot is the gold oxide reduction potential shift with pH which was found to be 80.5 mV/pH based on the slope of the linear fit. This shift shows a deviation from the expected Nernstian behaviour which may be due to the fixed upper limit used for the formation of oxide in the solutions of varying pH. [3]

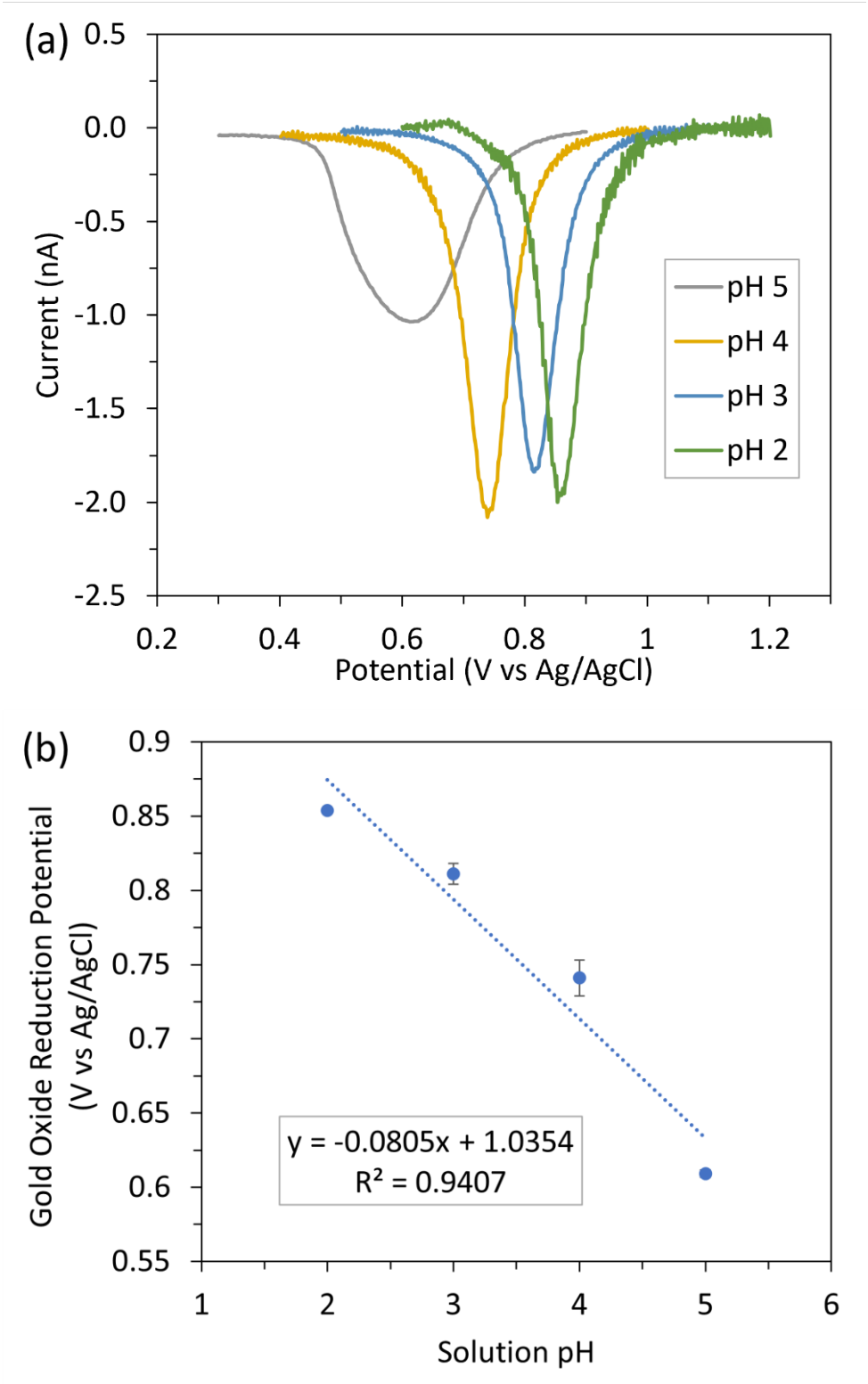


Figure 4.1 (a) The gold oxide reduction peak in CVs recorded from 0.0 V to 1.5 V vs Ag/AgCl (sat. KCl) at 50 mV s^{-1} at gold IDE arrays in a series of pH buffers. For these scans, only one side of the IDE array was used, the other was left unbiased. (b) Calibration plot of gold oxide reduction peak vs. solution pH.

4.3.2 Establishing Protonator Potential for *In Situ* pH Control

The position of the gold oxide reduction peak is a useful proxy to estimate the pH at electrodes. Tests were carried at gold IDE arrays where the sensing electrode was swept from 0.0 V to 1.5 V, during which gold oxide was formed. The gold oxide was subsequently reduced as the potential was swept back to 0 V. During the CV the protonator electrode was biased at various potentials. The resulting gold oxide reduction peaks were recorded and using the calibration plot established in Figure 4.1(b), the pH at each protonator potential was estimated. As the protonator potential increased from 1.45 V to 1.75 V, the gold oxide reduction potential also increased, as seen in Figure 4.2(a). This indicates that as the protonator potential increases the pH at the sensing electrodes becomes more acidic. The estimated pH environments created based on the protonator potentials were plotted against the corresponding gold oxide reduction peak for each protonator potential, see Figure 4.2(b). It was found that the relationship between pH and increasing protonator potential was linear ($R^2 = 0.8786$). As with the calibration plot from Figure 4.1(b), the potential shift per pH unit can be established by the slope of the plot. For Figure 4.2(b) the slope was found to be 62.8 mV/pH. Again, this deviates from the expected Nernstian behaviour. As mentioned previously, it is suspected that the reason for the is the fixed upper limit throughout the CVs.[3] A review of literature highlighted that the optimum pH for the detection of lead at gold electrodes was in the range of pH 3.5 to pH 5.[7-12] Therefore a protonator potential of 1.55 V was chosen as this corresponds to pH 4.

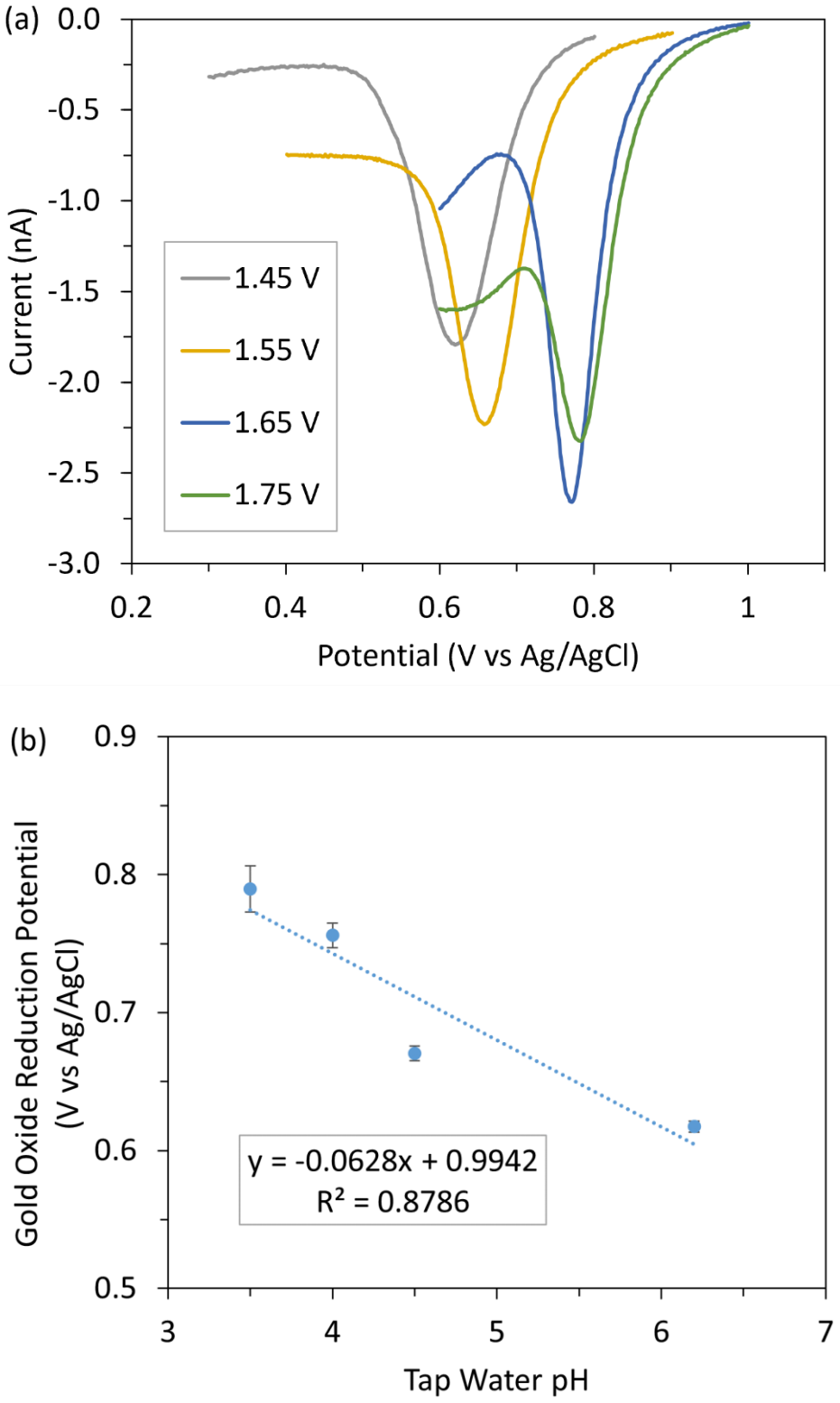


Figure 4.2 (a) The gold oxide reduction peak in CVs recorded from 0.0 V to 1.5 V at 50 mV s^{-1} at gold IDE arrays in artificial drinking water At the opposing side of the array, the protonator, the potential was biased at various potentials to electrochemically impose a local pH change at the IDE arrays. (b) Calibration plot of gold oxide reduction peak potential vs. solution pH.

The protonator potential was assessed in a sample of unmodified tap water. CVs were carried out where the sensing electrode was swept from 0.0 V to 1.5 V while the protonator was initially left unbiased and was subsequently held at 1.55 V, as shown in Figure 4.3. Here it can be seen that application of 1.55 V to the protonator shifts the gold oxide potential from 0.31 V to 0.65 V. Using the calibration plot established in Figure 4.1(b) it is estimated that this corresponds to a shift in pH from approximately 6.8 to 4.

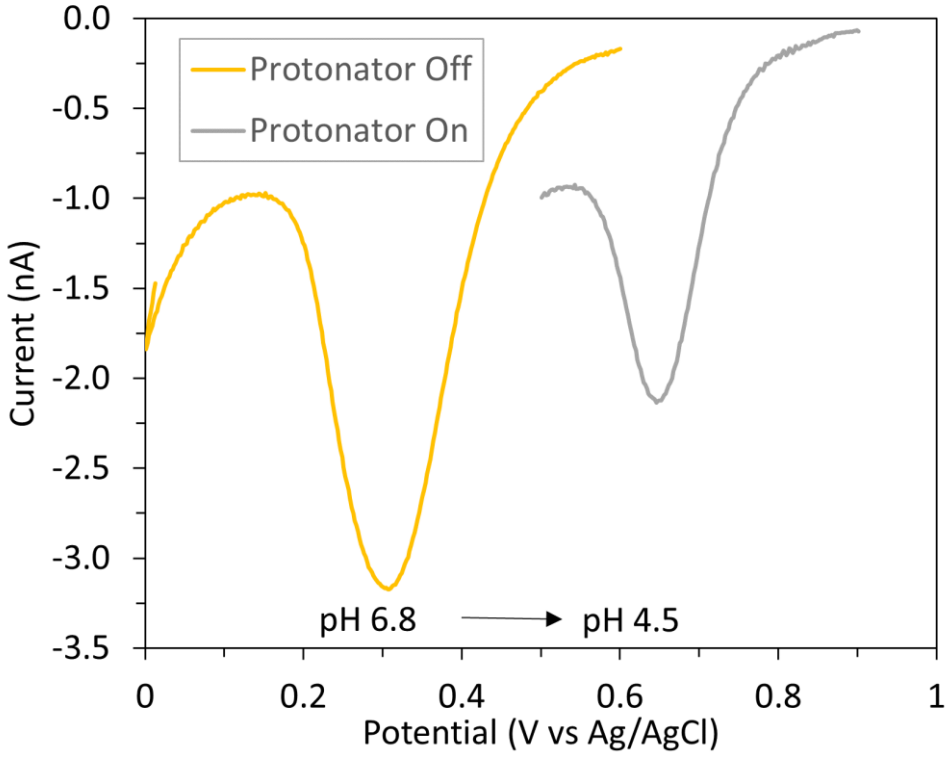


Figure 4.3 The gold oxide reduction peaks in tap water in CVs recorded from 0.0 V to 1.5 V vs Ag/AgCl (sat. KCl) at 50 mV s^{-1} at gold IDE arrays while the protonator was initially left unbiased and then held at 1.55 V vs Ag/AgCl (sat. KCl).

Since the pH of tap water can vary, the reliability of the pH generated from holding the protonator at 1.55 V was also investigated in samples with different starting potentials. CVs as described above were carried out in artificial drinking water (pH 7.5) and tap water (pH 6.8). In both cases the application of 1.55 V at the protonator created a local pH of approximately pH 4 at the arrays. The results for this are summarised in Table 4.1.

and the difference between the two starting pH values is 0.7 pH. The resulting gold oxide reduction peak potential from holding the protonator at 1.55 V only deviated by 7 mV.

Table 4.1 Summary of results for in situ pH control in water samples of varying pH

Solution	**pH**	**Gold Oxide Reduction Potential with Protonator at 1.55 V**
	[pH]	[V]
Artificial Drinking Water	7.5	0.661
Tap Water	6.8	0.654

The use of NPG modifications on the IDE arrays was optimised in Chapter 3 for the analysis of lead. It was intended to be used in this chapter with the electrochemical pH control analysis however, there appears to be some complication with the NPG modification that inhibits the use of electrochemical pH control. Figure 4.4 shows the gold oxide reduction peaks under the same conditions as shown in Figure 4.3. Here it can be seen that the pH change induced by a protonator potential of 1.55 V is small in comparison to planar gold which reacts as one would expect when a positive protonator potential is applied. This phenomenon was only seen with electrochemical pH control as when the pH was chemically changed the NPG gold oxide reduction peak shifted to match the peak seen at planar gold. The reason for the lack of electrochemical pH control at NPG modified IDE arrays is yet unknown. Further electrochemical and surface analysis is required to determine to full extent of what is occurring at NPG during the attempts at electrochemical pH control.

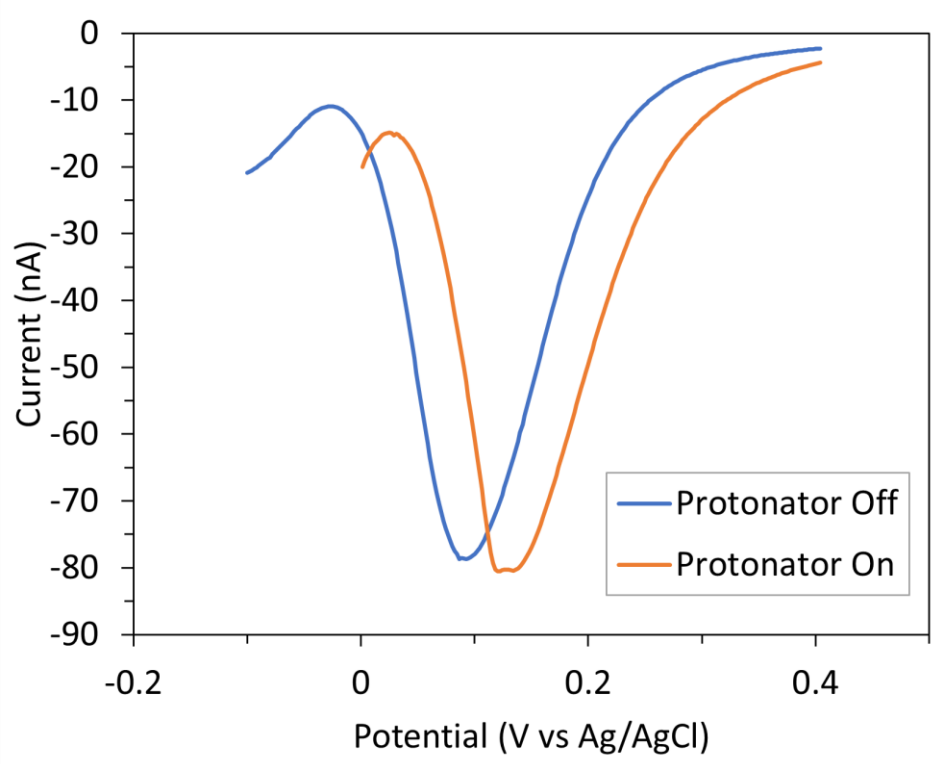


Figure 4.4 The gold oxide reduction peaks in tap water in CVs recorded from 0.0 V to 1.5 V vs Ag/AgCl (sat. KCl) at 50 mV s^{-1} at NPG modified IDE arrays while the protonator was initially left unbiased and then held at 1.55 V vs Ag/AgCl (sat. KCl).

4.3.3 Detection of Lead in Tap Water with Chemical pH Control

Initial tests for detection of lead in tap water were carried out in tap water where the pH was chemically controlled. Here acetic acid and sodium acetate were added to tap water to adjust the pH to pH 4.6. The optimum deposition and stripping conditions which were established for IDEs in Chapter 3 were used here and all measurements were carried out in triplicate. The protonator electrodes were left unbiased during this analysis. The concentration range tested was 0 ppb to 100 ppb and the resulting lead stripping peaks can be seen in Figure 4.5(a). Here it can be seen that the lead peak emerges at -0.15 V which is in good agreement with the results seen for the detection of lead in acetate buffer pH 4.6 shown in Chapter 3. However, here the lowest discernible peak is observed at 5 ppb, whereas lead in acetate buffer could detect as low as 2.5 ppb. The lead peak currents were plotted against the lead concentration of the samples, and it was found the peak

increases linearly in the range 10 to 100 ppb ($R^2 = 0.9396$) as shown in Figure 4.5(b). The LOD was found to be 2.18 ppb, which was calculated as shown in chapter 3.

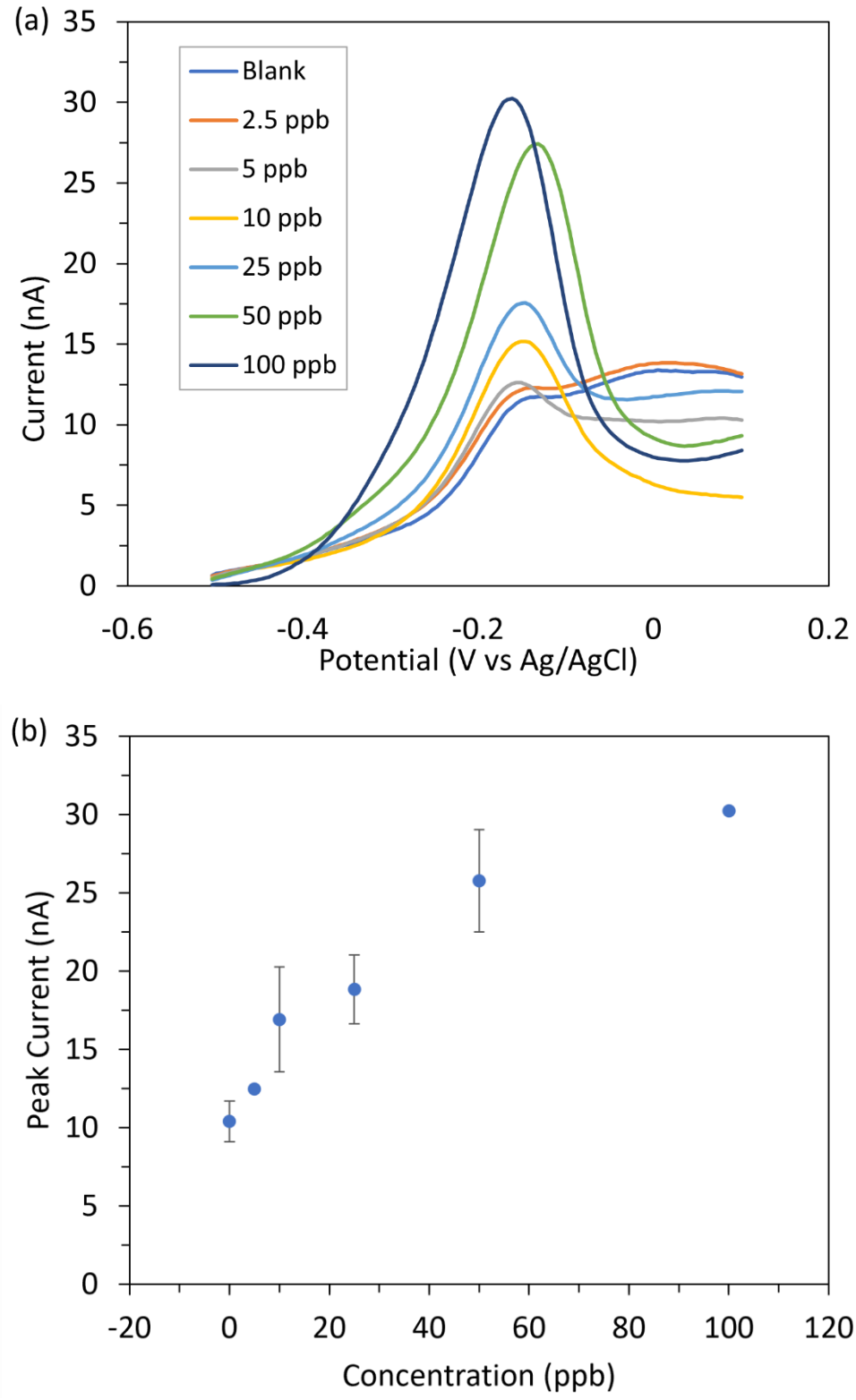


Figure 4.5 (a) Square wave stripping voltammogram for varied concentration of lead nitrate in tap water pH 4.6 at NPG-modified IDE arrays. (b) Calibration plot of lead stripping peak current vs. lead concentration.

4.3.4 Detection of Lead in Tap Water with Electrochemical *In Situ* pH Control

Subsequent tests were carried out in unmodified tap water samples, relying on the protonator electrode to electrochemically adjust the pH of the tap water for optimum lead detection. For these tests, deposition and stripping of lead was carried out at the sensing electrode while the protonator was held at 1.55 V. Planar gold IDE arrays were used for this work instead of previously used NPG-modified IDE arrays as it was found that electrochemical pH control was being inhibited at NPG modified arrays. It is believed that this is due to the increase in the influence of oxygen reduction and hydrogen evolution at NPG while performing electrochemical pH control in tap water. The resulting stripping peaks of lead for this work can be seen in Figure 4.6(a). Here results are shown for a concentration of 10 to 100 ppb. The position of the lead stripping peak has shifted to a more negative potential of -0.3 V compared to buffered solutions. This shift was also seen in the literature for in situ pH control for detection of lead in tap water.[7] A 1.8-fold reduction in current was noted when comparing the results to those obtained in NPG in tap water with chemically controlled pH. The lead peak currents were plotted against the lead concentrations, the resulting calibration plot can be seen in Figure 4.6(b). Here it was found that linearity in this concentration range was $R^2 = 0.9959$ and the LOD calculated based on the slope of the line was 11.6 ppb. The decrease in LOD achieved here compared to buffered solutions is believed to be due to complications created by oxygen reduction during the lead accumulation step. The oxygen reduction peak overlaps with the lead stripping peak as can be seen from the peak in the blank samples. The interference of the oxygen reduction peak is further enhanced by electrochemical pH control due to the nature of the water splitting reaction used to locally reduce the pH which produces

molecular oxygen which increases the oxygen concentration available for reduction to further limit the lead accumulation particularly at low ppb levels of lead.[7]

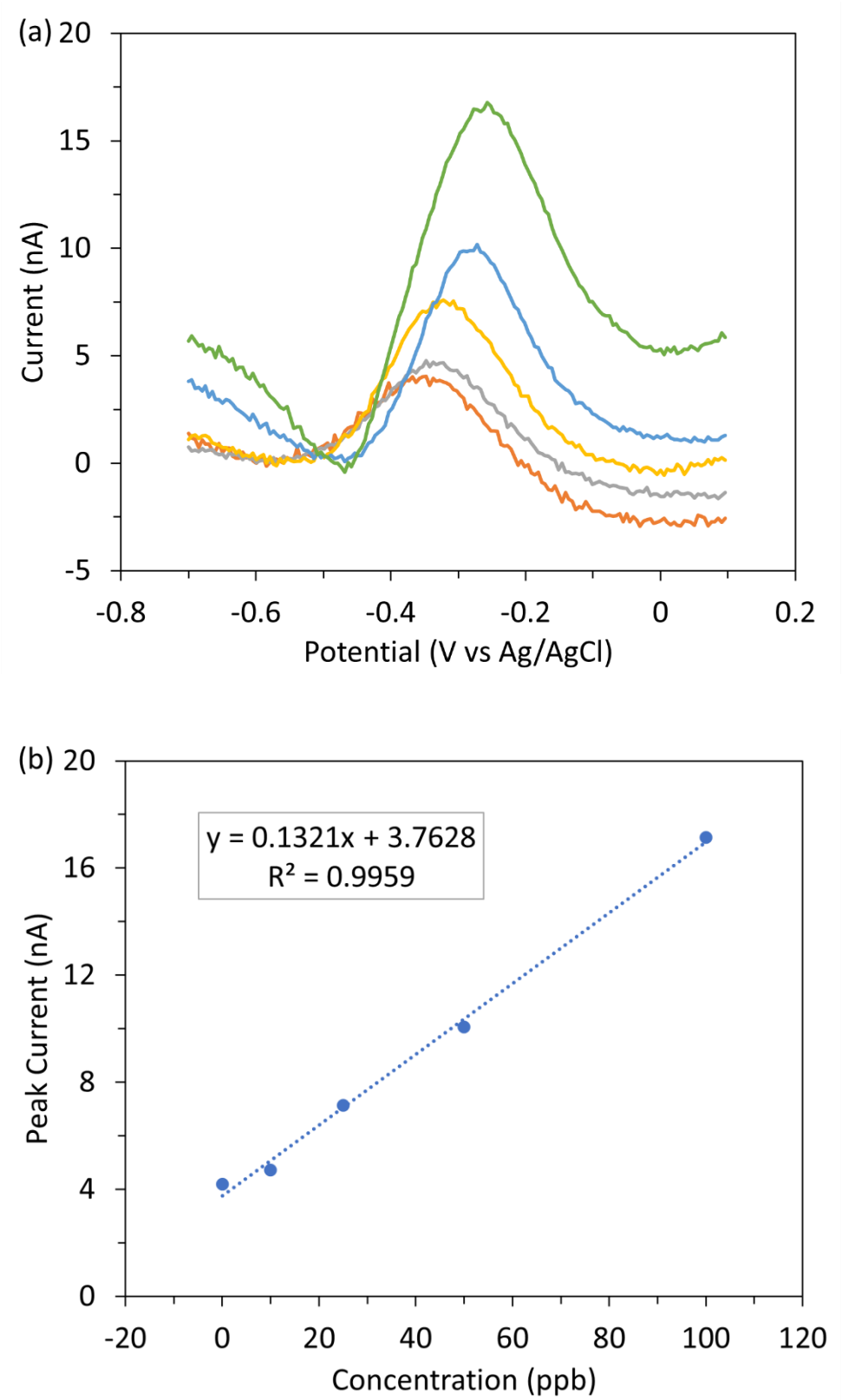


Figure 4.6 (a) Square wave stripping voltammogram for varied concentration of lead nitrate in unmodified tap water at gold IDE arrays where the protonator was held at 1.55 V. (b) Calibration plot of lead stripping peak current vs. lead concentration.

4.3.5 Reusability, Reproducibility and Ageing Study

To determine the reusability and reproducibility, analysis was carried out using 10 ppb lead samples, at different arrays on the same chip (inter-array analysis). Here the average peak current was found to be 6.94 ± 0.63 nA (n=8). The SWV voltammograms and subsequent plot of the lead peak currents showing these values can be seen in Figure 4.7 (a) and (b). In general, the reproducibility of the result was shown to be consistent, with 62.5% of the arrays tested exhibiting a stable peak current range. However, the study could benefit from a larger sample size to determine the full extent of reproducibility. The reusability was determined by repeating a measurement in a 10 ppb lead sample at the same array ten times (intra-array analysis). For this, the average peak current was found to be 10.1 ± 0.54 (n=10). The SWV voltammograms and subsequent plot of the lead peak currents showing these values can be seen in Figure 4.7 (c) and (d). For the reusability analysis, the peak current for the initial scan is lower and closer to the range of the inter-array peak current than the average peak current calculated for the intra-array analysis. Further analysis shows the peak current increasing and stabilising across the subsequent scans. A possible explanation for this is that changes in the electrode surface during the analysis are leading to increased peak current. Changes in the electrode surface area could be a result of roughening of the electrode surface or deposition of unidentified materials from tap water. A change in electrode surface is also reflected in the SWV voltammograms in Figure 4.7 (c) where a second peak is emerging from the primary lead peak. Further analysis is required to fully investigate the nature of the changes to the electrode surface following the detection of lead.

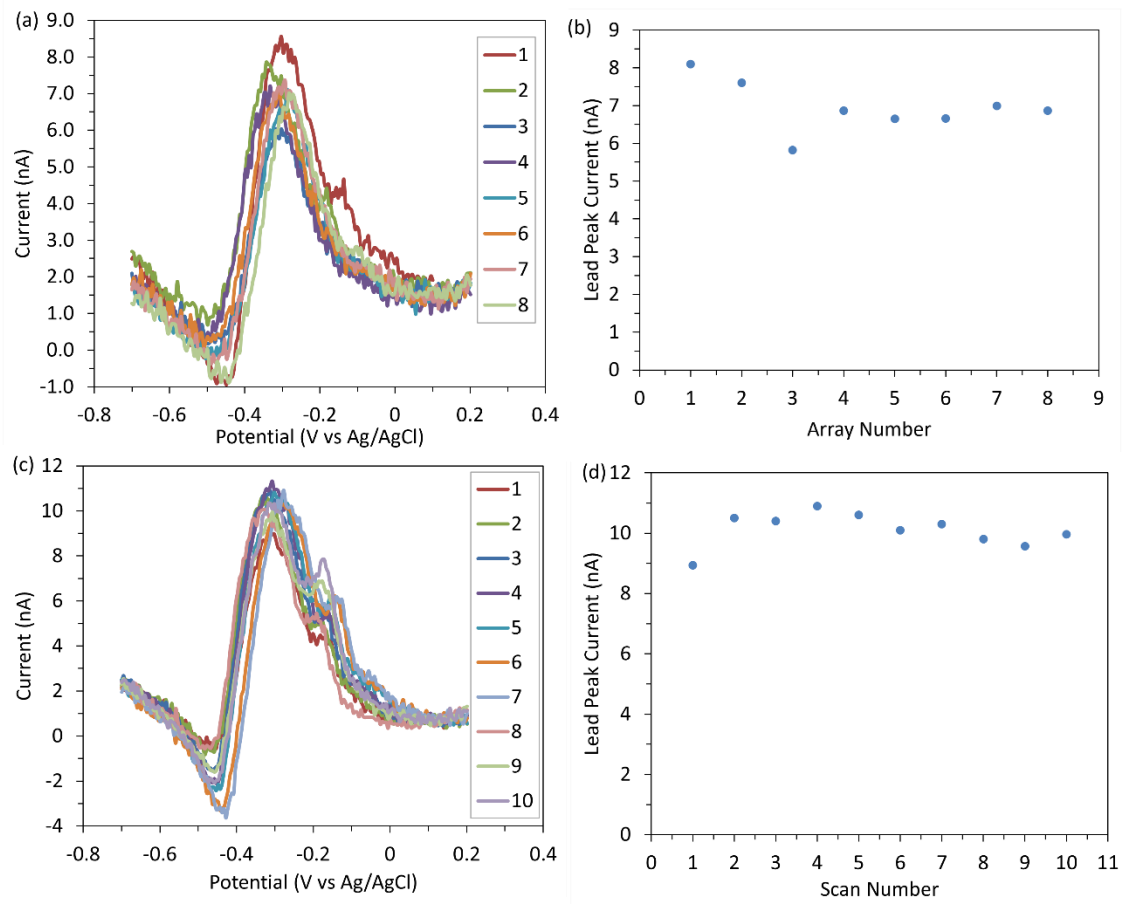


Figure 4.7 (a) Square wave stripping voltammograms for 10 ppb of lead nitrate in unmodified tap water at gold IDE arrays where the protonator was held at 1.55 V at 8 different arrays on the same chip. (b) Plot of lead stripping peak current vs. lead concentration for the lead peaks obtained in (a). (c) Square wave stripping voltammograms for 10 ppb of lead nitrate in unmodified tap water at gold IDE arrays where the protonator was held at 1.55 V at the same array where the measurement was repeated 10 times. (d) Plot of lead stripping peak current vs. lead concentration for the lead peaks obtained in (c).

An intra-array ageing study was carried out where measurements were taken 6 to 7 days apart. This analysis was demonstrated on two different arrays where one was aged in air, and one was aged in acetone. All the measurements were carried out in triplicate. While both arrays tested over the 21 days showed similar peak currents, it was found that the array aged in air had a higher deviation, and the SWV voltammograms showed the stripping peaks were more susceptible to noise and peak distortion. This could be due to surface oxidation and unwanted materials from tap water that can build up on the electrode surface when stored in air that are prevented by storing the array in acetone.

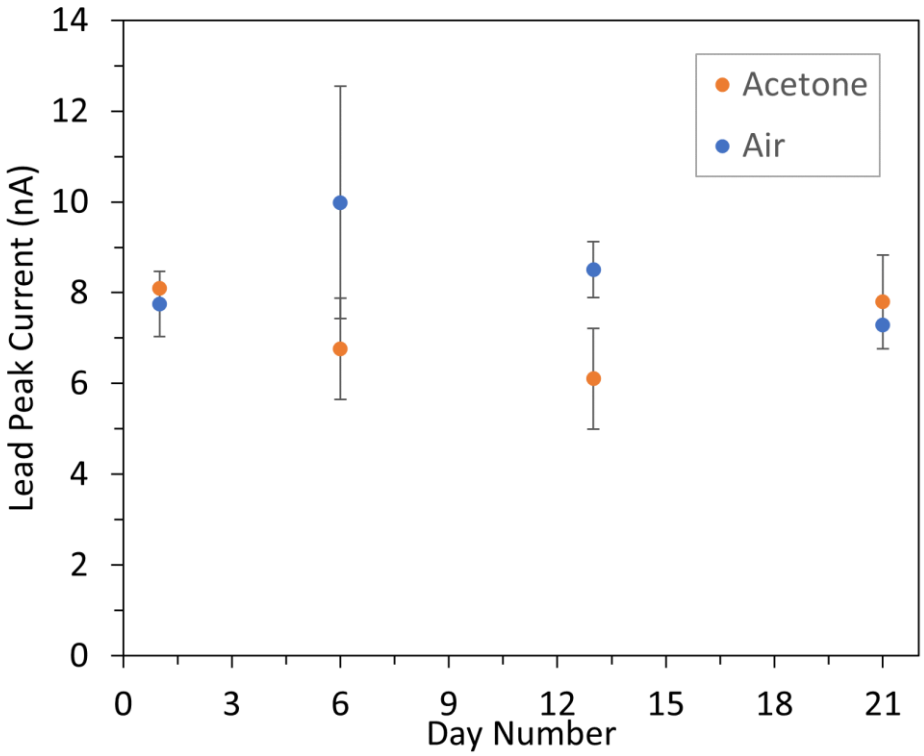


Figure 4.8 Plot of lead peak currents from SWV voltammograms following analysis in 10 ppb lead nitrate in tap water where the protonator was held at 1.55 V for arrays aged in acetone and air. Each measurement was carried out in triplicate at the same array.

4.4 Conclusions

This chapter has shown that electrochemical pH control is an effective approach for the detection of lead in tap water. Using the IDE arrays designed in Chapter 2, the local pH at the sensing electrode was lowered to pH 3 by holding the protonator electrode at the positive potential of 1.55 V. The potential at which the protonator needed to be held was established by exploiting the pH dependence of the gold oxide reduction peak. The use of electrochemical pH control in tap water samples allowed for the detection of lead as low as 10 ppb. This was 10 times lower than previous reports of the use of electrochemical pH control for the detection of lead in tap water in literature. This works shows the possibility of an electrochemical approach to reagent-free, at-source sensing of lead in tap water. Analysis carried out both inter- and intra-array show good reproducibility and reusability 6.94 ± 0.63 nA (n=8), and 10.1 ± 0.54 (n=10), respectively. Initial ageing studies show stable responses over a 21-day period, however, a more extensive ageing study is required to demonstrate full sensor lifetime.

4.5 References

1. O'Sullivan, B.; Patella, B.; Daly, R.; Seymour, I.; Robinson, C.; Lovera, P.; Rohan, J.; Inguanta, R.; O'Riordan, A., A simulation and experimental study of electrochemical pH control at gold interdigitated electrode arrays. *Electrochimica Acta* **2021**, 395, 139113.

2. Wasiewska, L. A.; Seymour, I.; Patella, B.; Inguanta, R.; Burgess, C. M.; Duffy, G.; O'Riordan, A., Reagent free electrochemical-based detection of silver ions at interdigitated microelectrodes using in-situ pH control. *Sensors and Actuators B: Chemical* **2021**, 333, 129531.

3. Seymour, I.; O'Sullivan, B.; Lovera, P.; Rohan, J. F.; O'Riordan, A., Electrochemical detection of free-chlorine in Water samples facilitated by in-situ pH control using interdigitated microelectrodes. *Sensors and Actuators B: Chemical* **2020**, 325, 128774.

4. Seymour, I.; O'Sullivan, B.; Lovera, P.; Rohan, J. F.; O'Riordan, A. Removal of dissolved oxygen interference in the amperometric detection of monochloramine using a pH control method. In 2019 IEEE SENSORS, 2019; IEEE: 2019; pp 1-4.

5. Burke, L.; Nugent, P., The electrochemistry of gold: I the redox behaviour of the metal in aqueous media. *Gold Bulletin* **1997**, 30, 43-53.

6. Nagle, L. C.; Rohan, J. F., Investigation of DMAB oxidation at a gold microelectrode in base. *Electrochemical and Solid-State Letters* **2005**, 8, C77.

7. Patella, B.; O'sullivan, B.; Daly, R.; Lovera, P.; Inguanta, R.; O'Riordan, A., Simultaneous detection of copper, lead and mercury in river water with in-situ pH control using electrochemical stripping techniques. **2020**.

8. Xu, X.; Duan, G.; Li, Y.; Liu, G.; Wang, J.; Zhang, H.; Dai, Z.; Cai, W., Fabrication of Gold Nanoparticles by Laser Ablation in Liquid and Their Application for Simultaneous Electrochemical Detection of Cd2+, Pb2+, Cu2+, Hg2+. *ACS Applied Materials & Interfaces* **2014**, 6, 65-71.

9. Cheng, Y.-m.; Fa, H.-b.; Yin, W.; Hou, C.-j.; Huo, D.-q.; Liu, F.-m.; Zhang, Y.; Chen, C., A sensitive electrochemical sensor for lead based on gold nanoparticles/nitrogen-doped graphene composites functionalized with l-cysteine-modified electrode. *Journal of Solid State Electrochemistry* **2016**, 20, 327-335.

10. Cheng, Y.; Sun, F.; Lee, J.; Shi, T.; Wang, T.; Li, Y. Gold-nanoparticles-graphene modified glassy carbon electrode for trace detection of lead ions. In E3S Web of Conferences, 2019; EDP Sciences: 2019; Vol. 78; p 03007.

11. Xiong, W.; Zhou, L.; Liu, S., Development of gold-doped carbon foams as a sensitive electrochemical sensor for simultaneous determination of Pb (II) and Cu (II). *Chemical Engineering Journal* **2016**, 284, 650-656.

12. Li, Y.; Liu, J.; Yu, F.; Tang, H.; Zhao, F.; Ye, B.-C.; Chen, W.; Lv, X., Electrochemical determination of trace lead(II) with enhanced sensitivity and selectivity by three-dimensional nanoporous gold leaf and self-assembled homocysteine monolayer. *Journal of Electroanalytical Chemistry* **2015**, 758, 78-84.

Chapter 5 Summary and Future Work

5.1 Summary

The aim of the PhD work was to develop a low-powered, micro-electrochemical sensor that can be easily mass-produced for distribution as handheld devices or long-term deployable devices for water quality monitoring. As highlighted in chapter 1, microelectrodes have many advantages over larger electrodes particularly when used as interdigitated electrodes arrays (IDE). IDEs can greatly amplify the current output of the devices through redox cycling when used as generator-collector (GC) electrodes, thus improving the limit of detection of the device. The target analyte chosen to demonstrate the effectiveness of this sensing platform was lead. A review of lead sensors in the literature also carried out in chapter 1 highlighted the need for lead sensors with a simple fabrication and, if necessary, modification process that allows for the detection in real water samples. As a result, we proposed using NPG-modified IDEs. In this instance, rather than performing as GC electrodes, the IDEs would be used for electrochemical pH control for optimum detection of lead in water.

Design, fabrication, and characterisation of the IDEs was described in chapter 2. Therein, simulations were used to identify the optimum electrode geometry for fabrication of IDEs. The use of IDEs in GC mode reduced the inter-electrode gap from >60 µm to 1 – 5 µm, reducing the overall sensor footprint by 1000x. This translates to a reduction in the cost of the materials needed to produce the devices. Several electrode geometries were investigated in this chapter showing a range of current amplification of 4.9 – 4.6x for GC mode over non-GC mode. A novel design feature explored here also was the introduction of a capping layer on the top surface of the electrodes. The capping layer was achieved by a simple additional step in the fabrication process, whereby a thin hafnium oxide (HfO_2) was applied conformally on top of the gold electrodes. The capping layer limited the reacting surface to the sidewalls of the electrodes and greatly reduced the amount of

reactant being lost of the bulk solution from the top surface of the electrodes during redox cycling in GC mode analysis. The introduction of the capping layer saw a current amplification of 3.7x over uncapped electrodes.

Chapter 3 explored the optimisation of the electrodes for detection of lead. Gold micro-disc arrays (MDAs) were initially used for analysis in this chapter. Planar gold MDAs were used to establish concentrations below 100 ppb were solely attributed to under-potential deposition (UPD). Modification of the MDAs with NPG saw a 9x increase in surface area and a 1.5x increase in current amplification for the detection of lead over planar gold MDAs. NPG modification proved to be easily transferrable to IDEs. Using a 10 ppb lead in buffered solution, 0.1 M acetate buffer pH 4.6, the optimum conditions for the detection of lead were found to be deposition at -0.75 V for 300 s followed by anodic stripping using SWV. Subsequently, analysis was carried out in the range of 0 to 100 ppb in 0.1 M acetate buffer pH 4.6. A linear range was established from 0 to 10 ppb (R^2 = 0.9951) and the limit of detection was found to be 0.43 ppb. A decline in performance was observed when the process was transferred to tap water where the lowest discernible lead stripping peak was observed at 50 ppb.

Chapter 4, the final chapter of this thesis focused on the use of electrochemical pH control for the detection of lead in tap water. The sensitivity of the gold oxide peak to pH was exploited to establish 1.55 V as the optimum potential to impose at the protonator to induce a local pH environment at the electrode surface of pH 4. Unfortunately, NPG-modified electrodes could not be utilised for application with electrochemical pH control. As a result, unmodified planar gold IDEs were used in this chapter. These IDEs were used to detect lead in the concentration range of 0 to 100 ppb in tap water using the deposition conditions established in chapter 3. The protonator electrode was held at 1.55 V during deposition and stripping. The lowest concentration of lead detectable was 10 ppb, this

result is 10 times lower than previously reported in the literature. However, *in situ* pH control did show a reduction in performance when compared to results of NPG modified IDE arrays in tap water that was chemically modified to pH 4.6, where the lowest lead concentration detected was 5 ppb. It is believed that the reduction in performance is due to an increase in the oxygen availability during the water splitting reaction used to electrochemically control the pH in the unmodified tap water samples which can then be simultaneously reduced during the lead accumulation step.

In conclusion this thesis has shown the benefits of using design, simulation, and fabrication of IDEs as a sensing platform for water quality monitoring. IDEs greatly reduce the sensor footprint leading to reductions in the cost of materials to produce such devices. The lower detection limits achievable by the current amplification of these devices make them ideal for targeting low levels of contaminants in water. *In-situ* pH control allowed for reagent-free analysis, improving the lowest detectable peak in tap water from 50 to 10 ppb which is the maximum allowable level in drinking water. Overall, the devices designed here are ideal for use in portable point of care analysis.

5.2 Future Work

The IDEs developed in this thesis proved successful for the detection of lead in tap water however, further work needs to be carried out for optimum detection. To determine the viability as a commercial sensor, a complete interferent study, lifetime testing, and susceptibility to biofouling need to be carried out. The IDEs were designed with an on-chip platinum pseudo reference, the impact of this reference electrode on the detection of lead and its stability also needs investigating. Further tests also need to be carried out to determine the optimum protonator potential and thus pH environment for the detection of

lead in tap water. Additionally, the inability to perform electrochemical pH control at devices modified with NPG needs extensive investigation.

The overall aim of developing these IDE devices was for a sensing platform for contaminants in water. Work is currently being undertaken outside of the PhD project to apply these IDEs to the detection of nitrates in tap water. Here, the IDEs can be used in GC mode where the redox reaction of nitrate reducing to nitrite can be exploited to enhance the detection of nitrate in water. Other contaminants proposed to investigate include arsenic which has a similar detection mechanism to lead and would also benefit from the ability of the IDEs to perform *in-situ* pH control.

Appendices

A.1 Publications

1. L.C. Nagle, A. Wahl, V.I. Ogurtsov, I. Seymour, **F. Barry**, J. F. Rohan, R. Mac Loughlin, Electrochemical Discrimination of Salbutamol from its Excipients in Ventolin™ at Nanoporous Gold Microdisc Arrays, Sensors, 2021, 21(12), 3975. https://www.mdpi.com/1424-8220/21/12/3975
2. K. Twomey, L.C. Nagle, A. Said, **F. Barry**, V.I. Ogurtsov, Characterisation of Nanoporous Gold for Use in a Dissolved Sensing Application, BioNanoSci, 2015, 5:55-63 https://link.springer.com/content/pdf/10.1007/s12668-014-0161-6.pdf

A.2 Invention Disclosure Forms

1. IDF 21-031: Interdigitated gold electrode array of micron-scale for lead detection in water. **F. Barry**, L. Nagle, J. Rohan.
2. IDF 21-032: Interdigitated gold arrays of micron-scale dimension modified with nanoporous silver for detection of nitrate in water using generator collector electrochemistry. L. Nagle, **F. Barry**, J. Rohan.

A.3 Presentations

1. **F. Barry**, L.C. Nagle, J.F. Rohan, Microelectrochemical Sensors for Water Quality Monitoring, 4th International Society of Electrochemistry & Royal Society of Chemistry Electrochemistry Group Irish Regional Early Career Meeting, 27th May 2021.
2. **F. Barry,** J. Rohan, Electrochemical Sensors for Detection of Volatile Organic Compounds, VistaMilk Internal Conference, 9th to 10th March 2021.
3. **F. Barry,** J. Rohan, Electrochemical Volatile Organic Compound Sensors, VistaMilk Executive Board Meeting, 2nd February 2021.
4. **F. Barry,** J. Rohan, Electrochemical Volatile Organic Compound (VOC) Sensors, VistaMilk Tyndall Catch-Up, 18th June 2020.
5. **F. Barry,** J. Rohan, Electrochemical VOC Sensors, VistaMilk Thematic Area Catch-Up, 11th June 2020.

6. **F. Barry**, L.C. Nagle, J.F. Rohan, Optimising Sensor Design for Electrochemical Analysis, 3rd International Society of Electrochemistry Regional Student Meeting Ireland, Trinity College, Dublin, 14th November 2019.
7. J.F. Rohan, L.C. Nagle, **F. Barry**, I. Seymour, Nanoporous Gold at Microdisc Arrays for Electrochemical Sensing Applications, IEEE Nano 2018, Cork, July 24th to 26th 2018.
8. J.F. Rohan, L.C. Nagle, **F. Barry**, Electrodeposition to Form Nanoporous Gold at Microdisc Arrays for Electrochemical Sensing Applications, 233rd Electrochemical Society Meeting, Seattle, WA, May 13th to 17th 2018.
9. **F. Barry**, L.C. Nagle, J. Rohan, Optimising Sensor Design for Electrochemical Analysis, Tyndall Internal Conference, 10th April 2018.
10. J. F Rohan, L.C. Nagle, **F. Barry**, Chip-scale Electrochemical Sensor for Lead & Nitrate Detection in Water, Invited Talk at Analog Devices Emerging Sensors Workshop, Limerick, November 14th 2017.
11. **F. Barry**, L.C. Nagle, B. Alameer, J. Rohan, Nanoporous Gold Modified Microdisc Arrays for Electrochemical Sensing Applications, Tyndall Student Poster Competition, 14th December 2017